Title

Geometric and molecular regulation of stress fiber viscoelasticity

Author

Kassianidou, Elena

Publication Date

2017

Geometric and molecular regulation of stress fiber viscoelasticity

By

Elena Kassianidou

A dissertation submitted in partial satisfaction of the
requirements for the degree of
Joint Doctor of Philosophy
with University of California, San Francisco
in
Bioengineering
in the Graduate Division
of the University of California, Berkeley

Committee in charge:
Professor Sanjay Kumar, Chair
Professor Tamara Alliston
Professor David G. Drubin
Professor Mohammad Mofrad

Spring 2017

Abstract

Geometric and molecular regulation of stress fiber viscoelasticity

by

Elena Kassianidou

Joint Doctor of Philosophy in Bioengineering
With University of California, San Francisco

University of California, Berkeley

Professor Sanjay Kumar, Chair

One of the most exciting recent developments in cell biology is the recognition that the geometry, topography, and elasticity of the extracellular matrix (ECM) can provide signals to cells that can affect cell physiology via a process called tensional homeostasis – the ability of a cell to balance tractional forces against the ECM. Actomyosin stress fibers (SFs) directly connect the cell to its ECM via focal adhesions and are responsible for force generation and transmission. Despite the importance of these structures, we lack a clear understanding of how the geometry of SFs, particularly their length, regulates force generation. Furthermore, current techniques used to study SF mechanical properties consider SFs as isolated bodies that lack connections with the remaining cytoskeletal elements. As a result, we lack the understanding of how tension is distributed across an individual SF that is part of a two-dimensional (2D) network.

In this dissertation, we sought to understand SF viscoelasticity by considering an SF as part of a network by combining SLA and single cell micropatterning. First, we show that longer SFs dissipate increased elastic energy after SLA. Second, we show that in addition to single SF geometry, the architecture of the connecting SF network also regulates the elastic energy dissipated by a single SF after SLA. We developed a computational model that takes in consideration the geometry of the surrounding SFs and can recapitulate SLA retraction kinetics. We then sought to understand the parameters that contribute to the observed differences in internal SF architectures and show that the initial cell binding position and spreading history on the micropattern may predict the final SF configuration. Finally, we expanded the theme of connectivity to study connections between cytoskeletal elements such as SFs and intermediate filaments. We show that vimentin interacts with central SFs and regulates SLA retraction kinetics. The work presented in this thesis provides a new framework of thinking about SFs as part of a 2D network both during cell spreading and during "steady state".

Moreover, myosin in SFs can be phosphorylated via two parallel pathways: Rho Associated Kinase (ROCK) and Myosin Light Chain Kinase (MLCK). While each pathway regulates the formation of SFs in different cellular compartments, it is unclear how each kinase contributes to the viscoelastic properties of SFs found throughout the cell. The relationship between these pathways and SF formation have been explored through pharmacological inhibition making it hard to determine whether SF properties can be tuned according to the amount of myosin phosphorylation. To study these questions, we combine SLA with synthetic biology tools and show that gradient expression of each kinase results to gradient changes in viscoelastic properties of SFs within specific cellular compartments. Specifically, MLCK induces mono-phosphorylation of myosin which primarily localizes in peripheral SFs, altering their viscoelasticity whereas ROCK induces myosin di-phosphorylation which primarily localizes and controls the viscoelastic properties of central SFs.

Overall, this thesis represents a systematic attempt to combine single cell micropatterning and SLA tools to relate single SF geometry and architecture of the connecting SF network to single SF mechanics. Our findings enhance our understanding of how cells distribute tension across a network of SFs and other cytoskeletal structures, addressing a fundamental open question in cell biology. We also provide further insight into the mechanistic pathways of SF tension generation by ascribing the viscoelasticity of SFs found in different cellular compartments to the activity of specific kinases.

Table of Contents

Acknowledgments

There are so many people to thank for all the help (both technical and emotional) throughout this long journey. I know that my dissertation would not have been possible without them.

First, I would like to thank my graduate advisor, Professor Sanjay Kumar, for his guidance and help throughout my PhD. Sanjay's calmness and optimism are a perfect fit to my somewhat dramatic attitude. He remained positive and confident in me through experimental failures and through the third-year slump. His mentoring has taught me so much – from improving my own presentation/writing and mentoring skills to the way I approach research questions and I cannot emphasize enough how instrumental he has been in my development as a researcher.

I would also like to thank the members of my qualifying exam and dissertation committee, including Professor Tamara Alliston, Professor Dan Fletcher, Professor Matt Welch, Professor David Drubin and Professor Mohammad Mofrad. I appreciate all the insightful advice on my projects, my overall graduate school experience and life after graduate school. Special shout out to Professor Tamara Alliston who in addition to being part of my quals and thesis, she was also one of my rotation mentors and has always had my back, providing endless words of wisdom and encouragement.

I owe so much to my labmates (current and past) that I honestly do not think I would be where I am today without them. Spending time with you in and out of lab was so enjoyable and fun! I always felt so supported and you all made the bad days brighter and the good days even better. I thank all the past lab members for dealing with me as a rotation student and a second/third year graduate student, specifically Joanna MacKay, Badri Ananthanarayanan, Andy Rape, Sophie Wong, Ching-Wei Chang and Yushan Kim. You all guided me through formulating my project, got me through my qualifying exam and helped me troubleshoot (and stay sane!). I also want to thank my current lab members, Mike Kang, George Lin, Stacey Lee, Jasmine Hughes, Kelsey Springer, Phil Kang, Kayla Wolf, Ruoxing Lei and Joe Chen for amazing science discussions/troubleshooting/help, laughs, lunches, coffee breaks, happy hours and so much more. You all set the bar high for my future labmates!

Some of the projects I worked on were collaborations and I was fortunate enough to have collaborators that really cared about the projects, were critical in their feedback and worked hard to get the projects going. I would like to thank Professor Ulrich Schwarz (University of Heidelberg), Christoph Brand (University of Heidelberg), Amy Shyer (UC Berkeley) and Anne-Lou Roguet (Ecole Polytechnique) for all your hard work and time.

I should emphasize that had I not done research in my undergraduate studies, I would not be where I am today. I would like to thank Professor Jan Skotheim for taking a chance with me during sophomore year and for being my first research mentor. Jan paid attention to my interests and was the one that encouraged me to write an honors thesis and follow my heart. I would also like to thank Amanda Amodeo who was the graduate student I worked with. Amanda gave me a lot of freedom to explore the project we were working on and the confidence to try out experiments, fail and move on – a valuable skill for a career in research.

I am so lucky to have wonderful friends (from Cyprus, Stanford and now Berkeley) and their support has been invaluable throughout this whole process. I strongly believe that my experience was as good as it was because of the supporting system I had; filled with girls' nights (thank you Jen, Shea, Annie and Martha), amazing roommates (Jen, Martha, Preeya and Elaine), delicious monthly dinners with Marta and Rachel and super relaxing and fun times back in Cyprus/England with Andrea, Katia and Chrissy. I cannot give enough credit to Todd – he has been a trooper throughout this whole journey. He always listened, helped, and supported me in so many ways – he should probably be getting an honorary PhD!! Thank you so much Todd for all the adventures we have had and for all the support you are constantly giving me. I look forward to our future adventures wherever we may be!

Finally, I'd like to thank my family, especially my parents and grandparents for allowing me to pursue my dreams even if it meant being away from home for so long, encouraging me during difficult times and celebrating with me from afar (and spoiling me every time I came home with lots of food and hugs!). Mum, thanks for reading everything I wrote even if it did not make much sense to you. Dad, thanks for all the delicious food you put in our freezer – made our lives much easier. Marina, thanks for inspiring me to keep studying and all the tips you gave me during my grad school. Christo, thanks for keeping it real!

P.S. Kumar lab would like to thank my parents and grandparents for kourabiedes and cookies

Chapter 1: A biomechanical perspective on stress fiber structure and function

1.1 Abstract

Stress fibers are actomyosin-based bundles whose structural and contractile properties underlie numerous cellular processes including adhesion, motility and mechanosensing. Recent advances in high-resolution live-cell imaging and single-cell force measurement have dramatically sharpened our understanding of the assembly, connectivity, and evolution of various specialized stress fiber subpopulations. This in turn has motivated interest in understanding how individual stress fibers generate tension and support cellular structure and force generation. In this review, we discuss approaches for measuring the mechanical properties of single stress fibers. We begin by discussing studies conducted in cell-free settings, including strategies based on isolation of intact stress fibers and reconstitution of stress fiber-like structures from purified components. We then discuss measurements obtained in living cells based both on inference of stress fiber properties from whole-cell mechanical measurements (e.g. atomic force microscopy) and on direct interrogation of single stress fibers (e.g. subcellular laser nanosurgery). We conclude by reviewing various mathematical models of stress fiber function that have been developed based on these experimental measurements. An important future challenge in this area will be the integration of these sophisticated biophysical measurements with the field's increasingly detailed molecular understanding of stress fiber assembly, dynamics, and signal transduction.

1.2 Introduction

The ability of a eukaryotic cell to adhere, spread, migrate and resist deformation depends on the ability of the cell to generate force against the surrounding extracellular matrix (ECM). These forces are not only essential for structural regulation in individual cells but can also control morphological changes in tissue during development (1). Changes in the magnitude and direction of these forces at either the cell or tissue length scale can contribute to the development of diseases such as atherosclerosis, osteoporosis and cancer. The cytoskeleton, an interconnected network of filamentous proteins consisting of actin filaments (F-actin), microtubules, intermediate filaments, and their associated molecular motors and other accessory proteins, acts as a physical and biochemical link between the cell and the ECM (2). The cytoskeleton senses, generates and mediates coordinated forces to maintain tensional homeostasis and control normal cell and tissue function (3, 4). It has been shown to contribute to cellular contractility and matrix reorganization in both highly simplified two-dimensional culture paradigms as well as more complex, three-dimensional microenvironments (5), reflecting the need to study how cytoskeletal components generate, transmit and withstand forces over time as a means of understanding how cells behave in vivo.

Stress fibers represent an important component of the cytoskeleton. Stress fibers are bundles of actin filaments with alternating polarity held together by various crosslinking proteins such as α-actinin and zyxin. Often, but not always, stress fibers also contain non-muscle myosin II (NMMII) bipolar filaments. Although stress fibers can resemble myofibrils in their composition, they exhibit a less organized structure; if sarcomeres are present, they are not as regular as myofibrils and actin filaments are not uniformly located along the fiber length (6). Contraction of NMMII produces a force along the length of the fiber that is transmitted through cellular adhesions to the extracellular matrix (ECM) allowing the fibers to be in isometric tension. Stress fibers are physiologically important in processes that require cellular contraction such as wound healing and exocrine gland secretion (7). For example, during wound healing, tension borne by specific stress fibers within fibroblasts can induce recruitment of α-smooth muscle actin to these fibers, which in turn permits even greater generation of tensile force (8, 9). This tension generation can activate latent Transforming Growth Factor β1 (TGF β1) within the matrix, promoting these fibroblasts to differentiate into myofibroblasts that drive tissue compaction (10). This increased stress fiber-driven contractility therefore initiates a positive feedback loop of increased tension generation and myofibroblast differentiation that contributes to eventual wound closure (11, 12). Epithelial cells that line the wound site also develop actomyosin cables that contract to facilitate wound closure (13). These principles are not limited to wound healing; epithelial cells around exocrine glands also form stress fibers whose contraction promotes secretion. In the presence of oxytocin, myosin is activated, leading to increased contraction around the mammary gland and eventual secretion of milk (14, 15).

The growing appreciation of the physiological importance of stress fibers has spurred significant interest in quantifying the mechanical properties of stress fibers and the roles they may play in supporting cellular structure, motility and tissue processes. Thus, a rich variety of tools have recently emerged to study the mechanical and structural properties of stress fibers and determine new physical models of how stress fibers contract and contribute to the overall mechanics of the cell. In this review, we will discuss both in vitro (cell-free) and in vivo (live-cell) tools available to study the mechanical properties of stress fibers and how these tools have been used to advance our understanding of stress fiber biomechanics. Several excellent reviews have covered broad aspects of stress fiber structure and function (2, 16, 17). Here, we will concentrate on current biomechanical models of stress fiber structure and function and end with a discussion of unanswered questions in the field.

1.3 Stress fiber composition

Stress fibers are generally defined as bundles of 10 – 30 thin filaments, composed of F-actin crosslinked by actin-binding proteins such as α-actinin, fascin and filamin. These thin filament bundles are frequently but not always interleaved with thick filaments composed primarily of non-muscle myosin II (NMMII) motors, the key force generating component in stress fibers (Figure 1A). NMMII is a hexamer that consists of two essential light chains (ELCs), two regulatory light chains (RLCs) and two heavy chains. The heavy chains contain the head domain, which is a globular structure that can both directly engage F-actin and hydrolyze ATP to provide the free energy required to power the contractile sliding of the thick filaments against the thin filaments, thus creating tension within the stress fiber (Figure 1B and C). Phosphorylation of the RLC facilitates this process by allowing myosin to uncoil and assemble into linear thick filaments, as well as enhancing its ATPase activity (18).

There are three NMMII isoforms in mammalian cells: NMMIIIIA, IIB and IIC, with the isoform specified by the heavy chain. NMMIA and IIB are the predominant isoforms, and much effort has been devoted to understand their differential biophysical properties and contributions to cell mechanics and motility. Much less is known about the in vivo function of NMMIIC, although it appears to play central roles in specific physiological contexts. For instance, NMMIIC is critical for the outgrowth of neuronal processes, can modulate neuronal cell adhesion (19) and is important in the cytokinesis and motility of cancer cells (20).

Within polarized cells, there is an overall differential distribution of NMMIIA and IIB with an observable NMMIIA-rich state in the front and a NMMIIB-rich state in the rear (21). The differential localization of NMMII isoforms is thought to correspond to distinct mechanical functions: NMMIIB found at the cell rear promotes directional migration by preventing protrusion formation and properly positioning the Golgi apparatus, the nucleus and microtubules, whereas NMMIIA found at the cell front contributes to nascent adhesion formation (18, 22, 23). The application of new super resolution imaging methodologies has introduced important complexities to this picture; two-color total internal reflection fluorescence/structured-illumination microscopy imaging of NMMIIA, IIB and IIC revealed that IIA and IIB as well as IIA and IIC co-assemble to form heterotypic filaments within single stress fibers, implying that the differences in regional localization may reflect a continuum of isoform-rich states (21). In addition to their differential localization, myosin isoforms also exhibit varying motor functions. NMMIIA has a higher rate of ATP hydrolysis and can slide actin filaments more rapidly than IIB. NMMIIB has a higher duty ratio and can stay bound to actin longer, which has led to the notion that IIB may drive sustained contraction (24). Given the different force-generating properties of myosin isoforms, one might predict that stress fibers made up of different compositions of myosin isoforms would exhibit different mechanical properties and may have different biological functions within a cell.

Stress fiber contractility depends on the polarity of the actin filaments. Since NMMII motors move towards the barbed ends of actin filaments, successive actin filaments must have opposite polarity to allow for NMMII sliding and subsequent contraction. Actin filaments in stress fibers can exhibit different patterns of polarity – some stress fibers exhibit the expected opposite polarity, others seem to be randomly oriented, whereas stress fibers of motile cells have regions of both uniformity and randomness (25). An important open question is how actomyosin networks with randomly oriented polarities that form at the leading edge evolve into more mature stress fibers with sarcomeric orientations. Recent actomyosin reconstitution studies have offered an elegant solution to this problem. In an actomyosin complex with mixed orientations, the sarcomeric regions generate tension whereas the non-sarcomeric regions generate compression. These internal tensile and compressive forces cause the regions with non-sarcomeric orientations to buckle and sever, effectively selecting these regions out and enriching the sarcomeric fraction (26). The contractile ring formed during cytokinesis represents an example of a structure that is not formally classified as a stress fiber but has been successfully computationally modeled by applying analogous concepts (27). It is likely that similar approaches may be fruitful in dissecting the function of other actin bundles, such as those found in filopodia (2, 28) or retraction fibers during cell division (29).

1.4 Stress fiber connectivity to the extracellular matrix and force transmission

Stress fibers can directly couple to the cell-ECM interface through focal adhesions, which contain a variety of actin binding proteins such as zyxin and paxillin, or indirectly by inserting themselves into (i.e. branching from) other stress fibers. When the tension within stress fibers is balanced by the mechanical resistance of the structure(s) to which they are attached, stress fibers are under isometric tension. Changes in isometric tension play a central role in sensing and adapting to extracellular forces, and thus stress fibers may be regarded as mesoscale mechanosensors (30). For example, endothelial and vascular smooth muscle cells commonly respond to cyclic stretch by reorganizing their stress fiber networks perpendicular to the axis of stretch (31). The strains induced by cyclic stretch can promote localization of specific proteins to stress fibers to facilitate remodeling (32) and stress fiber rupture can initiate a zyxin-mediated repair process (33). Indeed, even strains that are not sufficient to induce rupture may be sensed by sarcomeres within stress fibers; when a specific region of a stress fiber is extensionally adapting to extracellular forces, and thus stress fibers may be regarded as mesoscale

mechanosensors (30). For example, endothelial and vascular smooth muscle cells commonly respond to cyclic stretch by reorganizing their stress fiber networks perpendicular to the axis of

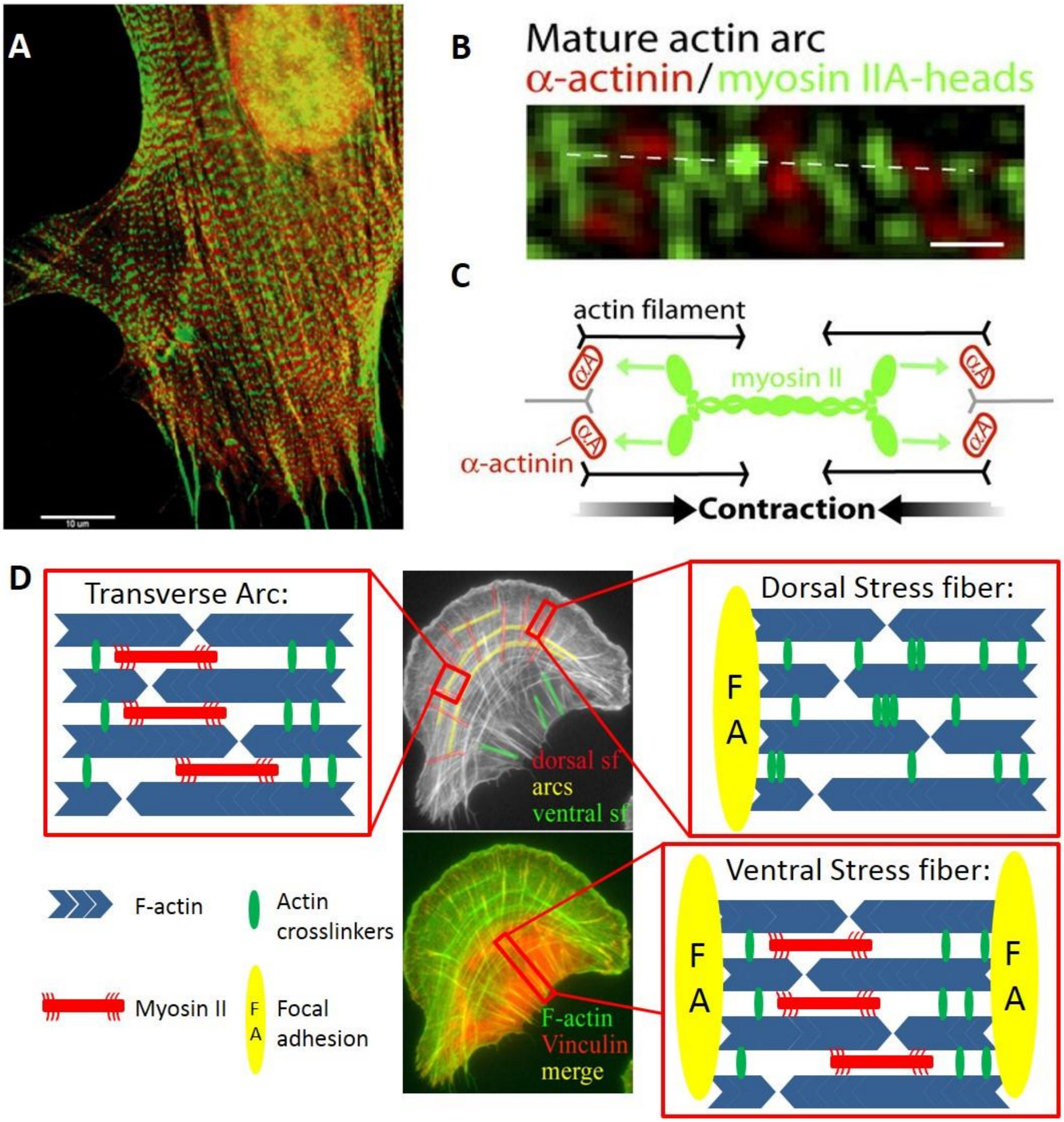

Figure 1: Stress fiber structure and composition. (A) A gerbil fibroma cell in stained for myosin light chain (red) and α-actinin (green) to illustrate the periodic localization of proteins along the stress fiber(34). (B) Structured illumination microscopy of the nanoscale organization of myosin IIA minifilaments in actin fibers using U2OS cells expressing α-actinin mApple (green) and myosin IIA-mEGFP (35). (C) Schematic showing how the interaction of myosin minifilaments can lead to sarcomere contraction of stress fibers (35). (D) Schematic of the three stress fiber subtypes indicated in a U2OS human osteosarcoma cell stained for F-actin (green) and the focal adhesion marker vinculin (red). Boxed regions highlight the structural differences between the three stress fiber subtypes.

stretch (31). The strains induced by cyclic stretch can promote localization of specific proteins to stress fibers to facilitate remodeling (32) and stress fiber rupture can initiate a zyxin-mediated repair process (33). Indeed, even strains that are not sufficient to induce rupture may be sensed by sarcomeres within stress fibers; when a specific region of a stress fiber is extensionally strained beyond a threshold, surrounding sarcomeres compensate by contracting to preserve stress fiber length, after which zyxin and α-actinin are recruited to the sites of high strain to form new sarcomeres (36, 37) . These findings suggest the presence of a tensional homeostasis mechanism that is based on sarcomere communication and provide evidence for the mechanosensitivity of stress fibers.

The formation and contractility of stress fibers are also associated with stem cell differentiation, in that cells grown on micropatterned islands of fibronectin that promoted increased stress fiber and focal adhesion formation also exhibited increased osteoblastic differentiation(38). More recently, Zemel and colleagues computationally investigated the effect of stress fiber alignment and cellular shape in stem cell differentiation (39). This study revealed that maximal stress fiber polarization occurs at an optimal ECM rigidity analogous to the optimal stiffness for stem cell differentiation, suggesting that fiber orientation may play an important intermediary role in converting matrix stiffness cues into differentiation programs. These studies strongly hint at the importance of stress fiber mechanosensing to cellular phenotype and illustrate the power of microfabrication techniques for manipulating stress fiber alignment and stem cell differentiation.

1.5 Classification of stress fibers

A widely-used classification scheme describes three different stress fiber subtypes – transverse arcs, dorsal stress fibers, and ventral stress fibers – based on their molecular composition, connectivity to focal adhesions, assembly mechanisms and dynamics, and biological function (40) (see Figure 1D). As the name would suggest, transverse arcs are curved stress fibers found parallel to the leading edge and are assembled from shorter actin filaments that originate in the lamellipodium (40). Transverse arcs are contractile and do not attach to focal adhesions at all. Dorsal stress fibers assemble in a myosin-independent fashion from nascent F-actin bundles within the lamellar compartment of the leading edge of the cell and are generally regarded as non-contractile (41). Dorsal stress fibers extend vertically upwards from their origin in a focal adhesion, insert into transverse arcs, and thereby mechanically link transverse arcs and focal adhesions at the front of the cell. Recent evidence makes a compelling case that this organization allows transverse arcs to distribute tension to the cell-ECM interface via their connectivity to transverse arcs and flatten the lamellar region by “levering down” dorsal stress fibers using focal adhesions as a fulcrum (35). Dorsal fibers may also act as a structural template to facilitate maturation of integrin-based focal adhesions found at the leading edge (42, 43). While the molecular mechanism of assembly of these structures remains incompletely understood, palladin was recently found to be specifically required for the assembly of dorsal stress fibers and essential for the generation of a fully functional stress fiber network in both two dimensional and three dimensional matrices (44). Ventral stress fibers, the third category, are NMMII-rich and generate strong traction forces at the cell base. These traction forces are particularly important for detaching the trailing edge of the cell during directional migration, and by extension for the establishment of front-to-rear polarity (45). Ventral stress fibers are thought to assemble through the fusion of transverse arcs and dorsal stress fibers or by fusion of two dorsal stress fibers; consequently, they are attached to focal adhesions at both ends and are optimally positioned to tense the ECM(40). The radial architecture and contractile activity of specific fiber subpopulations has been implicated in driving cell-scale symmetry-breaking and establishment of chirality (46).

1.6 *In vitro* micromanipulation

Studying single actin filaments and extracted stress fibers:

There have been several notable efforts to measure mechanical properties of stress fibers in cell-free preparations. Initial efforts focused on the use of glass needles, microcantilevers, and microneedles to probe reconstituted single actin filaments, with the notion of scaling up these measurements to estimate properties of bundles (47, 48, 49). While these measurements have been highly instructive, stress fibers are bundles of individual actin filaments reinforced by a variety of binding partners and motor proteins, which makes it inherently challenging to infer the mechanical properties of a bundle of crosslinked actin filaments from those of a single actin filament.

Thus, more recently, strategies have been developed to extract and mechanically manipulate intact stress fibers from living cells. For example, Katoh and colleagues used low ionic strength solution and detergent extractions to “de-roof” fibroblasts adherent to two-dimensional substrates, leaving behind matrix adhesions and their associated stress fibers (50) (see Figure 2). Notably, these isolated stress fibers retained their contractility, with the magnitude of contractility dependent on the concentration of ATP, and produced length contractions of up to 20% (50). The mechanical properties of isolated stress fibers were further investigated by performing tensile tests with the use of microcantilevers (51). The longitudinal elastic modulus of an isolated stress fiber increased nonlinearly with strain (approximately 1.45MPa for smooth muscle cells and 300kPa for endothelial cells assuming uniform structure and $0.05\mu m^2$ cross sectional area). Additionally, the force required to stretch a single stress fiber from its zero stress length to its original length was approximately 10nN, which is comparable with local traction forces of single adhesion sites (52). This suggests that stress fibers can bear substantial stresses and could account for traction observed at the cell-matrix interface.

Reconstitution of actomyosin cables:

Another powerful approach used to study the mechanical organization and function of stress fibers is *in vitro* reconstitution of minimal actomyosin structures. In principle, this approach combines the control associated with the use of purified materials while capturing some of the complexity that might be found in intact stress fibers. Actomyosin reconstitution involves polymerization of F-actin in the presence of myosin thick filaments and subsequent measurement of contraction and force generation. For over 60 years, this approach has been used to identify the minimal components necessary for reconstructing contractility and their dependence to contractility (53–55). Studies have concentrated on the effect of actin crosslinkers such as fascin, filamin A and α-actinin on the mechanical properties of an actomyosin network (56). Until recently, mechanical studies on reconstituted actomyosin networks were performed in a three dimensional gelatinous state and not the highly organized and anisotropic state characteristic of the cellular actomyosin network. In particular, a major challenge in the field had been the assembly of actomyosin complexes into two-dimensional bundles that could begin to mimic stress fibers.

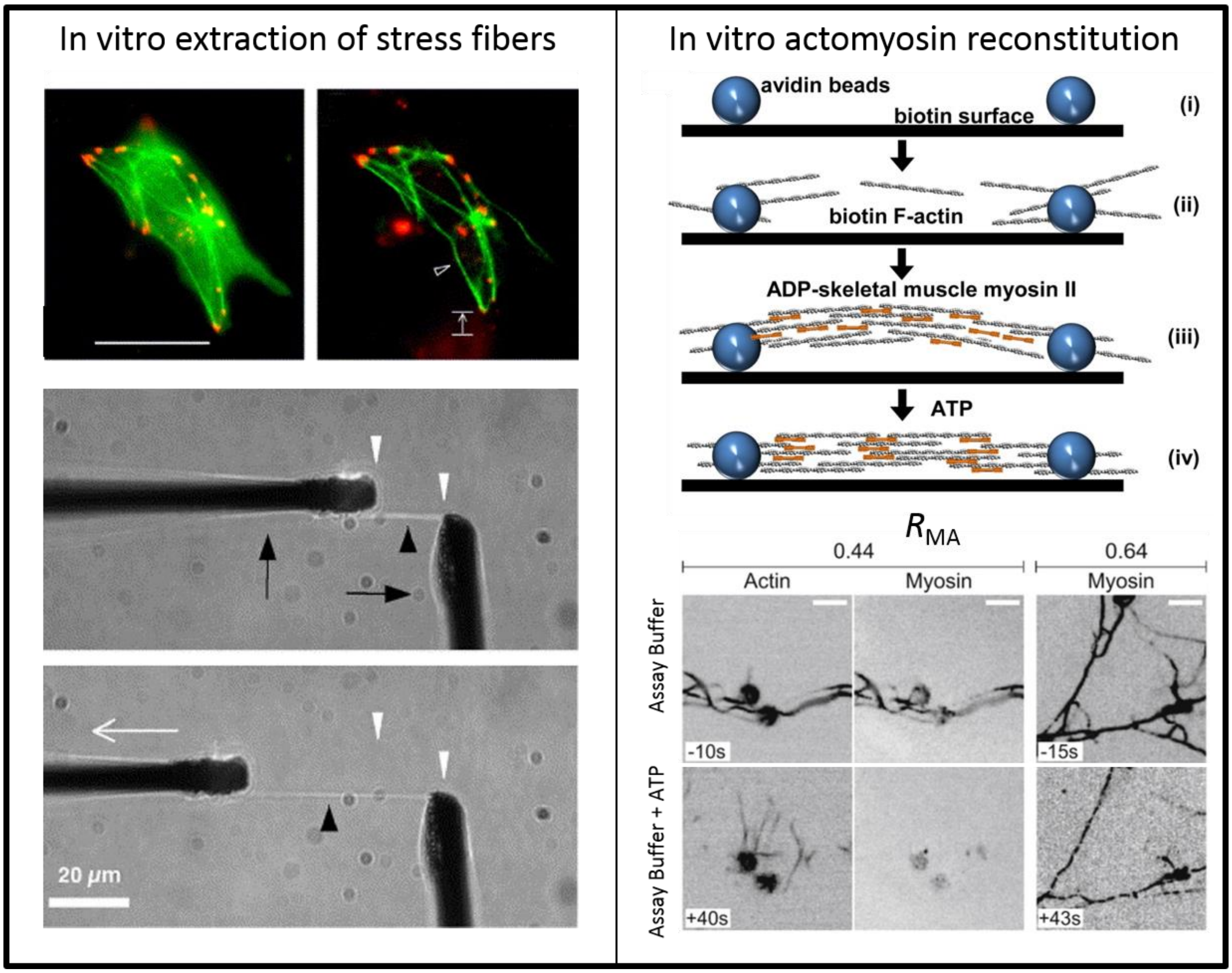

Figure 2: In vitro tools used to study stress fiber mechanical properties. Left: In vitro extraction of stress fibers. SMCs expressing GFP-actin before and after stress fiber extraction treatment and detachment from the substrate to obtain isolated stress fibers that can then be used in mechanical tests such as tensile stretching (51). Right: In vitro actomyosin reconstitution. Schematic illustrating bundle assembly and contraction of in vitro reconstituted actomyosin fibers (57). Addition of ATP allows for myosin contraction which results in an isometric tension within the reconstituted fibers as illustrated in the images (58).

This need has motivated recent efforts to reconstitute actomyosin bundles *in vitro*, with the goal of measuring the mechanical properties of the assembled structures and understanding how specific molecular components contribute to mechanics and function. In one strategy, to promote assembly of actomyosin bundles, F-actin was attached on neutravidin beads bound to a coverslip. Thick filaments of smooth muscle myosin were subsequently added, allowing the myosin heads to bind to F-actin, resulting in the formation of actomyosin bundles of varying lengths (5 to 50μm) (see Figure 2) (58, 59). At a low density of myosin, smooth muscle myosin thick filaments stabilized actin filaments and formed bundles with no measurable contraction. At a higher density and with the addition of ATP, the presence of myosin filaments was sufficient to elicit contraction and generate tension, even in the absence of actin crosslinkers or sarcomere formation (58). More recently, these bundles have been used to study the effects of the isoform composition of myosin filaments (nonmuscle vs. skeletal muscle vs. smooth muscle) to contraction rates as well as the mechanism of self-organization to sarcomere-like structures and its regulation by myosin-mediated forces (60, 57).

In addition to exploring how the mechanical properties of stress fibers depend on their molecular composition, actomyosin reconstitution can also been used to dissect the molecular mechanisms through which focal adhesions associate with the actomyosin cytoskeleton (61). Reconstitution of purified actin, myosin and vinculin on talin-micropatterned surfaces led to new insight into how vinculin associates with talin within a focal adhesion and the role of the cytoskeleton in reinforcing this association. Activation of vinculin by a stretched talin protein leads to a positive feedback loop that reinforces the actin-talin-vinculin association, revealing a molecular switch mechanism that controls the connection between adhesion complexes and the actomyosin network (61). Recently, actomyosin bundles were reconstituted in lipid vesicles to investigate effects of spatial confinement on bundle assembly and contractile function (62). Remarkably, increasing the myosin concentration facilitated the assembly of an equatorial actin ring and then contracted the ring, reminiscent of constrictions formed at the cleavage furrow during cytokinesis.

Reconstitution and extraction approaches have complementary strengths and limitations. Actomyosin reconstitution provides a more simplified and controlled system to study the contractility of stress fibers than extraction of stress fibers from fixed cells. Simply by including or excluding specific molecular components and controlling their relative stoichiometry, it is possible to identify functionally important proteins and quantitatively dissect how these proteins contribute to contractility. In contrast, isolated stress fibers are a complex multi-component system made up of different proteins that can vary based on the extraction method used, making it hard to identify how each protein contributes to contractility in a quantitative manner. On the other hand, isolated stress fibers retain key components found in cellular stress fibers and offer the opportunity to study how stimulation of specific signaling systems influences contractility. For example, stress fibers subjected to glycerol extraction have been reported to contract both in the presence and absence of Ca^{2+} whereas fibers extracted using Triton X-100 (presumably a different subset of fibers) only contract in the presence of Ca^{2+} (63–65). Triton X-100 dissolves RhoA and Rho-associated coiled-coil containing protein kinase (ROCK) leading to isolated stress fibers that can only contract via the Myosin Light Chain Kinase (MLCK) pathway, providing direct evidence that stress fiber contraction is dually regulated with two different modes of contraction – a rapid, extensive contraction induced by MLCK and a slower contraction controlled by RhoA/ROCK (65).

1.7 *In vivo* macromanipulation

Whole-cell stretch experiments to explore cytoskeletal mechanics:

Complementary to the above approaches, there has been much interest and effort to understand the mechanics of stress fibers in their cellular context, without having to remove or rebuild them. Initial efforts to do this have sought to infer the properties of cytoskeletal structures from measurements of whole-cell mechanics. Whole-cell tensile and compression tests, including those involving stretched/released silicone culture substrates and micropipette-based stretching of single cells, have been used to study how stress fibers bear and dissipate externally applied loads (66, 67). Osteoblasts seeded on a stretched silicone rubber were fixed 5 min after constant strain release with an observable 20% pre-strain on each stress fiber (68). Stress fibers of human aortic endothelial cells seeded on an initially pre-stretched silicone substrate buckled in a non-uniform manner with a calculated pre-strain distribution of 15-26% when tension was released. The variability suggests the presence of heterogeneity in cytoskeletal tension and stiffness within individual stress fibers (66). The presence of buckling was surprising since it suggested that stress fibers are not only mechanically constrained at their ends via focal adhesions but may also be constrained along the length of the fiber, potentially due to smaller adhesions or other cytoskeletal constituents such as microtubules. Nocodazole-induced disintegration of the microtubule network decreased the buckling frequency, suggesting a possible coupling between stress fibers and microtubules. A later study explored the connection of microtubules with the surrounding elastic cytoskeleton and provided evidence that the coupling of the two networks mechanically reinforces microtubules, allowing them to withstand high compressive forces and buckle at short wavelengths, without necessarily requiring discrete adhesion points between the microtubule and surrounding network (69). Given the heterogeneity of sarcomere contraction observed within a single fiber (34) as well as the buckling heterogeneity observed within the whole cell, it is challenging to interpret from these studies how a single stress fiber contributes to the overall cellular tension, or whether the mechanical differences in different fiber populations arise due to differences in fiber architecture or differences in myosin activation.

Tools to correlate cellular mechanical properties to stress fiber mechanics:

Perhaps most relevant to stress fiber function, several tools have been developed over the past two decades to quantify traction force generated by cells against the ECM. Coupled with molecular manipulations, these techniques may be used to determine how specific components contribute to traction force generation. For example, in traction force microscopy (TFM), traction stresses applied at the cell-ECM interface are recovered by tracking the displacement of fiduciary markers embedded within the underlying matrix. An important limitation of most current TFM strategies is that, with few exceptions(70), they do not incorporate intracellular structure, such that it is difficult to infer how much traction forces measured at specific adhesion sites are being transmitted to stress fibers, and what the molecular mechanism of that force transmission may be (71).

Atomic Force Microscopy (AFM) is another single-cell technology that has been used to mechanically interrogate living cells and to infer mechanical properties of stress fibers and other cytoskeletal structures (Figure 3). Because AFM does not require fixation and may be performed in culture medium, it is ideally suited to probe living cells under physiological conditions. In AFM, a microscale cantilever spring may either be scanned across a surface to obtain nanometer-resolution images or used to indent materials at a fixed horizontal position to discern mechanical properties. In the latter modality, AFM indentation curves may be fit using models of indentational elasticity (e.g. Hertz) to obtain a Young's Modulus; repetition of this measurement at different locations along the sample permits construction of elasticity maps. When combined with fluorescence imaging of labelled intracellular structures, elasticity mapping can be used to determine the local elastic modulus of a variety of superficial cellular structures, including stress fibers. For example, AFM elasticity mapping and topographical imaging combined with fluorescence imaging of the cytoskeleton showed that stress fibers colocalize with regions of higher stiffness (72). These approaches may also be coupled with small-molecule inhibitors of cytoskeletal function to dissect the contribution of specific networks to cellular elasticity (73). In one study, 3T3 and NRK fibroblasts were incubated with cytochalasin or latrunculin, which potently inhibit actin polymerization. Subsequent correlation of AFM elasticity maps with fluorescence images of the actin cytoskeleton revealed that these treatments both disaggregated stress fibers and reduced cell rigidity, underscoring the important contributions of the actin cytoskeleton to cellular elastic properties. Even with the use of highly specific cytoskeletal inhibitors, however, it is impossible to dissect the mechanical contributions of individual stress fibers within a cell.

While the ability to correlate images and mechanical measurements is an important advancement, it nevertheless still represents an indirect probe of the elasticity of subcellular structures and reflects the collective contributions of other structural elements. Moreover, living cells violate key assumptions of the theories commonly used to obtain Young's moduli from AFM stiffness measurements, in that cells are neither homogeneous, nor isotropic, nor linearly elastic, nor infinitely thick.

Imaging and mechanically indenting individual stress fibers using atomic force microscopy:

More recently, AFM has been used to investigate the mechanical properties of *individual* stress fibers within the cell providing an even more direct assessment of the mechanical properties of a stress fiber using a non-Hertzian approach (74, 75). AFM was used to perform nanoindentations in an 8 x 6 array on a region of the cell surface that included a single stress fiber. Based on differences in the AFM contact mode images, stress fiber localization was determined and its presence was correlated with elasticity measurements. The authors demonstrated that for strains up to 12%, an individual stress fiber had approximately linear stress-strain properties with a calculated transverse elastic modulus of approximately 12 kPa at both peripheral and central regions within the same stress fiber (75). Addition of calyculin-A, a drug that increases myosin activation through inhibition of myosin light chain (MLC) phosphatase, led to heterogeneous changes in stiffness along the same stress fiber. This highlights the critical role of myosin force generation in determining the stress fiber mechanical stiffness as well as the dynamic and non-uniform contractile nature of stress fibers.

It should be noted that the elastic modulus of an individual stress fiber reported by AFM was much smaller than the elastic modulus of isolated stress fibers, with the difference potentially arising from the differences in the experimental systems, the intrinsic anisotropy of the stress fiber, and/or the presence of other cellular components that may physically interact with stress fibers in the cell but are absent when the stress fiber is isolated. Additionally, an important caveat with AFM measurements of stress fibers is that AFM can only examine the exterior surface of a living cell, so that deep structures cannot be indented without also indenting the overlying superficial structures, which may then contribute to measured elastic moduli.

1.8 *In vivo* micromanipulation: Subcellular laser nanosurgery

Subcellular laser nanosurgery has emerged as a tool that allows one to directly study the viscoelastic properties of individual stress fibers within the cell interior. Subcellular laser microsurgery has been used since the late 1970s to study the mechanical properties of an individual stress fiber directly. In 1979, Strahs and Berns used an attenuated Nd:YAG laser microbeam with various wavelengths to ablate a single stress fiber in non-muscle cells (76). The authors observed that after ablation, the fiber ends retracted and repaired over time. Incubation of cells with cytochalasin B prior to laser ablation led to increased retraction distances, possibly due to disruption of fiber attachment points with the membrane, and decreased repair of the fiber ends (77). The method described could create a break ranging from 0.25 – 2 μm in length without affecting cell motility, shape and matrix adhesion. Interestingly, these early studies revealed that not all stress fibers retracted upon incision, suggesting that different fibers bear different levels of tension and presumably exert different contractile forces, presaging the now well-validated notion that some stress fibers primarily play structural roles (e.g. dorsal fibers) whereas others are highly contractile (e.g. ventral fibers) (78).

The precision of laser nanosurgery has advanced with improvements in laser technology and optics. Building from the early work of Berns and coworkers, intracellular nanosurgery systems have been developed in which femtosecond laser pulses are focused by a high-numerical aperture objective and confined to a very small focal volume, thus inducing multiphoton absorption and plasma mediated ablation of biological material within <300nm (79–81). This capability has been leveraged to sever individual stress fiber bundles within the cell and follow the retraction over time (82) (Figure 3). For example, severing a stress fiber in a living endothelial cell causes the fiber to retract in parallel with the axis of the fiber; fitting the retraction kinetics with a Kelvin-Voigt model revealed that the fiber behaves as a viscoelastic cable that has an elastic component and a viscous dissipative element(83). Subcellular laser nanosurgery can be combined with TFM to determine how single stress fibers distribute load across focal adhesions and throughout the cell. Studies with TFM revealed that the tension released by a single stress fiber after ablation contributed to ECM strain across the entire cell-ECM interface, with higher strains found at focal adhesions near the ablated stress fiber (82).

In addition to its utility for probing the mechanics of stress fibers, femtosecond laser nanosurgery may also be used to investigate how tension affects the localization and function of specific mechanosensory proteins at the cell-ECM interface. For example, the focal adhesion protein zyxin had been implicated as a mechanosensor based on its ability to localize to stress fibers upon stretch or shear (84), yet the biophysical basis of this connection had remained a mystery. To address this question, Lele and co-authors combined laser nanosurgery with fluorescence recovery after photobleaching (FRAP) to study how stress fiber tension influences the binding kinetics of zyxin to associated focal adhesions. These studies revealed that dissipation of tension significantly increased the off-rate with which zyxin engaged focal adhesions, suggesting a mechanism through which cell-scale forces could influence molecular-scale localization (85, 86).

Taking this approach one step further, laser nanosurgery has been combined with molecular biosensors of tension to determine how individual stress fibers contribute to tension across specific mechanosensory proteins within focal adhesions. One study used laser nanosurgery to sever stress fibers while simultaneously applying a vinculin-based fluorescence resonance energy transfer (FRET) tension sensor (87) to show that tension released from a single stress fiber increased or decreased vinculin tension within a given focal adhesion in a manner that depended on the directional alignment of that adhesion with the incised stress fiber (88). Combining laser nanosurgery with other techniques has the potential to map cytoskeletal mechanics within the cell and show direct connections of tension transmission between individual molecules at the nanoscale, individual contractile elements in the micron scale and traction forces exerted by whole cells.

Combining laser nanosurgery with pharmacological and genetic manipulation of signaling has enabled more precise determination of how specific myosin activators contribute to tension generation. For example, inhibition of the myosin activators ROCK and MLCK significantly altered the rate and extent of stress fiber retraction, providing evidence that myosin motors contribute heavily to stress fiber elasticity (82, 89). This capability has been used to map elastic properties of stress fibers within the cell and implicate specific myosin activators in controlling tension within different cellular compartments (89). Inhibition of ROCK and MLCK abolished the retraction of central and peripheral stress fibers respectively, and this is consistent with earlier findings (64, 65). Moreover, each stress fiber population displayed different viscoelastic properties and structural contributions, with incision of peripheral stress fibers producing more viscous retraction and leading to whole-cell contraction (89).

The ability to combine subcellular laser nanosurgery with other techniques such as the ones described above makes it a very powerful tool that allows one to probe not only the mechanical and force transducing properties of stress fibers but also determine how stress fiber molecular activation and architecture contribute to their contractility and mechanical behavior.

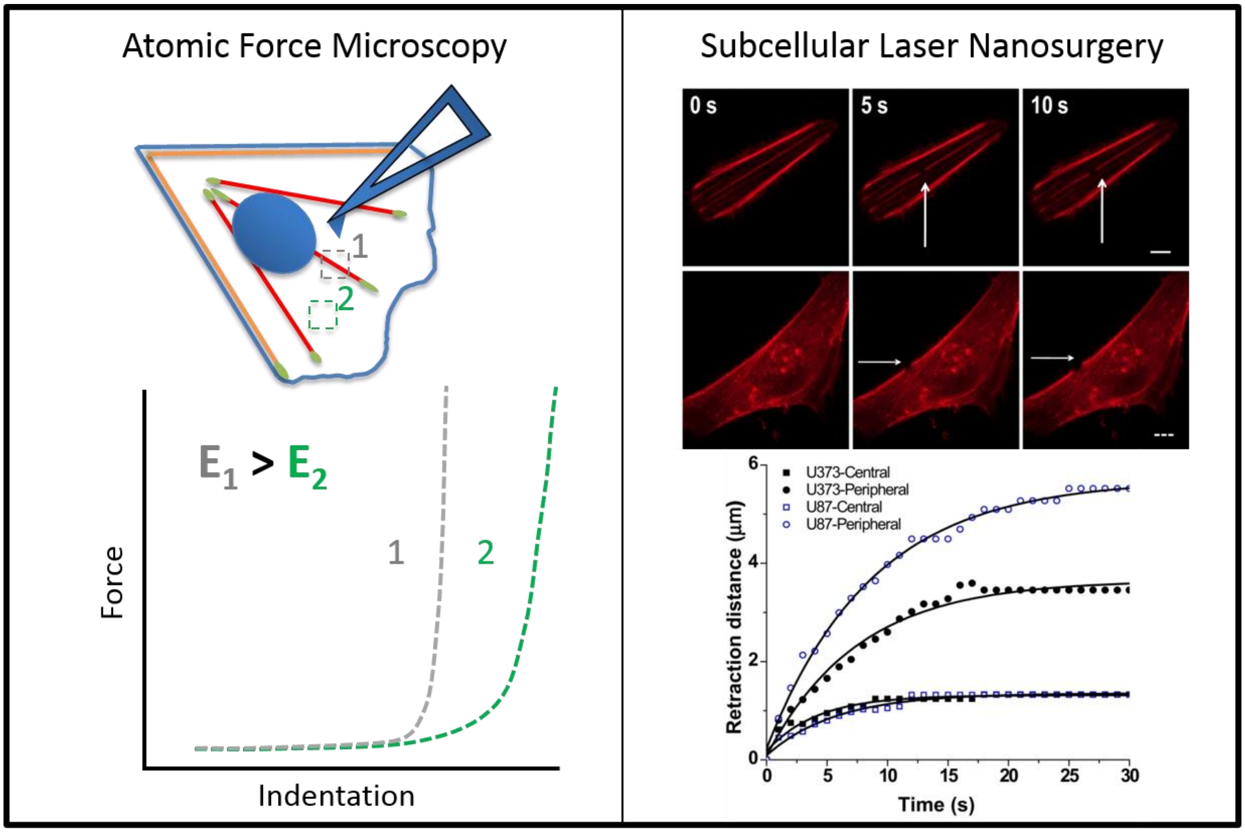

Figure 3: In vivo tools used to study stress fiber mechanical properties. Left: Atomic Force microscopy may be used to measure the stiffness of individual stress fibers within the cell. The AFM tip probes the cell surface at different locations (positions 1 and 2). The resulting force-indentation data may be fit to extract local elastic modulus values, thus allowing stiffness comparisons between the fiber and the surrounding cytoskeletal cortex (75). Right: Subcellular laser ablation allows for selective photodisruption of peripheral or central stress fibers. By following the retraction of the fiber over time and fitting it to the Kelvin-Voigt model of viscoelasticity, one can deduce effective viscoelastic properties of the severed fiber (89).

1.9 Developing biomechanical models of stress fibers using subcellular laser nanosurgery

Despite the importance of stress fibers in multiple biological processes, the molecular mechanisms that contribute to tension in stress fibers remain unclear. Part of the reason is that stress fibers in cultured cells are often found under isometric tension (i.e., constant length) and thus offer little opportunity to observe kinetic properties that may shed light on the origins of tension. Because laser nanosurgical incision of stress fibers releases this tension and provides access to retraction kinetics, these measurements have greatly promoted efforts to develop biomechanical models of stress fiber contraction (82, 85, 90, 91).

While macroscale, continuum descriptions of stress fibers (e.g. Kelvin-Voigt) continue to be useful to broadly describe viscoelastic properties (82, 88, 89), there has been increasing interest in creating models that incorporate various levels of microscale detail, including sarcomeres. After laser ablation, the retraction of stress fibers of Swiss 3T3 fibroblasts was observed to be restricted to the proximity of the cut with new adhesions forming at the retraction end over time. The presence of focal adhesion markers along the fiber suggests that stress fibers are attached to focal adhesions along their entire length and that after ablation, zyxin is further recruited to those sites to form new adhesions (85). To mathematically model these data, one framework treated each sarcomeric unit as a viscoelastic unit, taking into consideration fiber internal viscosity and elasticity, with the addition of an elastic element that symbolizes the fiber's longitudinal crosslinking to the ECM via adhesions (85). In this model, stress fibers undergo a viscoelastic retraction that scales inversely with external crosslinking and, as a result, only sarcomeres close to the ablated site retract while others remain unaffected, leading to a highly non-uniform contraction of sarcomeres. More recently, this model was analytically solved and it was determined that friction between the cytoplasm and the stress fiber is insignificant and can be disregarded as a parameter that contributes to the viscoelastic retraction observed (92).

In contrast, Stachowiak and co-authors developed a model with no external crosslinks but high frictional coupling between the stress fiber and the cytoplasm (91). These substantial external drag forces act on the recoiling fiber and slow it down over time, leading to power-law fiber retraction kinetics with highly non-uniform contraction of individual sarcomeres. Sarcomeres close to the ablated side retract faster than those further away due to the increased drag force. Since there are no external crosslinks, all sarcomere-like structures eventually collapse to a minimum size determined by the overlapping distance of myosin and actin filaments. More recently, the authors explored the relationship between stress fiber recoil after natural rupture (not induced by laser nanosurgery) and the overlapping distance of myosin and actin filaments more deeply (93). Experimental data obtained by observing the natural rupture rate of stress fibers (0.03 breaks/min per cell) further suggested the absence of external crosslinks, supporting the model described above (33). In addition, a new model was proposed where after severing, actin overlap within sarcomeres is negligible, allowing all sarcomeres to contract with minimal actin disassembly. As the sarcomeres contract further, however, they reach a minimum contraction distance where the overlapping distance of myosin and actin filaments builds stresses of around 3.3 pN per sarcomere. The model suggests that the presence of this stress is enough to activate a mechanosensing feedback loop that will increase actin disassembly, causing actin filaments to shorten and the stress to be relieved (93). Both these models argue against external crosslinking and, as a result, all sarcomeres eventually contract (91, 93).

Unlike the high non-uniformity of sarcomeric contraction observed in the two models discussed above, another study reported a two-phase sarcomeric contraction after stress fiber ablation in endothelial cells: an instantaneous initial decrease, followed by a linear contraction of sarcomeres at constant speed (90). Inhibition of myosin with blebbistatin (a myosin ATPase inhibitor) after severing of the fiber yielded no elastic recovery, in agreement with the results obtained by Katoh et al, who showed that isolated stress fibers cannot relax after contracting in a myosin dependent manner (50). These observations would seemingly argue that stress fiber tension generation cannot be fully accounted for by models that formulate stress fibers as elastic elements in parallel with viscous elements (82, 85, 88, 89). Based on these data, a model was proposed in which stress fiber tension is determined only by myosin contractility within each individual sarcomere-like unit. Due to the near instantaneous initial retraction, there is no external viscosity or crosslinking that limits the rate of contraction after severing.

Table 1: Overview of stress fiber biomechanical models based on data obtained from subcellular laser nanosurgery.

	Viscoelastic model[86]	**Progressive Linear Collapse Model**[90]	**Progressive Inhomogeneous Collapse Model**[91]
Stress fiber retraction	Decreasing exponential	Decreasing exponential	Decreasing exponential
Sarcomere Retraction	Decreasing exponential	Linear	Time dependent ½ Power law
Do all sarcomeres collapse?	No – only ones close to ablated side	Yes	Yes
Viscosities considered	Internal + External	Internal	Internal + External
External Crosslinking	Yes	No	No
Tension generation	Borne entirely due to myosin contractility	Borne due to the elasticity of the fiber and myosin contractility	Borne due to the elasticity of the fiber and myosin contractility

The disparate predictions of these models may reflect the fact that they are built from data obtained from heterogeneous combinations of cells, matrix formulations, and stress fiber populations (see Table 1). This exemplifies a broader challenge in interpreting subcellular laser nanosurgery data, as stress fibers vary dramatically in their length, connectivity, and position within the cell, making it challenging to reconcile data obtained in living cells with idealized models of single stress fibers. Constraining stress fiber geometry with single-cell micropatterning may represent a potential solution to this problem.

1.10 Conclusions

Advances in molecular biology, imaging and biochemistry have provided a rich diversity of tools and insights into the contractile mechanisms of stress fibers. Each of these approaches has its complementary strengths and limitations. Reconstitution of actomyosin bundles from purified proteins provides a simplified *in vitro* system that allows one to quantitatively study how specific proteins contribute to bundle assembly and contractility. While this approach yields unmatched control over molecular composition, it inevitably cannot capture all elements that would be found in cellular stress fibers. In a similar way, stress fibers extracted from cells are presumably structurally complete but lack connections to the cytoplasm and other cytoskeletal networks that may contribute in unforeseeable ways to the mechanics of the structure. This in turn has motivated the development of strategies for measuring stress fiber mechanics in living cells, including AFM and subcellular laser nanosurgery, both of which may be combined with advanced fluorescence methodologies to yield insight into the origins and functional contributions of stress fiber tension.

Despite these important advances, a number of key questions and challenges remain. First, how are the mechanical properties of whole stress fibers connected to their microscale, sarcomeric organization? The spatial orientation of actin filaments across stress fiber subtypes as well as within individual stress fibers vary between motile and non-motile cells (94). For example, as described earlier, within the same stress fiber of a migrating cell, barbed ends of actin filaments present at the ends of a stress fiber are directed towards focal adhesions whereas the middle regions of the same stress fiber have a mixed actin filament orientation, suggesting that the middle region is highly contractile (25). Conversely, stress fibers of non-motile cells often exhibit a sarcomeric-like pattern throughout the length of the fiber. How do these structural differences translate to force generation and how do they affect the overall function of the fiber in cell migration? Do geometric parameters such as stress fiber length and width play a role?

Another important question centers around the compartmentalization of stress fiber populations within the cell, and how this compartmentalization is associated with differential regulatory control of NMMII activation in peripheral and central stress fibers via MLCK and ROCK respectively (89, 95). In addition to the studies discussed earlier, inhibition of ROCK blocked myosin phosphorylation and formation of focal adhesions at the center in gerbil fibroma cells whereas inhibition of MLCK resulted in loss of myosin phosphorylation at the periphery of the cell (96). It is currently not clear how this compartmentalization originates – are ROCK and MLCK found at different regions in the cell or are ROCK and MLCK preferentially activated at different regions of the cell? Evidence has begun to emerge to support the idea that ROCK and MLCK preferentially promote phosphorylation of NMMIIA or IIB (97). Taken together with the differences in mechanochemical function between the two myosin isoforms, findings such as these begin to explain regional differences in stress fiber contractility in different parts of the cell. Clearly, much more work is required to determine the specific roles of NMMIIA and IIB and their differential regulation mechanism.

It is also unclear how site-specific phosphorylation of NMMII contributes to force generation, and how this in turn contributes to overall stress fiber contractile properties. As described earlier, each RLC has multiple phosphorylation sites that control myosin activity, with phosphorylation of serine 19 activating the motor domain and phosphorylation of threonine 18 and serine 19 enhancing ATPase activity (98). Mono-phosphorylation of RLC has been observed throughout the cell whereas di-phosphorylation is found at the rear of the cell where MLCK seems to preferentially activate myosin (99). Do ROCK and MLCK phosphorylate different sites on the RLC and how does the force generated from a mono-phosphorylated myosin motor differ quantitatively from that of a di-phosphorylated myosin motor? From current evidence, it seems that differential control of stress fibers via ROCK and MLCK translates to differential mechanical properties of stress fibers. It will be extremely interesting to examine in more detail the molecular mechanisms responsible for this preferential control and determine functional contributions of each myosin activator to cell-scale force-dependent properties such as cell-ECM tensional homeostasis and cellular migration.

Finally, much remains to be learned about the differential mechanics and structural contributions of stress fibers in the context of migration. As discussed earlier, our understanding of the assembly mechanisms and evolution of stress fibers during migration has advanced dramatically over the past decade due to the application of increasingly sophisticated live-cell imaging technologies. It will be interesting to explore further the molecular mechanisms that allow stress fibers to evolve from one type to the next and investigate how their mechanical properties change over time during migration. Super resolution imaging, which has already proven fruitful for visualizing the organization of structural and motor proteins within stress fibers (21), could be combined in creative ways with reconstituted actomyosin systems and subcellular laser nanosurgery to provide answers.

1.11 Acknowledgments

EK gratefully acknowledges the support of the Howard Hughes Medical Institute International Student fellowship. SK gratefully acknowledges support from the NIH Physical Sciences–Oncology Center Award (1U54CA143836); the NSF (CAREER Award CMMI 1055965) and the NIH (1R21EB016359).

1. Wozniak MA, Chen CS (2009) Mechanotransduction in development: a growing role for contractility. *Nat Rev Mol Cell Biol* 10(january):34–43.
2. Blanchoin L, Boujemaa-Paterski R, Sykes C, Plastino J (2014) Actin dynamics, architecture, and mechanics in cell motility. *Physiol Rev* 94(1):235–63.
3. Fletcher DA, Mullins RD (2010) Cell mechanics and the cytoskeleton. *Nature* 463(7280):485–92.
4. DuFort CC, Paszek MJ, Weaver VM (2011) Balancing forces: architectural control of mechanotransduction. *Nat Rev Mol Cell Biol* 12(5):308–19.
5. Kraning-Rush CM, Carey SP, Califano JP, Smith BN, Reinhart-King CA (2011) The role of the cytoskeleton in cellular force generation in 2D and 3D environments. *Phys Biol* 8(1):15009.
6. Naumanen P, Lappalainen P, Hotulainen P (2008) Mechanisms of actin stress fibre assembly. *J Microsc* 231(3):446–454.
7. Pellegrin S, Mellor H (2007) Actin stress fibres. *J Cell Sci* 120(Pt 20):3491–9.
8. Tomasek JJ, Haaksma CJ, Schwartz RJ, Howard EW (2013) Whole animal knockout of smooth muscle alpha-actin does not alter excisional wound healing or the fibroblast-to-myofibroblast transition. *Wound Repair Regen* 21(1):166–176.
9. Goffin JM, et al. (2006) Focal adhesion size controls tension-dependent recruitment of alpha-smooth muscle actin to stress fibers. *J Cell Biol* 172(2):259–68.

10. Wipff PJ, Rifkin DB, Meister JJ, Hinz B (2007) Myofibroblast contraction activates latent TGF-beta1 from the extracellular matrix. *J Cell Biol* 179(6):1311–1323.

11. Tomasek JJ, Gabbiani G, Hinz B, Chaponnier C, Brown R a (2002) Myofibroblasts and mechano-regulation of connective tissue remodelling. *Nat Rev Mol Cell Biol* 3(5):349–63.

12. Darby IA, Laverdet B, Bonte F, Desmouliere A (2014) Fibroblasts and myofibroblasts in wound healing. *Clin Cosmet Investig Dermatol* 7:301–311.

13. Evans ND, Oreffo ROC, Healy E, Thurner PJ, Man YH (2013) Epithelial mechanobiology, skin wound healing, and the stem cell niche. *J Mech Behav Biomed Mater* 28:397–409.

14. Gudjonsson T, Adriance MC, Sternlicht MD, Petersen OW, Bissell MJ (2005) Myoepithelial cells: their origin and function in breast morphogenesis and neoplasia. *J Mammary Gland Biol Neoplasia* 10(3):261–272.

15. Sopel M (2010) The myoepithelial cell: Its role in normal mammary glands and breast cancer. *Folia Morphol (Warsz)* 69(1):1–14.

16. Burridge K, Wittchen ES (2013) The tension mounts: stress fibers as force-generating mechanotransducers. *J Cell Biol* 200(1):9–19.

17. Tojkander S, Gateva G, Lappalainen P (2012) Actin stress fibers - assembly, dynamics and biological roles. *J Cell Sci* 125(Pt 8):1855–64.

18. Vicente-Manzanares M, Ma X, Adelstein RS, Horwitz AR (2009) Non-muscle myosin II takes centre stage in cell adhesion and migration. *Nat Rev Mol Cell Biol* 10(11):778–90.

19. Wylie SR, Chantler PD (2008) Myosin IIC: A Third Molecular Motor Driving Neuronal Dynamics. *Mol Biol Cell* 19(1):3956–3968.

20. Takaoka M, Saito H, Takenaka K, Miki Y, Nakanishi A (2014) BRCA2 phosphorylated by PLK1 moves to the midbody to regulate cytokinesis mediated by nonmuscle myosin IIC. *Cancer Res* 74(5):1518–1528.

21. Beach JR, et al. (2014) Nonmuscle myosin II isoforms coassemble in living cells. *Curr Biol* 24(10):1160–6.

22. Raab M, et al. (2012) Crawling from soft to stiff matrix polarizes the cytoskeleton and phosphoregulates myosin-II heavy chain. *J Cell Biol* 199(4):669–83.

23. Vicente-Manzanares M, Newell-Litwa K, Bachir AI, Whitmore LA, Horwitz AR (2011) Myosin IIA/IIB restrict adhesive and protrusive signaling to generate front-back polarity in migrating cells. *J Cell Biol* 193(2):381–96.

24. De La Cruz EM, Ostap EM (2004) Relating biochemistry and function in the myosin superfamily. *Curr Opin Cell Biol* 16(1):61–7.

25. Cramer LP, Siebert M, Mitchison TJ (1997) Identification of novel graded polarity actin filament bundles in locomoting heart fibroblasts: implications for the generation of motile force. *J Cell Biol* 136(6):1287–305.

26. Murrell MP, Gardel ML (2012) F-actin buckling coordinates contractility and severing in a biomimetic actomyosin cortex. *Proc Natl Acad Sci* 109(51):20820–20825.

27. Bidone TC, Tang H, Vavylonis D (2014) Dynamic Network Morphology and Tension

Buildup in a 3D Model of Cytokinetic Ring Assembly. *Biophys J* 107(11):2618–2628.

28. Winkelman JD, Bilancia CG, Peifer M, Kovar DR (2014) Ena/VASP Enabled is a highly processive actin polymerase tailored to self-assemble parallel-bundled F-actin networks with Fascin. *Proc Natl Acad Sci* 111(11):4121–6.
29. Mitchison TJ (1992) Actin based motility on retraction fibers in mitotic PtK2 cells. *Cell Motil Cytoskeleton* 22(2):135–151.
30. Burridge K, Wittchen ES (2013) The tension mounts: stress fibers as force-generating mechanotransducers. *J Cell Biol* 200(1):9–19.
31. Tzima E (2006) Role of small GTPases in endothelial cytoskeletal dynamics and the shear stress response. *Circ Res* 98(2):176–85.
32. Hoffman LM, Jensen CC, Chaturvedi A, Yoshigi M, Beckerle MC (2012) Stretch-induced actin remodeling requires targeting of zyxin to stress fibers and recruitment of actin regulators. *Mol Biol Cell* 23(10):1846–59.
33. Smith M a, et al. (2010) A zyxin-mediated mechanism for actin stress fiber maintenance and repair. *Dev Cell* 19(3):365–76.
34. Peterson LJ, et al. (2004) Simultaneous stretching and contraction of stress fibers in vivo. *Mol Biol Cell* 15(July):3497–3508.
35. Burnette DT, et al. (2014) A contractile and counterbalancing adhesion system controls the 3D shape of crawling cells. *J Cell Biol* 205(1):83–96.
36. Chapin LM, Blankman E, Smith MA, Shiu Y-T, Beckerle MC (2012) Lateral communication between stress fiber sarcomeres facilitates a local remodeling response. *Biophys J* 103(10):2082–92.
37. Chapin LM, Edgar LT, Blankman E, Beckerle MC, Shiu Y-T (2014) Mathematical modeling of the dynamic mechanical behavior of neighboring sarcomeres in actin stress fibers. *Cell Mol Bioeng* 7(1):73–85.
38. Kilian K a, Bugarija B, Lahn BT, Mrksich M (2010) Geometric cues for directing the differentiation of mesenchymal stem cells. *Proc Natl Acad Sci U S A* 107(11):4872–4877.
39. Zemel A, Rehfeldt F, Brown AEX, Discher DE, Safran SA (2010) Optimal matrix rigidity for stress-fibre polarization in stem cells. *Nat Phys* 6(6):468–473.
40. Hotulainen P, Lappalainen P (2006) Stress fibers are generated by two distinct actin assembly mechanisms in motile cells. *J Cell Biol* 173(3):383–94.
41. Kovac B, Teo JL, Mäkelä TP, Vallenius T (2013) Assembly of non-contractile dorsal stress fibers requires α-actinin-1 and Rac1 in migrating and spreading cells. *J Cell Sci* 126(Pt 1):263–73.
42. Oakes PW, Beckham Y, Stricker J, Gardel ML (2012) Tension is required but not sufficient for focal adhesion maturation without a stress fiber template. *J Cell Biol* 196(3):363–74.
43. Parsons JT, Horwitz AR, Schwartz M a (2010) Cell adhesion: integrating cytoskeletal dynamics and cellular tension. *Nat Rev Mol Cell Biol* 11(9):633–43.
44. Gateva G, Tojkander S, Koho S, Carpen O, Lappalainen P (2014) Palladin promotes

assembly of non-contractile dorsal stress fibers through VASP recruitment. *J Cell Sci* 127(Pt 9):1887–98.

45. Vicente-Manzanares M, Koach MA, Whitmore L, Lamers ML, Horwitz AF (2008) Segregation and activation of myosin IIB creates a rear in migrating cells. *J Cell Biol* 183(3):543–54.

46. Tee YH, et al. (2015) Cellular chirality arising from the self-organization of the actin cytoskeleton. *Nat Cell Biol* 17(February):445–457.

47. Kojima H, Ishijima a, Yanagida T (1994) Direct measurement of stiffness of single actin filaments with and without tropomyosin by in vitro nanomanipulation. *Proc Natl Acad Sci U S A* 91(26):12962–6.

48. Akiyoshi K., Toshio Y. (1988) Force measurements by micromanipulation of a single actin filament by glass needles. *Nature* 334:74–76.

49. Liu X, Pollack GH (2002) Mechanics of F-actin characterized with microfabricated cantilevers. *Biophys J* 83(5):2705–15.

50. Katoh K, Kano Y, Masuda M, Onishi H, Fujiwara K (1998) Isolation and contraction of the stress fiber. *Mol Biol Cell* 9(7):1919–38.

51. Deguchi S, Ohashi T, Sato M (2006) Tensile properties of single stress fibers isolated from cultured vascular smooth muscle cells. *J Biomech* 39(14):2603–10.

52. Tan JL, et al. (2002) Cells lying on a bed of microneedles : An approach to isolate mechanical force. *Proc Natl Acad Sci U S A* 100(4):1484–1489.

53. Spicer SS (1951) Gel formation caused by adenosinetriphosphate in actomyosin solutions. *J Biol Chem* 190:257–267.

54. Ebashi S, Ebashi F (1964) A New Protein Component Participating in the Superprecipitation of Myosin B. *J Biochem* 55(6).

55. Weber A, Winicur S (1961) The Role of Calcium in the Superprecipitation of Actomyosin. *J Biol Chem* 236:3198–3202.

56. Bendix PM, et al. (2008) A quantitative analysis of contractility in active cytoskeletal protein networks. *Biophys J* 94(8):3126–36.

57. Stachowiak MR, et al. (2012) Self-organization of myosin II in reconstituted actomyosin bundles. *Biophys J* 103(6):1265–74.

58. Thoresen T, Lenz M, Gardel ML (2011) Reconstitution of contractile actomyosin bundles. *Biophys J* 100(11):2698–705.

59. Murrell M, Thoresen T, Gardel M (2014) Reconstitution of contractile actomyosin arrays. *Methods Enzymol* 540:265–82.

60. Thoresen T, Lenz M, Gardel ML (2013) Thick filament length and isoform composition determine self-organized contractile units in actomyosin bundles. *Biophys J* 104(3):655–65.

61. Ciobanasu C, Faivre B, Le Clainche C (2014) Actomyosin-dependent formation of the mechanosensitive talin-vinculin complex reinforces actin anchoring. *Nat Commun* 5:3095.

62. Miyazaki M, Chiba M, Eguchi H, Ohki T, Ishiwata S (2015) Cell-sized spherical

confinement induces the spontaneous formation of contractile actomyosin rings in vitro. *Nat Cell Biol* 17(4):480–489.

63. Katoh K, Kano Y, Noda Y (2011) Rho-associated kinase-dependent contraction of stress fibres and the organization of focal adhesions. *J R Soc Interface* 8(56):305–11.
64. Katoh K, et al. (2001) Rho-kinase-mediated contraction of isolated stress fibers. *J Cell Biol* 153(3):569–84.
65. Katoh K, Kano Y, Amano M, Kaibuchi K, Fujiwara K (2001) Stress fiber organization regulated by MLCK and Rho-kinase in cultured human fibroblasts. *Am J Physiol Cell Physiol* 280:1669–1679.
66. Costa KD, Hucker WJ, Yin FC-P (2002) Buckling of actin stress fibers: a new wrinkle in the cytoskeletal tapestry. *Cell Motil Cytoskeleton* 52(4):266–74.
67. Nagayama K, Matsumoto T (2008) Contribution of actin filaments and microtubules to quasi-in situ tensile properties and internal force balance of cultured smooth muscle cells on a substrate. *Am J Physiol Cell Physiol* 295:1569–1578.
68. Sato K, Adachi T, Matsuo M, Tomita Y (2005) Quantitative evaluation of threshold fiber strain that induces reorganization of cytoskeletal actin fiber structure in osteoblastic cells. *J Biomech* 38(9):1895–901.
69. Brangwynne CP, et al. (2006) Microtubules can bear enhanced compressive loads in living cells because of lateral reinforcement. *J Cell Biol* 173(5):733–41.
70. Soiné JRD, et al. (2014) Model-based traction force microscopy reveals diferential tension in cellular actin bundles. *PLoS Comput Biol*.
71. Wang JH-C, Lin J-S (2007) Cell traction force and measurement methods. *Biomech Model Mechanobiol* 6(6):361–71.
72. Haga H, et al. (2000) Elasticity mapping of living fibroblasts by AFM and immunofluorescence observation of the cytoskeleton. *Ultramicroscopy* 82:253–258.
73. Rotsch C, Radmacher M (2000) Drug-induced changes of cytoskeletal structure and mechanics in fibroblasts: an atomic force microscopy study. *Biophys J* 78(1):520–35.
74. Costa KD, Sim AJ, Yin FC-P (2006) Non-Hertzian approach to analyzing mechanical properties of endothelial cells probed by atomic force microscopy. *J Biomech Eng* 128(2):176–84.
75. Lu L, Oswald SJ, Ngu H, Yin FC-P (2008) Mechanical properties of actin stress fibers in living cells. *Biophys J* 95(12):6060–71.
76. Berns W, Strahs R, Biology C (1979) Laser microirradiation of stress fibers and intermediate filaments in non-muscle cells from cultured rat heart. *Exp Cell Res* 119(2):31–45.
77. Koonce MP, Strahs KR, Berns MW (1982) Repair of laser-severed stress fibers in myocardial non-muscle cells. *Exp Cell Res* 141:375–384.
78. Berns MW (2007) History of laser scissors. *Methods Cell Biol* 82.
79. Vogel A, Venugopalan V (2003) Mechanisms of Pulsed Laser Ablation of Biological Tissues. *Chem Rev* 103(2):577–644.

80. Heisterkamp A, et al. (2005) Pulse energy dependence of subcellular dissection by femtosecond laser pulses. *Opt Express* 13(10):3690–6.

81. Ronchi P, Terjung S, Pepperkok R (2012) At the cutting edge : applications and perspectives of laser nanosurgery in cell biology. *Biol Chem* 393(April):235–248.

82. Kumar S, et al. (2006) Viscoelastic retraction of single living stress fibers and its impact on cell shape, cytoskeletal organization, and extracellular matrix mechanics. *Biophys J* 90(10):3762–73.

83. Berkeley F Sanjay Kumar Departm ent and University : M anuel Thery Départem ent et Université : Institut de Recherche en Technologies et Sciences pour Address : Budget : Funding Requested From UC or French Partner None Beginning : None End : N / A.

84. Yoshigi M, Hoffman LM, Jensen CC, Yost HJ, Beckerle MC (2005) Mechanical force mobilizes zyxin from focal adhesions to actin filaments and regulates cytoskeletal reinforcement. *J Cell Biol* 171(2):209–15.

85. Colombelli J, et al. (2009) Mechanosensing in actin stress fibers revealed by a close correlation between force and protein localization. *J Cell Sci* 122(11):1928–1928.

86. Lele TP, Pendse JAY, Kumar S, Salanga M, Karavitis J (2006) Mechanical Forces Alter Zyxin Unbinding Kinetics Within Focal Adhesions of Living Cells. *J Cell Physiol* 207:187–194.

87. Grashoff C, et al. (2010) Measuring mechanical tension across vinculin reveals regulation of focal adhesion dynamics. *Nature* 466:263–6.

88. Chang C-W, Kumar S (2013) Vinculin tension distributions of individual stress fibers within cell-matrix adhesions. *J Cell Sci* 126(Pt 14):3021–30.

89. Tanner K, Boudreau A, Bissell MJ, Kumar S (2010) Dissecting regional variations in stress fiber mechanics in living cells with laser nanosurgery. *Biophys J* 99(9):2775–83.

90. Russell RJ, Xia S-L, Dickinson RB, Lele TP (2009) Sarcomere mechanics in capillary endothelial cells. *Biophys J* 97(6):1578–85.

91. Stachowiak MR, O'Shaughnessy B (2009) Recoil after severing reveals stress fiber contraction mechanisms. *Biophys J* 97(2):462–71.

92. Besser A, Colombelli J, Stelzer EHK, Schwarz US (2011) Viscoelastic response of contractile filament bundles. *Phys Rev E* 83(5):51902.

93. Stachowiak MR, et al. (2014) A mechanical-biochemical feedback loop regulates remodeling in the actin cytoskeleton. *Proc Natl Acad Sci U S A* 111(49). doi:10.1073/pnas.1417686111.

94. Deguchi S, Sato M (2009) Biomechanical properties of actin stress fibers of non-motile cells. *Biorheology* 46(2):93–105.

95. Katoh, Kazuo, Kano Yumino, Amano Mutsuki KK and FK (2001) Stress fiber organization regulated by MLCK and Rho-kinase in cultured human fibroblasts.

96. Totsukawa G, et al. (2000) Distinct roles of ROCK (Rho-kinase) and MLCK in spatial regulation of MLC phosphorylation for assembly of stress fibers and focal adhesions in 3T3 fibroblasts. *J Cell Biol* 150(4):797–806.

97. Sandquist JC, Swenson KI, Demali KA, Burridge K, Means R (2006) Rho Kinase Differentially Regulates Phosphorylation of Nonmuscle Myosin II Isoforms A and B during Cell Rounding. *J Biol Chem* 281:35873–35883.

98. Umemoto S, Bengur a R, Sellers JR (1989) Effect of multiple phosphorylations of smooth muscle and cytoplasmic myosins on movement in an in vitro motility assay. *J Biol Chem* 264(3):1431–6.

99. Vicente-Manzanares M, Horwitz AR (2010) Myosin light chain mono- and di-phosphorylation differentially regulate adhesion and polarity in migrating cells. *Biochem Biophys Res Commun* 402(3):537–42.

Chapter 2. Geometry and network connectivity govern the mechanics of stress fibers

2.1 Abstract

Actomyosin stress fibers (SFs) play key roles in driving polarized motility and generating traction forces, yet little is known about how tension borne by an individual SF is governed by SF geometry and its connectivity to other cytoskeletal elements. We now address this question by combining single-cell micropatterning with subcellular laser ablation to probe the mechanics of single, geometrically defined SFs. Intriguingly, retraction length of geometrically isolated SFs after cutting depends strongly on SF length, demonstrating for the first time that longer SFs dissipate more energy. Furthermore, when cell geometry and adhesive spacing are fixed, cell-to-cell heterogeneities in SF dissipated elastic energy can be predicted from varying degrees of physical integration with the surrounding network. We apply genetic, pharmacological and computational approaches to demonstrate a causal and quantitative relationship between SF connectivity and mechanics for patterned cells and show that similar relationships hold for non-patterned cells allowed to form cell-cell contacts in monolayer culture. Remarkably, dissipation of a single SF within a monolayer induces cytoskeletal rearrangements in cells long distances away. Finally, stimulation of cell migration leads to characteristic changes in network connectivity that promote SF bundling at the cell rear. Our findings demonstrate that SFs both influence and are influenced by the networks in which they reside. Such higher-order network interactions contribute in unexpected ways to cell mechanics and motility.

2.2 Significance Statement

Actomyosin stress fiber (SF) networks transmit tension to the microenvironment, which contributes to cell shape and tissue assembly. However, virtually nothing is known about how SF geometry and network structure control the ability of an SF to generate tension. We normalized cell shape and SF length with micropatterning and used laser ablation to probe the viscoelastic properties of the resulting standardized SFs. We find that retraction dynamics of a cut SF is strongly regulated by its length and this relationship may be amplified or offset by the orientation of the attached SFs in single cells as well as in a monolayer. Thus, SF force generation is controlled both locally via adhesive geometry and globally via connections to the actin network.

2.3 Introduction

Actomyosin stress fibers (SFs) enable mammalian cells to generate traction forces against the extracellular matrix (ECM) (1–3). These forces are increasingly recognized to play central roles in the regulation of cell shape, migration, and stem cell fate decisions (1, 4). At the multicellular level, these forces also contribute significantly to tissue morphogenesis, wound healing, and neoplasia (5, 6). SFs are composed of F-actin, structural proteins such as α-actinin, and, frequently, non-muscle myosin II (NMMII) (2, 7). When NMMII filaments are present, these structures generate tension that is transmitted along the length of the SF to ECM adhesions, surrounding SFs, and other connected structural elements such as the actin cortex, microtubules, intermediate filaments and the nucleus (8). As such, SFs are capable of acting both locally and globally through their networked interactions with other cellular structures to impose tensile loads within the cell (9). This notion is a critical yet largely unexplored linchpin in current models of cell motility, where specific SF subsets are thought to coordinate tensile activities to direct remodeling of ECM adhesions and sculpt migratory processes (1, 10, 11).

The increasing appreciation of SFs as important players in cell mechanics and motility has stimulated great interest in measuring the contractile properties of individual SFs. Several techniques have been used over the past two decades, spanning two broad categories. The first and more reductionist category includes characterization of SFs extracted from cells (12) or reconstituted from molecular components (13). The second category includes characterization of SFs in living cells such as subcellular laser ablation (SLA) which allows for the mechanical interrogation of single SFs (3). We and others have applied SLA to determine the viscoelastic contraction of sarcomeric structures within SFs (14–16) and tension distribution after SF ablation to focal adhesion (FAs) throughout the cell (9). Moreover, SLA has been used to spatially map SF viscoelastic properties within the cell and associate activities of specific NMMII activators and isoforms to these subpopulations (17, 18).

An important, emergent theme from these studies is that the effective mechanical contributions of an SF depend strongly on its geometry and structural context, although these relationships remain largely uninvestigated and controversial. Cellular heterogeneity represents a critical barrier to clarifying this since cultured cells adopt a variety of morphologies giving rise to a poorly controlled diversity of SF geometries. Thus, it is challenging to understand fundamental material properties of SFs, including how length and ECM adhesivity regulate elastic recoil. This heterogeneity has also frustrated efforts to understand how single SF mechanics are related to the network properties in which they reside, even though this interconnectedness is broadly understood to play essential roles in cellular structure and motility.

2.4 Results

Single-cell ECM micropatterning represents a valuable tool for accomplishing this goal. The ability of this technology to arbitrarily standardize cell geometry has dramatically improved the field’s understanding of how cell shape controls traction force, cytoskeletal architecture, proliferation/apoptosis, and stem cell fate (8, 19, 20). Micropatterning has also been used to prescribe the geometry of peripheral SFs (21–23). We reasoned that we could productively exploit micropatterning approaches to control cell and SF geometry in combination with SLA and thereby gain new insights into SF mechanics. We were first interested in determining how SF length regulates viscoelastic retraction. To accomplish this, we designed three fibronectin (FN)-coated U-shaped patterns, i.e. patterns consisting of a rectangular frame of matrix with one long edge missing, of aspect ratios 1.5, 1.9 and 3.0 using a UV photopatterning strategy (Fig. 1A and last column of Fig. 1B-C) (24). This strategy produced SFs of similar thickness with two terminal FAs and a length closely conforming to that of the pattern edge across all aspect ratios (Appendix I - Fig. S1 and last column of Fig. 1B-C). We then applied SLA on SFs along the FN-free edge and observed their retraction kinetics. As in our previous studies, we fit each retraction curve to a Kelvin-Voigt viscoelastic cable model described by a time constant (τ), which reflects the SF's effective viscosity/elasticity ratio, and a plateau retraction distance (L_o), which correlates to the elastic energy dissipated by half of the severed SF (3, 17, 18) (Fig.1D) (see Appendix I – Text and Fig. S2 for model choice). The retraction kinetics of these SFs exhibited a clear length dependence, with both L_o and τ ($p<0.01$, Dunn test for non-parametric multiple comparison) increasing with length (Appendix I - Fig. S1). On the contrary, SFs produced on FN-filled rectangular patterns showed no statistical variation in dissipated elastic energy (L_o) or τ with SF length (Appendix I - Fig. S3) due to the presence of vinculin-positive FAs along the SF length, which pin the SF and prevent it from freely retracting (14). Thus, dissipated SF elastic energy and viscoelastic properties depend strongly on adhesive spacing, with longer SFs storing more elastic energy. These results validate indirect predictions from earlier micropattern-based studies on the elastic nature of SFs (21–23).

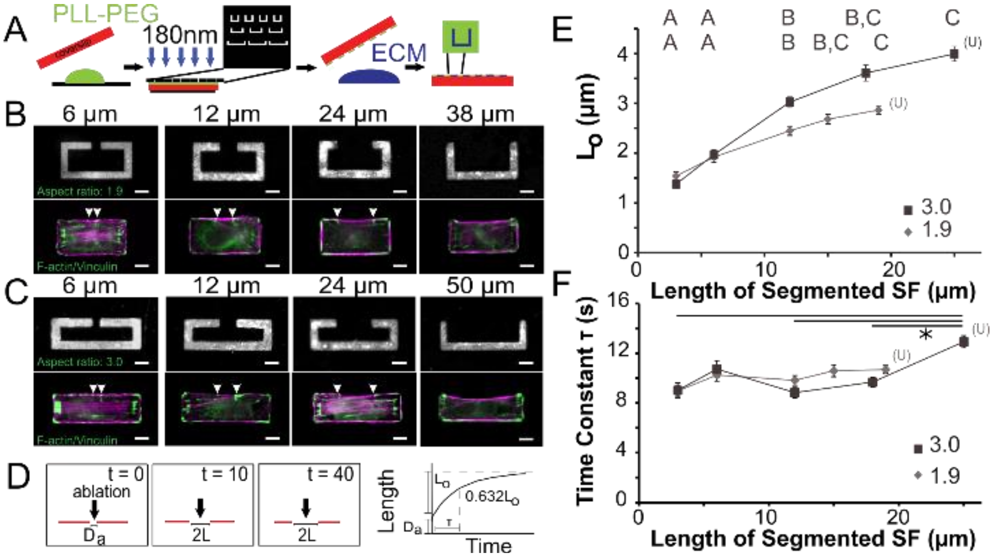

Figure 1: Dissipation of elastic energy in severed SFs depends on fiber length. To elucidate SF mechanics and SF length relationships for fixed cell geometry, we created "spacing patterns" in which cells are cultured on patterns consisting of a rectangular frame that contains a variable-length gap. **A**, Schematic of pattern fabrication. **B**, Top row: FN distribution on patterns of aspect ratio 1.9 with gap lengths ranging from 6 µm to 24 µm. Bottom row: Distribution of F-actin (magenta) and vinculin (green) in U2OS cells seeded on the corresponding patterns. A length-defined SF is formed across the gap with focal adhesions formed at the ends. Gap ends depicted by white arrows. **C**, Top row: FN stain on patterns of aspect ratio 3.0. Bottom row: F-actin and vinculin distributions. **D**, SF Retraction analysis. D_a - SF material destroyed by ablation, 2L - distance between fiber ends over time (L is the retraction distance of a severed SF fragment). Length L vs time t is fit to the Kelvin-Voigt model to determine $L_{o,}$ whose magnitude correlates with the SF's dissipated elastic energy, and τ, the viscoelastic time constant which is the ratio of viscosity/elasticity. **E**, Average L_o values for each pattern. A, B and C statistical families show differences $p<0.05$ determined using Dunn test for multiple comparisons of non-normally distributed data. **F,** Average τ values for each pattern. * indicate statistical differences of $p < 0.05$ using Kruskal-Wallis followed by Dunn test. (N= 27, 58, 89, 72 and 126 for each spacing of aspect ratio 1.9, N=13, 21, 38, 40 and 120 for each spacing of aspect ratio 3.0). Data points at 19 µm (aspect ratio 1.9) and 25 µm (aspect ratio 3.0) correspond to the U-shaped patterns (replotted from Fig. S1). Note that for the Kelvin-Voigt model, we measure the retraction of one end of the cut fiber and as such, SF length is halved. Scale bars = 10 µm.

Earlier studies have shown that when area is conserved, cellular pre-stress increases with aspect ratio, raising concerns that these differences could contribute to the observed length-dependence (19, 25). However, when we measured whole-cell RMS traction and strain energy on the varying aspect ratio U-shaped patterns, we did not observe differences (Appendix I - Fig. S4) (26). Nevertheless, to directly probe for SF mechanics rather than whole-cell pre-stress, we designed patterns in which the two parallel arms of the U are symmetrically but incompletely connected with matrix (spacing patterns), leaving a gap of defined length (6 µm, 12 µm, 24 µm and 30 µm for aspect ratio 1.9 and 6 µm, 12 µm, 24 µm and 36 µm for aspect ratio 3.0). Cells form single SFs across the gap, with FAs present at the edge of each SF (Fig. 1B-C). Dissipated elastic energy released by an SF (corresponding to L_o) does indeed scale with length, whereas τ remains relatively constant (Fig. 1E-F). The length-sensitivity of L_o decreases with increased SF length, which may be due to subtle differences in matrix geometry, SF connectivity, or pre-stress across these patterns. Additionally, at higher SF lengths, we observe differences in the elastic energy dissipated by SFs of equal length within cells of different aspect ratios (Appendix I - Fig. S5 for primary data).

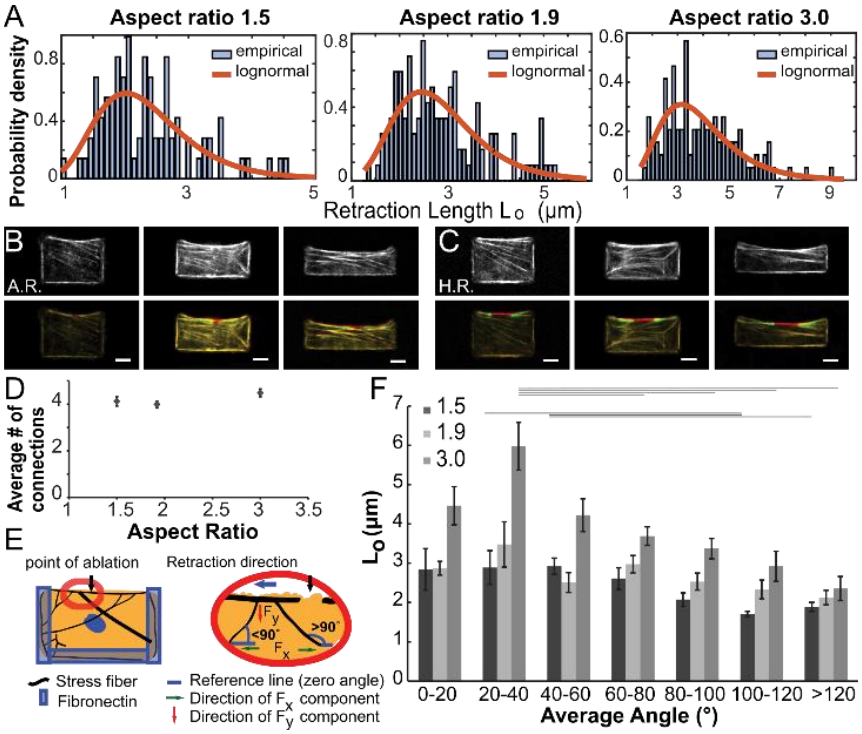

Figure 2: Analysis of L_o distributions of U-shaped patterns reveals that elastic energy dissipation is heterogeneous and depends on network connectivity. A, Probability density histograms of L_o on each U-shaped pattern fit to a lognormal distribution. **B**, Top panel: Pre-ablation F-actin distribution (RFP-LifeAct) of average retracting (A.R.) cells whose L_o values fall under the peak. Bottom panel: Overlay of F-actin distribution before (red) and after (green) ablation. **C**, Top panel: Pre-ablation F-actin distribution of highly retracting (H.R.) cells whose L_o values fall under the tail of the fit. Bottom panel: Overlay of actin network before (red) and after (green) ablation. **D**, Dependence of number of connecting fibers to length-defined SF does not reveal statistical differences (N= 66, 94, 103 for each aspect ratio respectively, ANOVA followed by Tukey). Error bars represent SEM. **E**, Schematic depicting angles with which the connecting fibers intersect the severed length-defined fiber. If the angle is between 0º-90º, its cosine is positive and corresponds to an x-component of the force (F_x) (green arrow) parallel to the direction of retraction (blue arrow). If the angle is between 90º-180º, its cosine is negative resulting to an F_x that is against retraction direction. Each cell is assigned an average angle value. **F**, Correlation between observed L_o and average angle for a given cell. Bars are mean ± SEM, lines portray statistical differences determined using ANOVA followed by Tukey ($p<0.05$). Scale bars = 10 µm.

As noted earlier, a key motivation for using single-cell micropatterning was to standardize SF geometry and facilitate the development of relationships between SF length and viscoelasticity. Despite this effort, we still observed experimental variation in SF retraction. Identifying remaining sources of heterogeneity could potentially yield valuable and unappreciated regulatory principles underlying SF mechanics. Indeed, when we examined our retraction distributions more closely, we noted that the L_o values were highly skewed on U-shaped patterns of all aspect ratios (Fig. 2A). The distributions closely follow log normal distributions, with most cells falling under the peak and some cells falling under the long, right-sided tail of the fit (Fig. 2A, Appendix I - Table S1). The appearance of a log normal distribution suggests that SF mechanical properties depend on their growth history. When we more closely inspected pre- and post-ablation RFP-LifeAct images for cells found under the peak (average retracting (A.R.)) and under the long tail (highly retracting (H.R.)) (Fig. 2B-C, Appendix I - Fig. S6), we noted broad, cell-to-cell structural heterogeneities in the SF networks surrounding the target fiber. This in turn led us to hypothesize that variations in network structure might contribute to heterogeneities in SF viscoelasticity. We counted the number of SF connections to the length-defined SF (SF formed across the pattern gap) and found no statistical difference in the number of connections as a function of aspect ratio (Fig. 2D). We then asked whether the orientation of these connected SFs varies across cells. We hypothesized that connecting SFs apply a force on the length-defined SF whose y-component ($F_{y,}$ red arrow) is always downwards and whose x-component ($F_{x,}$ green row) depends on the intersecting angle (Fig. 2E). Differences in angular distributions can presumably determine whether these connections and their corresponding forces are enhancing or impeding retraction. We calculated the average angle distribution per cell and binned the L_o values based on the average angle measurements (see Appendix I - Fig. S7 for examples of angle analysis). We first observed that for average angles >90°, L_o values are smaller when compared to angles <90°, possibly due to the presence of an F_x value that is in the opposite direction of retraction (Fig. 2F). As the average angle distribution increases from 0° to 90°, we observed an increase in L_o that peaks around 20°- 40°. The presence of a peak suggests that retraction kinetics are affected by both the F_x and F_y imposed by connecting SFs. The angle of the connecting SF, therefore, contributes to dissipated elastic energy (L_o).

To experimentally test a causal role for SF connectivity in driving retraction, we performed gain- and loss-of-function studies with the myosin activator Rho-associated kinase (ROCK), which has been shown to govern SF assembly and contractility within the cellular interior, including the connecting SFs seen here. By contrast, peripherally located SFs such as the ones severed in our experiments are primarily regulated by myosin light chain kinase (MLCK) and are thus expected to be minimally perturbed by ROCK manipulation (17, 18). To suppress ROCK activity and dissipate central connections, we treated cells with 5 μM Y-27632. To enhance ROCK activity and strengthen connections, we stably overexpressed a constitutively active mutant of ROCK that is induced by doxycycline (CA-ROCK) (27) (Appendix I - Fig. S8). Immunostaining of FAs and SFs confirmed the increase of FA size in the presence of CA-ROCK and reduction in SF and FA formation in the presence of Y-27632 (Fig. 3A). In the absence of doxycyline, CA-ROCK cells have similar FAs to naïve cells. Doxycycline addition induced the assembly of numerous SFs connected to the length-defined SF whereas Y-27632-treated cells exhibited fewer connections (Fig. 3B-C). The average number of connections per cell increased with CA-ROCK expression compared to naïve and Y-27632 treated cells (Fig. 3D). To understand how these manipulations might influence the total F_y and F_x, we quantified the cell-to-cell distribution of the sums of the sines ($\sum \sin\alpha$ for F_y) and cosines ($\sum \cos\alpha$ for F_x) of the angles of intersection as defined earlier. Compared to naïve cells, Y-27632 treatment shifted the $\sum \sin\alpha$ distribution to smaller values for all aspect ratios, whereas CA-ROCK expression shifted the distribution to larger values (Fig. 3E, *=$p<0.05$, **=$p<0.001$). Similarly, Y-27632 treatment produced shifts to slightly more negative values for $\sum \cos\alpha$ and CA-ROCK overexpression led to more positive values (Fig. 3F *=$p<0.05$ and **=$p<0.001$). When we performed SLA, we found that Y-27632 treatment reduced elastic energy dissipation (L_o) for all aspect ratios (relative to naïve) and muted pattern to pattern differences. Conversely, CA-ROCK overexpression increased dissipated elastic energy compared to naïve ($p<0.05$ for 1.9 and 3) and enhanced pattern-to-pattern differences (Fig. 3G). With no doxycycline, CA-ROCK cells exhibited similar L_o values to naïve U2OS RFP LifeAct (Appendix I - Fig. S8). In parallel experiments, we found that wholesale inhibition of myosin II with blebbistatin reduced retraction distance while also producing an inward deflection of the length-defined SF (Appendix I - Fig. S9). This finding, together with our previous results, is consistent with our hypothesis that the viscoelastic properties of an SF are governed both by its own axial geometry and that of the network to which it connects.

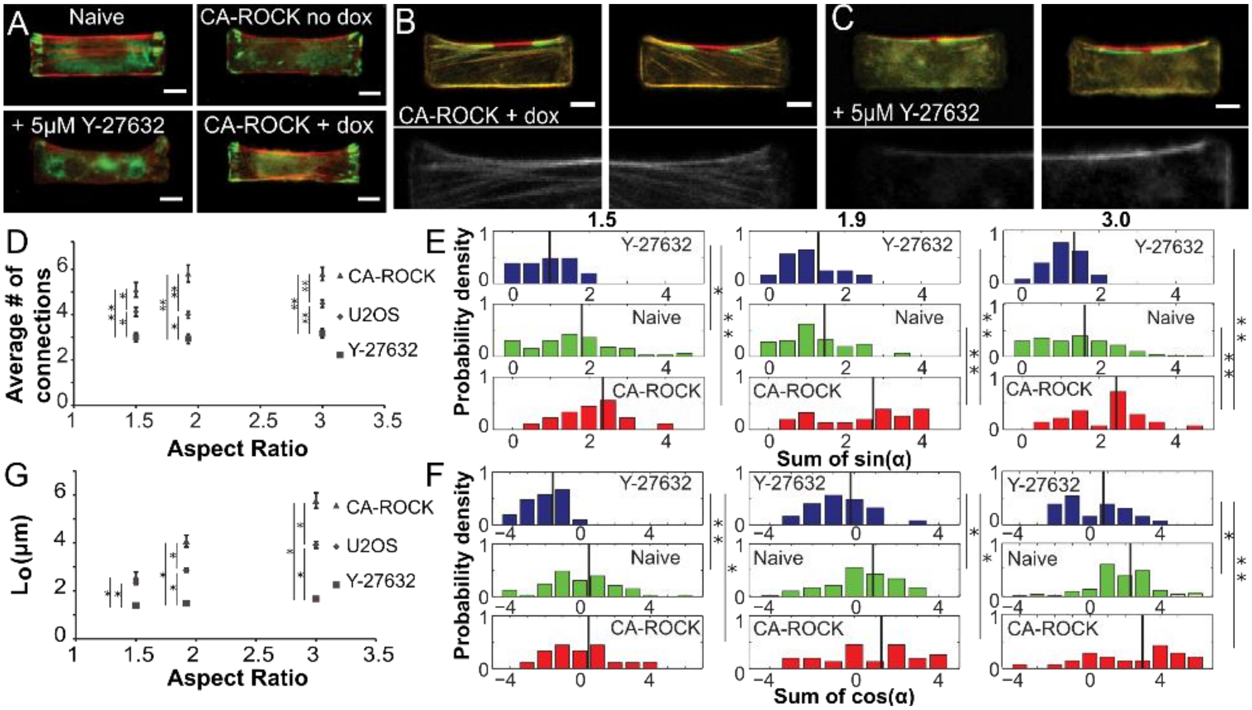

Figure 3: Network control of SF retraction is regulated by Rho-associated kinase-mediated assembly of connecting fibers. A, Focal adhesion (green) and SF (red) distributions in naïve U2OS, U2OS pSLIK CA ROCK ± doxycycline, and Y-27632 treated U2OS cells (U-shaped patterns, aspect ratio 3.0). **B-C**, Effect of CA ROCK and Y-27632 on SF architecture. Top panels: SF distributions before (red) and after (green) ablation. Bottom panels: High-magnification images of connecting fibers to length-defined SF. **D**, Quantification of the average number of connecting fibers per cell (N for Y-27632 = 21, 27 and 28 and N for induced CA-ROCK = 20, 33 and 30 respectively for each aspect ratio). Data points represent mean ± SEM. Statistical comparisons performed using ANOVA followed by Tukey (* = $p<0.05$, **=$p<0.001$). Data points for U2OS are transposed from Fig. 2D. **E-F**, Histograms of $\sum \sin\alpha$ and $\sum \cos\alpha$ values per cell obtained for Y-27632, Naïve and induced CA-ROCK cells per aspect ratio. Black lines depict the mean value. Statistical comparisons of cosine and sine distributions within same aspect ratio were performed using ANOVA followed by Tukey (* = $p<0.05$, ** = $p<0.001$). **G**, L_o for cells treated with Y-27632 (rectangles), induced CA-ROCK (triangles) and naïve (diamonds) on each aspect ratio. N for Y-27632= 21, 26 and 45 and N for induced Ca-ROCK = 18, 33, 30 for each aspect ratio respectively. Data points are mean ± SEM. Statistical differences calculated using Dunn test for multiple comparison of non-normal data (* = $p<0.01$). Scale bars = 10 µm.

To investigate causal relationships between network architecture and SF mechanics more precisely, we developed a simple mechanical model of networked elastic cables subjected to external force (Fig. 4A) (28, 29). Shapes and forces of peripheral SFs in the absence of connecting SFs have been previously described with the tension-elasticity model (TEM) (21). Peripheral SFs show a circularly invaginated shape due to the force balance of an elastic line tension λ and a homogenous surface tension σ (Fig. S10). We extended this model by including internal SFs that connect to the peripheral one and exert a force F_o at a prescribed angle α (see Appendix I text). To simplify the model, we first considered a symmetric cell with one connecting SF at each side. Numerical solution of the system produces a distribution of F_{center} values with a peak at $\alpha \sim 70^o$, reminiscent of the experimental observations. We explored the sensitivity of this solution to model parameters by varying the geometry of the system (connection point as determined by $l_{1,o}$), the active force (F_o), and the fiber stiffness EA (Fig. 4B). If the angle α is close to 0^o or 180^o, moving the connection points closer to the center (large $l_{1,o}$), does not affect the force calculated. At higher α, however, the force increases with increased $l_{1,o}$ (Fig. 4B top). In contrast, varying the active force F_o changes both the basal and maximal force values (Fig. 4B middle). Changing the SF stiffness leaves the force levels unchanged for both large and small α (Fig. 4B bottom). Based on this simple symmetric model, we conclude that the magnitude of F_o is not the sole determinant for predicting the dissipated elastic energy of a length-defined SF. Instead, the force F_o has both an x-component in the direction of retraction and a y-component in the normal direction that pulls on the severed SF. This pull distends the retracting SF, introducing an additional elastic component that further enhances retraction. Without this y-component force and the additional spring, SFs would retract maximally at $\alpha=0$, a prediction not consistent with our experimental observations. The presence of this elastic force is further confirmed by our experimental observation that the length-defined SF moves outward following SLA of the internal connecting fibers showing that connecting fibers contribute through pre-stress (Appendix I - Fig. S11).

To further understand how connecting fibers contribute to local retraction *within* a single SF, we photobleached fiduciary markers in a single SF, photoablated the SF, and followed the retraction of each inter-marker segment. When an SF fragment was highly connected at acute angles, SF segments within that fragment retracted more than those in the non-connected SF fragment (Appendix I - Fig. S12A and C). However, when a SF fragment was connected at large angles (>90°), SF segments underwent smaller retraction than the non-connected SF fragment (Appendix I - Fig. S12B). Based on our results and our simple active cable model, we conclude that differences in the location and angle of connecting fibers can explain cell to cell heterogeneities in the elastic energy dissipated by SFs after SLA.

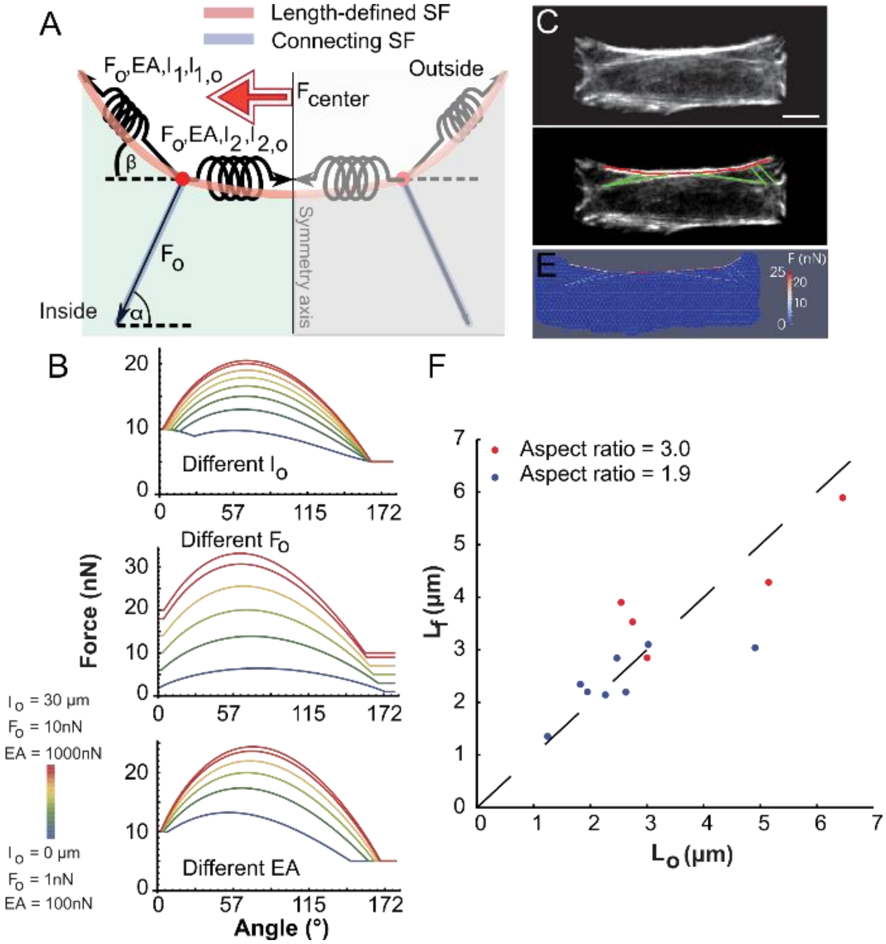

Figure 4: An active cable network (ACN) model recapitulates key experimental results. A, Symmetric model in which connecting SFs are modeled as exerting an active force F_o and defined-length SFs are modeled as active elastic cables. **B,** Parametric studies relating the magnitude of F_{center} to changes in geometry ($l_{1,o}$), SF active tension (F_o) and SF stiffness (EA). All curves exhibit the same shape and show that intermediate angles (60°-100°) support the greatest force, which is due to the additional elastic component of the length-defined SF from the pull of the internal F_o that stretches the spring of the length-defined SF. **C-E,** Segmentation process of the ACN model. U2OS RFP-LifeAct images obtained prior to laser ablation were manually segmented and SF network simulations are created as discussed in SI text. **F,** Plot of simulated retraction lengths L_f (y-axis) against experimentally derived retraction lengths L_o (x-axis). (N = 8 and 5 for aspect ratios 1.9 and 3.0 respectively). Parameters used for ACN: F_o = 4 nN, EA = 40nN at aspect ratio 1.9 and F_o = 7 nN, EA = 80nN at aspect ratio 3.0.

The symmetry inherent in our model (Fig. 4A) represents a major simplification of cellular SF networks. To test whether this reasoning could be extended to more complex experimentally observed SF distributions, we manually traced the location and angle of connecting SFs in a population of cells and generated a triangular mesh network that embeds the SFs as marked edges (Fig. 4C-E). For illustration, we calculated the equilibrium force distribution for the length-defined SF using active force F_o= 5 nN and EA = 500 nN. As shown in Fig. 4E, although a connecting SF adds only 5 nN of active force, the total force in the length-defined SF is as high as 25 nN at the center where SLA occurs and exhibits a heterogeneous energy distribution depending on the connecting SFs. To find optimal parameters for both active force and stiffness, we carried out active cable network simulations based on two data sets (n = 8 and n = 5 cells cultured on U-shaped patterns with aspect ratio of 1.9 and 3.0 respectively). Within each data set, we used the same parameters for all cells. Thus, the differences in the predicted forces between cells on the same pattern arise solely from the geometry of the internal SF distribution. To convert forces retrieved from the model to retraction distances L_f using a simple spring model (k

= 3 nN/µm), we adjusted F_o and EA for all cells in the data set to achieve optimal agreement with experiments. We found that connecting SF geometries are sufficient to explain the differences in retraction within each data set (Fig. 4F), though not with the same parameters for both aspect ratios. In contrast, we observed that SFs are both stiffer ($EA_{r=1.9}$ = 40 nN compared to $EA_{r=3.0}$ = 80 nN) and more contractile ($F_{o,r=1.9}$ = 4 nN and $F_{o,r=3.0}$ = 7 nN) at aspect ratio 3.0. Thus, a simple model that considers SF networks as a series of connected elastic cables enables us to dissect differences in the mechanical properties of SFs and accurately predict the retracted distance of a peripheral SF based only on its connections to other SFs.

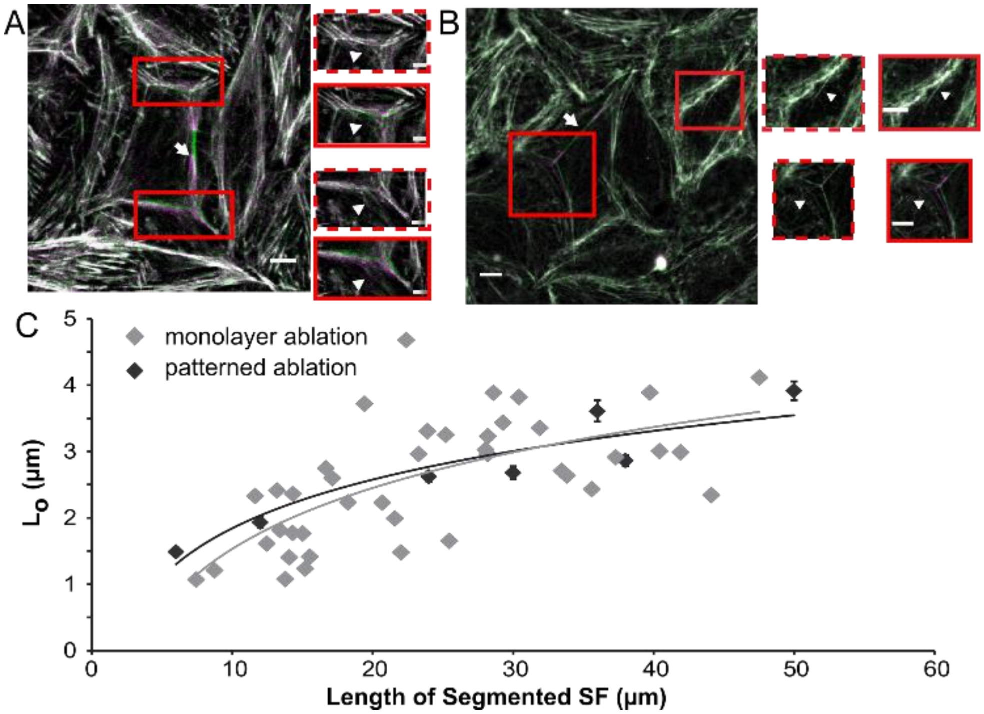

Figure 5: Dissipation of elastic energy in a monolayer setting is related to fiber length and connectivity. To elucidate whether the relationships uncovered using patterned single cells hold true in non-patterned cells, we performed SLA of SF of cells grown as a monolayer. A and B, Examples of an ablated SF within cells that are growing in a monolayer. Overlay of cells before (green) and after ablation (magenta). Solid red boxes show overlay of images before (green) and after (magenta) ablation. Dashed red boxes show overlay of images taken at different times with no ablation to control for any SF movement during imaging. Arrowheads within solid red boxes point to regions of increased SF network rearrangement. In B, the ablated SF is highly connected and therefore undergoes large retraction which leads to SF network rearrangements within cells further away from the site of ablation (arrowheads within solid red boxes). C, Overlay of patterned single cell retraction kinetics (data transposed from Fig. 1E) and monolayer ablation retraction kinetics (grey triangles). Both single cell and monolayer ablation results exhibit similar relationships between fiber length and dissipated elastic energy after ablation. Scale bars = 10 µm for all images except zoomed-in images in A where scale bars = 5 µm.

To test whether the concepts developed with patterned single cells can also be extended to multicellular structures in which SF networks may be physically integrated across several cells, we performed SLA on cells grown in a monolayer (Fig.5A-B). Quantification of retraction kinetics showed that the relationship between SF length and retraction distance observed in patterned single cells (Fig. 1E) holds true in a monolayer setting: increasing SF length leads to increased $L_{o,}$ reaching an eventual plateau (Fig. 5C). Remarkably, the effect of connectivity is amplified in the presence of cell-cell adhesions, as evidenced by the transmission of tension release from the targeted cell to its nearest neighbors. In some instances, this tension release is felt within distant cells tens of micrometers away (Fig. 5B).

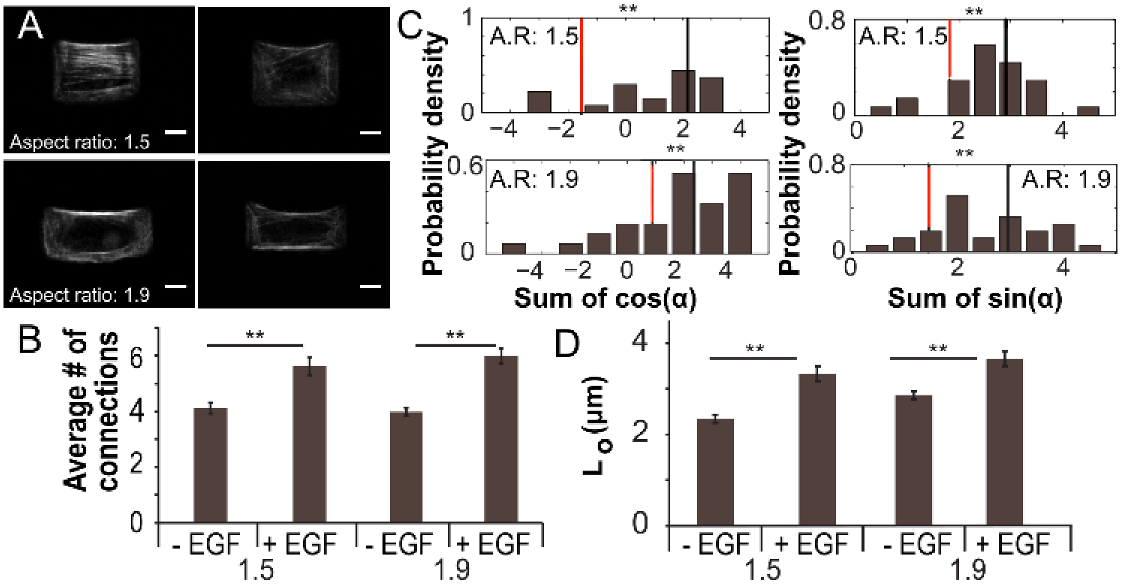

Figure 6: U2OS RFP-LifeAct cells treated with EGF acquire a motile phenotype where the "rear" SF exhibits increased connectivity and increased elastic energy. A, U2OS RFP-LifeAct cells seeded on U-patterns treated with EGF. **B,** Quantification of the average number of connecting fibers per cell (N for EGF treatment = 27 and 31 respectively for each aspect ratio). Data points represent mean ± SEM. Statistical comparisons performed using Two-way student t-test (** = $p<0.001$). **C,** Histograms of $\sum \cos \alpha$ (left) and $\sum \sin \alpha$ (right) values per cell obtained for EGF treated cells grown on U patterns of aspect ratio 1.5 (top) and aspect ratio 1.9 (bottom). Black lines depict the mean value of EGF treated cells and red lines depict the mean value of non EGF treated (averages transposed from Fig. 3E and F). Statistical comparisons of cosine and sine distributions within same aspect ratio were performed using Two-way student t-test (**=$p<0.001$). **D,** L_o for cells treated with EGF on each aspect ratio. N = 44 and 48 for EGF-treated cells for each aspect ratio respectively. Data points are mean ± SEM. Statistical differences calculated using Two-way student t-test (** = $p<0.001$). Data for no EGF treated cells is transposed from Fig. S1. Scale bars = 10 μm.

Finally, we wondered whether changes in SF connectivity might contribute to broader cell-scale functions such as directional motility. To study the effect of connectivity on migration, we stimulated patterned cells using Epidermal Growth Factor (EGF) to initiate the formation of migratory processes (20). When cells grown on the spacing patterns of aspect ratio 1.9 were EGF-stimulated, migratory processes were formed in ways that depended on the gap length (Appendix I - Fig. S13): for small gaps, migratory processes were formed at either the spacing side or the FN side whereas for larger gaps, migratory processes only formed at the FN side leading to a polarized cell with a rear SF. Moreover, the rear SFs of EGF-stimulated cells on U-shaped patterns (aspect ratio 1.5 and 1.9) exhibited increased connectivity with more internal SFs connecting to them (Fig. 6A-B). When comparing the average angle distribution of naïve versus EGF-treated cells, we observed a decrease in the average angle, which suggests that under EGF treatment, cells rearrange their SF networks to both increase the number of connections and align these connecting SFs at more acute angles (Appendix I - Fig. S14). Connectivity analysis revealed increases in both $\sum \cos \alpha$ and $\sum \sin \alpha$ distributions for both aspect ratios (Fig. 6C, **=$p<0.001$) due to both the change in the angle of connecting fibers as well as the increase in the number of connections. Based on the broader force distributions, we hypothesized and observed that the rear SF of EGF-treated cells dissipate increased elastic energy after ablation (Fig. 6D, **=$p<0.001$). Our results suggest that as the cell is induced to migrate, SF connectivity evolves to suit the tensile/contractile needs of the rear SF, resulting in changes in SF mechanical properties as measured by SLA.

2.5 Discussion

In this study, we have combined single-cell micropatterning and SLA in a novel way to elucidate how SF geometry and connections within a complex network alter the elastic energy dissipated by an SF. Previous studies have produced several models that suggest that retraction length scales with SF length but make no predictions on how SF contractility and stiffness vary with SF length (14–16). Our results show that the relationship between SF length and dissipated elastic energy after SLA is more complex than previously appreciated and offers new insights into this intricate relationship.

First, simulations demonstrate for the first time that longer SFs are stiffer and more contractile – a result that would not be predicted by existing SF models. Second, we do not find a simple linear increase, as suggested by simple mathematical models for SF retraction (see Appendix I text), but a decrease in slope with increasing SF length. This is a novel insight that could be due to the interconnectedness of the actin SF network. Our study shows for the first time that the presence of internal connections leads to inhomogeneous retraction within the same SF as well as heterogeneities across standardized cells. In addition to producing pre-stress on the length-defined SF, differences in connectivity may also affect τ due to differences in drag force, in that a highly-connected SF pulls a greater subset of the actin cytoskeleton as it retracts, effectively increasing viscous drag (Appendix I - Fig. S15). Our results directly show that connecting fibers, rather than the viscosity of the cytosol, dominate the viscous component of the retraction, thereby resolving an important open-ended question in the field of single SF mechanics (15).

Furthermore, when we cut single SFs in a monolayer setting, we observed tension release and SF rearrangement in distant cells. Recent work has suggested that transmission of contractile forces between cells critically regulates collective migration and durotaxis. Much of the evidence for this concept has been indirectly inferred from TFM and whole cell genetic and pharmacological manipulations of cadherins and myosin (30–33). Our findings now provide direct evidence that single cytoskeletal structures in cells mediate tensile forces over long distances across a monolayer. Our results also provide mechanistic insight into how aggregates of cells can cooperatively generate huge traction forces, which is important in collective cell migration and matrix remodeling (30).

Although our cable network model was quite minimalistic and only incorporated a small portion of the cytoskeletal network, it successfully predicted key experimental results and achieved remarkable quantitative agreement with the experimental results for specific cells. This suggests that cellular geometry and SF network properties are the primary drivers of SF viscolelastic retraction, whatever other cell-to-cell variations in structure or mechanics may exist. Precisely how SF network heterogeneities arise and evolve represents an important open question, and it is possible that this may be a function of the cell's adhesive and spreading history. Indeed, our findings complement the recent, elegant demonstration that patterning reconstituted actomyosin network architecture can modulate contractility (34). Development of analogous micropatterning strategies for living cells may make it possible to test the hypotheses raised in our study by engineering the details of the internal SF network through strategic placement of adhesions.

2.6 Materials and Methods

Cell lines and reagents: Viral particles of the pFUG-RFP-LifeAct vector were packaged in 293T cells and used to infect U2OS cells (ATCC HBT-96) (35). Cells expressing the pFUG-RFP-LifeAct vector were sorted on a DAKO-Cytomation MoFlo High Speed Sorter based on RFP fluorescence. Myc tagged p160ROCK Δ3 (kindly provided by Shuh Narumiya, Kyoto University, Japan) was subcloned into the lentiviral vector pSLIK containing the TRE tight doxycycline-inducible promoter (27). U2OS RFP LifeAct cells were further stably transduced with the pSLIK vector at an MOI of 0.5 IU/cell. Cells were sorted based on RFP and Venus fluorescence. Cells were cultured in DMEM with 10% fetal bovine serum (JR scientific), 1% penicillin/strep (Thermo Fischer Scientific) and 1% Non-Essential Amino Acids (Life Technologies). Y-27632 2HCL was from Selleck Chemicals, doxycycline and blebbistatin were purchased from Sigma Aldrich. Epidermal Growth Factor (EGF) was obtained from R&D Systems and was used at 100ng/ml. Cells were stimulated with EGF for at least 2 hours and 30 minutes before ablation.

Deep-UV based pattern fabrication: Chrome quartz photomasks were designed using CleWin 4.0 and were printed from aBeam technologies (Hayward, CA). Patterns were made as described elsewhere (24). Briefly, glass coverslips were coated with 0.01mg/ml PLL-PEG (Surface Solutions, Switzerland) in 10mM HEPES pH=7.4 for 1 hour. After drying with air, coverslips were exposed to deep UV (UVO cleaner, Jelight, USA) through a photomask. A drop of water was used to hold the coverslips on the photomask and care was taken to remove any excess liquid and air bubbles. After Deep UV incubation, coverslips were placed in DI water and left to incubate for at least 30 minutes. Coverslips were then incubated with 34.25µg/ml of fibronectin (EMD Millipore Corporation) in 10mM HEPES pH=8.5 for 1 hour at 37° (Fig. 1A). Patterns were washed 3 x for 5 min in phosphate-buffered saline (PBS) before cells were plated.

Confocal Imaging of immunofluorescence and SF photo-disruption: Immunostaining imaging and SF SLA experiments were performed on a Zeis LSM 510 Meta Confocal microscope equipped with a MaiTai Ti:sapphire femtosecond laser (Spectra Physics, Newport Beach, CA) (9, 17, 18). U2OS RFP-LifeAct cells were seeded on patterns and allowed to spread for 3 hours. Media was changed to Live Cell Imaging Solution (Invitrogen) prior to experiment. For SF photodisruption, the femtosecond laser was used at 770nm resulting in an energy deposition of 1-2 nJ on a single stress fiber (9, 17, 18). SLA experiments were performed between 3-6 hours after cell seeding. All images were acquired with a 40x water-dipping objective (N.A = 0.8). For Y-27632 experiments, 5 µM of Y-27632 was added 2 hours after seeding and for blebbistatin, 10 µM was added 3 hours after seeding for 1 hour and 30 minutes. CA-ROCK cells were cultured in doxycycline for two days prior to experiments.

Data analysis of SF retraction: SF retraction distance was recorded every 1.96 seconds for 43 seconds following SLA. Retraction dynamics were obtained through tracking of the two ends in ImageJ. Results were then fit to a Kelvin-Voigt model

$$L = D_a + L_o\left(1 - \exp\left(-\frac{t}{\tau}\right)\right) \qquad (22)$$

where L is defined as half the distance between the two severed ends, D_a is the length of SF destroyed by ablation, L_o is the retraction plateau distance and τ is the viscoelastic time constant determined using CurveFit, MATLAB. Note that this equation is the same as Eq. 4, discussed above. $L_o$is proportional to the ratio of pre-stress to elasticity of the fiber, whereas τ is the ratio of viscosity to elasticity (9, 17). Connections to the length-defined SF were manually traced using confocal images of U2OS RFP-LifeAct cells and angles were obtained using ImageJ (Fig. S7).

Monolayer laser ablation: A 35 mm glass bottom dish (MaTek corporations) was coated with 25 µg/ml fibronectin diluted in phosphate-buffered saline (PBS) and incubated at 37˚ for at least 30 minutes. Dishes were washed with PBS before use. 200,000 U2OS RFP-LifeAct cells were seeded and allowed to grow until the dish surface was fully covered. Laser ablation was performed and analyzed as described before.

Western blots: U2OS RFP-LifeAct pSLIK CA-ROCK cells were cultured in 150ng/ml doxycycline for 2 days prior to lysis. U2OS RFP LifeAct cells were incubated in 5µM Y-27632 for 1 and 3 hours prior to lysis. As described previously, cells were lysed in RIPA buffer with phosphatase and protease inhibitors (EMD Millipore, Billerica, MA) (27). Protein content was measured by BCA and used to normalize samples before loading. Lysates were boiled and run on 4-12% Bis-Tris gels and transferred onto a PVDF membrane. The following primary antibodies were used: anti-phosphorylated myosin light chain 2 (Thre18/Ser19) (Cell Signaling Technology) and anti-GAPDH (Sigma-Aldrich, St. Louis, MO). HRP-conjugated secondary antibodies (Life Technologies, Carlsbad, CA) and ECL reagent (Thermo Fisher Scientific, Waltham, MA) were used for detection. Bands were quantified and normalized to GAPDH with the built-in gel analyzer tool in ImageJ.

Traction force microscopy: Polyacrylamide gel micropatterning was performed as described previously (25). Briefly, gels were synthesized with 7.7% acrylamide, 0.29%bis-acrylamide, 1% ammonium persulphate (APS), 0.1% TEMED and 0.5% far-red fluorescent beads (0.2µm diameter (Invitrogen)) and left to polymerize for 30 minutes on a chrome quartz photomask, treated with hexane to prevent gel sticking. After polymerization, the gel was exposed to deep UV (UVO cleaner, Jelight, USA) for 80 seconds. The gels were then incubated with 10mg/ml EDC (Thermo Fisher Scientific) and 17mg/ml NHS (Thermo Fisher Scientific) for 15 minutes. After EDC/NHS incubation, gels were incubated with 34.25µg/ml of fibronectin (EMD Millipore Corporation) in 10mM HEPES pH=8.5 for 1 hour at 37°. Gels were washed 3 x for 5 min in PBS and 2 x for 5 min in cell media. Cells were seeded on the patterns and left to spread for 6 hours prior to imaging. We computed maps of cellular traction stresses from bead positions before and after cell detachment using constrained Fourier Transform Traction Cytometry by manually drawing the cell area (9, 27).

Immunofluorescence staining: Briefly, patterned cells were fixed using 4% paraformaldehyde for 10 minutes, and washed using PBS. Cells were permeabilized in 0.5% Triton-X for 15 minutes, and blocked in 5% goat serum. We then incubated the cells with the primary antibody for 1 hour at room temperature, followed by extensive washing in 1% goat serum and secondary incubation for 1 hour at room temperature. We used the following antibodies: anti-fibronectin clone HFN 7.1 (Thermo Scientific), anti-vinculin (Sigma-Aldrich) and Alexa-Fluor 647 mouse. F-actin was stained with 546-phalloidin. Immunostaining images were obtained by one-photon confocal imaging. For presentation purposes, the contrast and brightness of fluorescence images were optimized using Image J.

2.7 Acknowledgements

This work was performed in part at the CRL Molecular Imaging Center supported by NIH 3R01EY015514-01S1. EK and CAB gratefully acknowledge the support of the Howard Hughes Medical Institute International Student and Siebel Scholar fellowships and Konrad Adenauer Foundation fellowship, respectively. This work was supported from the National Institute of Health (1R21EB016359), the National Science Foundation (CAREER Award CMMI-1055965) and the France-Berkeley Fund. CAB and USS acknowledge support by the Heidelberg Karlsruhe Research Partnership (HEiKA). USS is a member of the cluster of excellence CellNetworks and the Interdisciplinary Center for Scientific Computing (IWR). The authors acknowledge Professor Manuel Thery and Dr. Timothée Vignaud for valuable technical guidance on patterning methods.

1. Burnette DT, et al. (2014) A contractile and counterbalancing adhesion system controls the 3D shape of crawling cells. *J Cell Biol* 205(1):83–96.
2. Kassianidou E, Kumar S (2015) A biomechanical perspective on stress fiber structure and function. *Biochim Biophys Acta - Mol Cell Res* 1853(11, Part B):3065–3074.
3. Kumar S, et al. (2006) Viscoelastic retraction of single living stress fibers and its impact on cell shape, cytoskeletal organization, and extracellular matrix mechanics. *Biophys J* 90(10):3762–73.
4. Zemel A, Rehfeldt F, Brown AEX, Discher DE, Safran SA (2010) Cell shape, spreading symmetry and the polarization of stress-fibers in cells. *J Phys Condens Matter* 22(19):194110.
5. Zeng Y, et al. (2015) Formin-like2 regulates Rho/ROCK pathway to promote actin assembly and cell invasion of colorectal cancer. *Cancer Sci* 106(10):1385–1393.
6. Darby IA, Laverdet B, Bonte F, Desmouliere A (2014) Fibroblasts and myofibroblasts in wound healing. *Clin Cosmet Investig Dermatol* 7:301–311.
7. Blanchoin L, Boujemaa-Paterski R, Sykes C, Plastino J (2014) Actin dynamics, architecture, and mechanics in cell motility. *Physiol Rev* 94(1):235–63.
8. Makhija E, Jokhun DS, Shivashankar G V (2016) Nuclear deformability and telomere dynamics are regulated by cell geometric constraints. *Proc Natl Acad Sci* 113(1):E32–E40.
9. Chang C-W, Kumar S (2013) Vinculin tension distributions of individual stress fibers within cell-matrix adhesions. *J Cell Sci* 126(Pt 14):3021–30.
10. Kovac B, Teo JL, Mäkelä TP, Vallenius T (2013) Assembly of non-contractile dorsal stress fibers requires α-actinin-1 and Rac1 in migrating and spreading cells. *J Cell Sci* 126(Pt 1):263–73.
11. Tojkander S, Gateva G, Husain A, Krishnan R, Lappalainen P (2015) Generation of contractile actomyosin bundles depends on mechanosensitive actin filament assembly and disassembly. *Elife* 4:e06126.
12. Katoh K, Kano Y, Masuda M, Onishi H, Fujiwara K (1998) Isolation and contraction of

the stress fiber. *Mol Biol Cell* 9(7):1919–38.

13. Thoresen T, Lenz M, Gardel ML (2013) Thick filament length and isoform composition determine self-organized contractile units in actomyosin bundles. *Biophys J* 104(3):655–65.

14. Colombelli J, et al. (2009) Mechanosensing in actin stress fibers revealed by a close correlation between force and protein localization. *J Cell Sci* 122(11):1928–1928.

15. Stachowiak MR, O'Shaughnessy B (2009) Recoil after severing reveals stress fiber contraction mechanisms. *Biophys J* 97(2):462–71.

16. Russell RJ, Xia S-L, Dickinson RB, Lele TP (2009) Sarcomere mechanics in capillary endothelial cells. *Biophys J* 97(6):1578–85.

17. Chang C-W, Kumar S (2015) Differential Contributions of Nonmuscle Myosin II Isoforms and Functional Domains to Stress Fiber Mechanics. *Sci Rep* 5:13736.

18. Tanner K, Boudreau A, Bissell MJ, Kumar S (2010) Dissecting regional variations in stress fiber mechanics in living cells with laser nanosurgery. *Biophys J* 99(9):2775–83.

19. Rape A, Guo W, Wang Y (2011) The Regulation of Traction Force in Relation to Cell Shape and Focal Adhesions. *Biomaterials* 32(8):2043–2051.

20. Parker KK, et al. (2002) Directional control of lamellipodia extension by constraining cell shape and orienting cell tractional forces. *FASEB J* 16(10):1195–1204.

21. Bischofs IB, Klein F, Lehnert D, Bastmeyer M, Schwarz US (2008) Filamentous network mechanics and active contractility determine cell and tissue shape. *Biophys J* 95(7):3488–96.

22. Labouesse C, Verkhovsky AB, Meister J-J, Gabella C, Vianay B (2015) Cell Shape Dynamics Reveal Balance of Elasticity and Contractility in Peripheral Arcs. *Biophys J* 108(10):2437–2447.

23. Labouesse C, Gabella C, Meister J-J, Vianay B, Verkhovsky AB (2016) Microsurgery-aided in-situ force probing reveals extensibility and viscoelastic properties of individual stress fibers. *Sci Rep* 6:23722.

24. Azioune A, Carpi N, Tseng Q, Théry M, Piel M (2010) Protein micropatterns: A direct printing protocol using deep UVs. *Methods Cell Biol* 97(10):133–46.

25. Oakes PW, Banerjee S, Marchetti MC, Gardel ML (2014) Geometry Regulates Traction Stresses in Adherent Cells. *Biophys J* 107(4):825–833.

26. Mertz AF, et al. (2012) Scaling of traction forces with the size of cohesive cell colonies. *Phys Rev Lett* 108(19):1–5.

27. Wong SY, et al. (2015) Constitutive activation of myosin-dependent contractility sensitizes glioma tumor-initiating cells to mechanical inputs and reduces tissue invasion. *Cancer Res* . doi:10.1158/0008-5472.CAN-13-3426.

28. Guthardt Torres P, Bischofs IB, Schwarz US (2012) Contractile network models for adherent cells. *Phys Rev E* 85(1):11913.

29. Soiné JRD, et al. (2015) Model-based Traction Force Microscopy Reveals Differential Tension in Cellular Actin Bundles. *PLoS Comput Biol* 11(3):e1004076.

30. Sunyer R, et al. (2016) Collective cell durotaxis emerges from long-range intercellular force transmission. *Science (80-)* 353(6304):1157 LP-1161.

31. Ng MR, Besser A, Danuser G, Brugge JS (2012) Substrate stiffness regulates cadherin-dependent collective migration through myosin-II contractility. *J Cell Biol* 199(3):545 LP-563.

32. Fernandez-Gonzalez R, Simoes S de M, Röper J-C, Eaton S, Zallen JA (2016) Myosin II Dynamics Are Regulated by Tension in Intercalating Cells. *Dev Cell* 17(5):736–743.

33. Ng MR, Besser A, Brugge JS, Danuser G (2014) Mapping the dynamics of force transduction at cell–cell junctions of epithelial clusters. *Elife* 3:e03282.

34. Ennomani H, et al. (2016) Architecture and Connectivity Govern Actin Network Contractility. *Curr Biol* 26(5):616–626.

35. Lee JP, Kassianidou E, MacDonald JI, Francis MB, Kumar S (2016) N-terminal Specific Conjugation of Extracellular Matrix Proteins to 2-Pyridinecarboxaldehyde Functionalized Polyacrylamide Hydrogels. *Biomaterials* 102:268–276.

Appendix I. Supplementary text and figures for Chapter 2

AI.1 Supplementary text on theory of retraction

1) Active Kelvin-Voigt model:

Stress fibers are defined as actin-based bundles with periodic structure (1). They can be classified into different subclasses (radial, dorsal, ventral, transverse arcs, peripheral) (1–3) but all of them have a periodic arrangement of its constituents, in particular the actin crosslinker α-actinin. Here we consider contractile stress fibers, such as ventral stress fibers, that have a periodic arrangement also of myosin II minifilaments. We conclude that such stress fibers have a sarcomeric structures, similar to striated muscle (4). Because of the one-dimensional nature of the system, each sarcomere must sustain the same force and for many purposes, it is sufficient to consider one such element. Because stress fibers can maintain force over a long period of time, they seem to be dominated by the elastic element and we model them as a Kelvin-Voigt model for an elastic solid, supplemented by a contractile element (Fig. S2A) (5–9). This model has also been used before to evaluate laser cutting experiments of the actin cortex (10).

Fig. S2A shows that in an active Kelvin-Voigt model, the elastic, viscous and contractile elements are arranged in parallel, thus the force balance simply reads

$$\xi\dot{L} + kL - F_m = 0 \qquad (1)$$

where ξ is the friction coefficient, k the spring constant and F_m is the motor force. If we use a linearized force-velocity relation for the motor activity

$$F_m = F_s(1 - \frac{v}{v_o}) \qquad (2)$$

with stall force F_s, free velocity v_o and velocity $v = \dot{L}$, we see that the second part adds a constant contribution to the friction coefficient, $\xi \rightarrow \xi + \frac{F_s}{v_o}$. We define the relaxation time $\tau = \frac{\xi}{k}$ to write the force balance as

$$\tau\dot{L} + L - \frac{F_s}{k} = 0\ . \qquad (3)$$

With the appropriate initial conditions, this is solved by

$$L = D_a + \frac{F_s}{k}(1 - e^{-\frac{t}{\tau}})\ . \qquad (4)$$

Because all terms in the force balance are linear, we obtain an exponential relaxation. Eq.3 is commonly used for evaluating retraction after laser cutting and usually gives an excellent fit to the experimental data (11).

From Eq. 4 we see that the final retraction length is simply

$$L_o = \frac{F_s}{k}. \qquad (5)$$

F_s scales linear with the number of motors pulling in parallel in the actin bundle. The fact that retraction is caused by motor force F_s corresponds to the experimental observation that the myosin II inhibitor blebbistatin strongly reduces retraction (compare Fig. S9). The larger the motor force F_s, the larger is the retraction length L_o, as is the initial speed, $\dot{L}(t = 0) = \frac{F_s}{\xi}$. Because the spring constant k has been measured in SF-pulling experiments to be of the order of $3\,\frac{nN}{\mu m}$ (6) and because the typical final retraction length is $L_o = 2\ \mu m$, we can estimate the typical motor stall force as $F_s = kL_o = 6\ nN$, in agreement to earlier results (6, 12). Note that in our simple model, the system comes to a halt because compressive energy is built up in the spring. Alternatively, one might argue that it comes to a halt because the myosin motors can only pull out a finite length because they eventually reach the barbed ends of the actin filaments (6). Another potential mechanism is that the contracted SF is held by connections it its environment, e.g. the substrate or the surrounding cytoskeleton (see below).

Until now, we have assumed that before cutting the motors are stalled and that the elastic spring is relaxed. However, it is very likely that the system is pre-stressed, as suggested e.g. by analysis of cell shape on micropatterned substrates (13, 14) and by initial jumps observed in the retraction (15). We therefore now include a pre-stress in the equations:

$$\xi\dot{L} + k(L - L_1) - F_s = 0 \qquad (6)$$

thus both the motor force and the pre-stressed spring now pull on a fiber right after cutting ($L = 0$). We immediately note that the equations remain linear and we thus get the same exponential relaxation, with the only difference that $F_s \rightarrow F_s + kL_1$. For the final retraction we thus get a larger value:

$$L_o = \frac{F_s + kL_1}{k}\,. \qquad (7)$$

If we assume that the retraction after cutting is completely determined by the pre-stress ($F_s = 0$), then $L_o = L_1$. The above estimate $F_s = 6\ nN$ for the motor force now became an estimate for the force generated by the pre-stress before cutting. This would also be the force F_a transmitted to a focal adhesion holding the SF. In general, we expect the force

$$F_a = F_s + kL_1 \qquad (8)$$

transmitted to the focal adhesion to contain contributions from both motors and pre-stress. We conclude that pre-stress might be a substantial part of the force measured at the SF-endpoint (i.e. at the focal adhesion), but this cannot be deduced from the retraction kinetics, because it has the same shape both without and with pre-stress.

2) Stress fiber as contractile beam:

Until now, we did not explicitly consider the spatial extent of the stress fiber. We now consider the equations for a spatially extended beam of length l contracted locally by force dipoles P (corresponding to the bipolar myosin II minifilaments) (Fig. S2B). We introduce the spatial coordinate x ($0 \leq x \leq l$) along the beam of length l. The 1D displacement is called $u(x)$ (we do not treat the dynamic case, so there is no time t here). The final retraction length can now be identified as $L_O = |u(l)|$ (we take the modulus because $u(l)$ will be negative). Assuming a linear constitutive law, the internal tension T (stress times cross-sectional area) in the beam is

$$T(x) = Cu'(x) + P(x) \tag{9}$$

where $C = EA$ is the 1D modulus. In the following, we assume homogeneous contractility, $P(x) = const.$ Force balance dictates $T(x)' = 0$ (no external forces) and therefore

$$Cu'' = 0\ . \tag{10}$$

With the boundary condition $u(0) = 0$ and $T(l) = 0$ (no displacement at the left and free stress boundary at the right), this is solved by

$$u(x) = -\frac{P}{C}x\ . \tag{11}$$

Thus the displacement increases linearly along the beam. It is driven by internal contractility P, which is balanced by compressive energy being stored in the beam. For the final retraction length, we get

$$L_O = |u(l)| = \frac{P}{C}l \tag{12}$$

which corresponds to Eq. 5 with $k = \frac{C}{l} = \frac{EA}{l}$. We conclude that for the simplest possible stress fiber model, retraction length L_o should scale linear with stress fiber length l. We also note that with the estimate $k = 3\ \frac{nN}{\mu m}$ from above and the typical length $l = 10\ \mu m$ of the cut segment, we get $C = EA = kl = 30\ nN$ as a typical value for the 1D modulus.

Because we assume contractility P to be constant, it enters the calculation only through the boundary condition, exactly in the way an elastic pre-stress would enter, because pre-stress would be generated by an external force F pulling the beam to a certain extension. Thus like for the active Kelvin-Voigt model, we again find that it is difficult to differ between the effect of motor force and pre-stress. If we go back to Eq. 7 and again use $k = \frac{EA}{l}$, we find that the linear scaling now only followed if we could assume that $L_1 = cl$ with a constant c, meaning that the resting length exactly scales with stress fiber length l. Then we would get

$$L_o = \frac{F_s + EAc}{EA}l \tag{13}$$

and thus the final retraction length Lo should scale again linear with stress fiber length l. Of course these results only hold when both motor force F_s and stress fiber rigidity k do not show some unexpected scaling with l. Thus, the standard model for stress fibers suggests a linear scaling between retraction length and stress fiber length, even for a pre-stressed fiber. However, this result is based on many strong assumptions and experimentally there might be several reasons why this

might not be the case. In particular, it has been argued earlier that non-linear geometric effects for peripheral SFs break this kind of linear scaling (13), as also confirmed here by our computer simulations.
We next consider the force that should be exerted by a stress fiber that does not have a free end, but is attached at the end to a focal adhesion. Then we have to implement the boundary condition $T(l) = -Ku(l)$ with an external spring constant K. The solution is

$$u(x) = -\frac{P}{C+Kl}x \tag{14}$$

and the force on the boundary is

$$T(l) = \frac{Kl}{C+Kl}P = \frac{K}{k+K}P \tag{15}$$

which corresponds to two springs in series. In the limit of a stiff focal adhesion, $K \gg k$, the force on the substrate is simply P, independent of the length of the fiber. Thus for a contractile beam, P has the same function as F_s for the active Kelvin-Voigt model.

We also consider the elastic energy stored in the contractile beam. Because constant contractility P only enters through the boundary condition, the elastic energy can be written as

$$U = \int_0^l \frac{1}{2} Cu'(x)^2 dx = \frac{1}{2} Cl(\frac{P}{C})^2 = \frac{P^2}{2C} l \tag{16}$$

and thus a longer SF stores more energy. With $k = \frac{C}{l}$ and $F_s = P$, the same results follow from the active Kelvin-Voigt model with $U = \frac{{F_s}^2}{2k}$.

We finally consider the case that the beam is attached along its length to the environment through springs with spring constant per length ρ. Now the force balance reads $T' = \rho u$ and thus

$$Cu'' = \rho u\ . \tag{17}$$

Defining the decay length $\lambda = \sqrt{\frac{C}{\rho}}$, we can write

$$\lambda^2 u'' - u = 0 \tag{18}$$

With the same boundary conditions as above this is solved by

$$u(x) = -\frac{P\,\lambda}{C}\frac{\sinh(\frac{x}{\lambda})}{\cosh(\frac{l}{\lambda})} \tag{19}$$

For $\rho \to 0$, $\lambda \to \infty$, we recover the result from Eq. 11 through a Taylor expansion. For the tension in the beam, we find

$$T(x) = P(1 - \frac{\cosh(\frac{x}{\lambda})}{\cosh(\frac{l}{\lambda})} \qquad (20)$$

thus it is maximal at the left end and vanishes at the right end. For small λ, the tension at the left reaches the maximal possible value of P. In general, this calculation shows that stress will localize to the cut end if there is some connection to the environment. For the final retraction length, we find

$$L_o = |u(l)| = \frac{P\lambda}{C}\tanh(\frac{l}{\lambda}) \ . \qquad (21)$$

Thus it initially increases with beam length l, but then plateaus for large l because for a long beam, only the end parts retract, as indeed observed experimentally when the stress fiber is attached to the substrate (16). Here we consider stress fibers that are isolated from the substrate, but do have some connections to the surrounding network. Then one would also expect that the final retraction length starts to plateau with increased SF length, in agreement with our experimental findings.

AI.2 Supplementary text on symmetric model introduced in Figure 4:

1) Mathematical description:

In order to understand the effect of internal stress fibers (SFs) pulling a length-defined SF inwards, we develop a simple mechanical model of connected cables subjected to external force. The connecting SFs are modelled by an active force F_o at an angle α with the horizontal axis (Fig. S10). The length-defined SF is modelled by an active cable intersected by the connection points of the connecting SF. Further, a homogenous surface tension σ exerts a constant inwards pull along the two segments of the peripheral SF, which results in a circular shape as described previously with the tension-elasticity model (TEM) (13). Note that the curvature along the peripheral SF is discontinuous at the connection point in order to satisfy force balance. For comparison to experiments we are interested in the force F_{central}, which can be assessed if the rest lengths of the two fiber segments $l_{1,0}$ and $l_{2,0}$, the fiber stiffness EA, and the active force level F_o are known parameters.

We first identify the length of the first segment, l_1, the length of the second segment l_2, and the angle β of the tangent of the first segment with the horizontal line at the intersection point as free variables and express all other variables in terms of these three. This leads to

$$\delta_i = {}^{l_i}\!/_{2\pi R_i} \ , \quad R_i = {}^{\lambda_i}\!/_{\sigma} \ , \quad \lambda_i = EA\,\frac{l_i - l_{i,0}}{l_{i,0}} \ , \quad d_i = 2R_i \sin\left(\frac{\delta_i}{2}\right) \ ,$$

Further, we establish the geometric properties

$$\beta' = \beta + \frac{\delta_1}{2} \ , \quad \gamma' + \frac{\delta_2}{2} = \gamma \ , \quad \gamma = \delta_2 \ .$$

Note that by the last geometric property, γ is not a free variable but depends on l_2. To solve the problem, we need to find three relations between the free variables. The first two are given by the force balance equation at the connection point,

$$\overrightarrow{F_0} + \lambda_1\overrightarrow{t_1} + \lambda_2\overrightarrow{t_2} = 0$$
$$-F_0\sin\alpha + \lambda_1\sin\beta - \lambda_2\sin\gamma = 0$$

$$-F_0 \cos\alpha - \lambda_1 \cos\beta + \lambda_2 \cos\gamma = 0\,.$$

Here, $\overrightarrow{t_1}$, $\overrightarrow{t_2}$ denote the tangents of the two circle segments at the connection point C. The third relation follows from the geometrical consideration that the horizontal distance between points A and B in Fig. S10 equals the sum of the two rest lengths, $l_{1,0} + l_{2,0}$, which leads to

$$\cos\beta' = \frac{l_{1,0} + l_{2,0} - d_2 \cos\gamma'}{d_1}\,.$$

We can further simplify this relation if we assume that $l_f := \frac{EA}{\sigma} \gg 1\mu m$, which implies approximately straight segments and seems to be a good approximation for the experimental observations. In this limit, $R_i = \infty,\ \ \delta_i = 0,\ \ \gamma = 0,\ \ l_i = d_i$, and consequently

$$F_o \times \sin(\alpha) - \big((F_o + k(l - l_o)\big) \times \sin(\beta) = 0$$

$$F_o \times \cos(\alpha) + \big(F_o + k(l - l_o)\big) \times \cos(\beta) = F_o + k_2(l_2 - l_{2,o})$$

$$\cos(\beta) = \frac{l_o + l_{2,o} - l_2}{l}$$

$$0 \leq \beta \leq \frac{\pi}{2}$$

Note that here and before the elastic parts are only evaluated if $l - l_o > 0$, which represents the cable asymmetry between stretch and compression. We numerically solved this system of equations with the commercial software package *Mathematica* using F_o = 5 nN, $k = \frac{EA}{l_o}$, $k_2 = \frac{EA}{l_2}$, EA = 500nN, l_o= 26μm, $l_{2,o}$= 4μm, which are typical values for U2OS cells (17). Rather than exhibiting a simple force decay with increasing α, the force distribution shows a peak at α ≈ 70°, and the maximal force is considerably higher than the active forces involved (Fig. 4B). The force decreases for higher α until it reaches the active force level at α ~ 180°. The plateaus on the left and right end of the curve correspond to conditions in which either the outer (left) or central (right) cable is in the compression regime.

2) Interpretation of results:

This simple model shows that the exact magnitude of active forces might not be the only determinant for the retraction length. As the connecting SFs pull the contour inwards, an elastic stress occurs in the length-defined SF that might be higher than the active force of the connecting SF and is released when the length-defined fiber is severed. Experiments confirm that the contour not only retracts along itself after ablation but also moves inwards in this process. This indicates that there is indeed a stress caused by connecting SFs that pull inwards. This stress is primarily determined by the connection location of the connecting SF to the length-defined SF, and by the connection angle. We conclude that configurations with either only small or only large α are well suited to figure out the scale of active forces in experiments.

AI.3 Active Cable (ACN) simulations:

1) Description of workflow:

Unlike the symmetric model, cells exhibit asymmetric SF distributions. To determine whether the principles underlying the model may be extended to these more complex experimental networks, we conducted an additional set of simulations based on active cable networks (ACN). The advantages of ACN simulations are that they are very flexible regarding the geometry of the fiber distribution and they allow for the introduction of background network tension.

The workflow is illustrated in Fig. 4C-E and is as follows: We take the actin fluorescence image and enhance the contrast in ImageJ such that the SFs are clearly visible. We then use our plugin for the Segmentation of Focal Adhesions and STress fibers (SoFAST) (17) where the user can manually segment SFs by marking them with segmented lines. The plugin also allows us to segment cell area from the actin image and generate a triangular network that covers the whole cell area and embeds the stress fibers as marked edges. Due to the difficulty of segmenting a cell in such a way that a curved SF lies exactly at the cell rim, we implemented a mesh alteration routine which removes the network part on the outside of the peripheral SF. We then perform an optimization with respect to the ACN energy using the same active force and one-dimensional Young's modulus as for the symmetric model, F_o = 5 nN and EA = 500 nN for all SFs. As we segment already the invaginated contour of the cell, we set the rest length of the length-defined SF to 98% of its segmented length when comparing simulations and experiments. The background network was chosen to be softer by an order of magnitude and with a very small active component, which was added for numerical reasons. An example of a network after energy optimization with the software SurfaceMaster is shown in Fig. 4E, where the force magnitude is shown in color code. Fig.4E shows that the qualitative behavior of the symmetric model is broadly preserved in the ACN simulation. Although the individual connecting SFs add only 5 nN of active force, the total force in the fiber is as high as 25 nN at the center. The other segments show lower forces depending on the connectivity of the SFs. These force predictions enable comparison of model predictions to experiments. To perform this comparison, we investigated two data sets, where either n = 8 or n = 5 cells where cultured on U-shaped patterns with aspect ratio 1.9 and 3.0, respectively. Since we used the same parameters for all cell simulations within one data set (noted above), any differences observed in force magnitude at point of ablation is attributed only to the geometry of the internal SF network which was based on segmentations of the RFP-LifeAct images of individual cells. We then recorded the predicted force at the location of ablation in the corresponding experiment. We converted these forces to lengths L_f for comparison with the retraction length L_o using a simple spring model, $Fsimulation = k \times L_f$, where k = 3 nN/µm was chosen.

2) Interpretation of results:

The retraction lengths and the force lengths L_o and L_f match surprisingly well. Apart from one cell in each data set, the difference $\Delta L = abs\left(L_o - L_f\right)$is below 1 µm. Cells that show large retraction lengths show high forces at the point of ablation in the simulations, and, conversely, SFs with low retraction lengths are predicted to be under low force. We emphasize that information about the experimental retraction length did not enter the force prediction process, and that the parameter settings were the same for all simulations within each data set. This means that the active force was assumed to be the same for all SFs. This is obviously a very strong assumption and underlines the claim from the symmetric model that the connectivity determines peripheral SF forces more than force magnitudes. We conclude that ACN simulations are a fast and reliable way of estimating the force distribution along the contour.

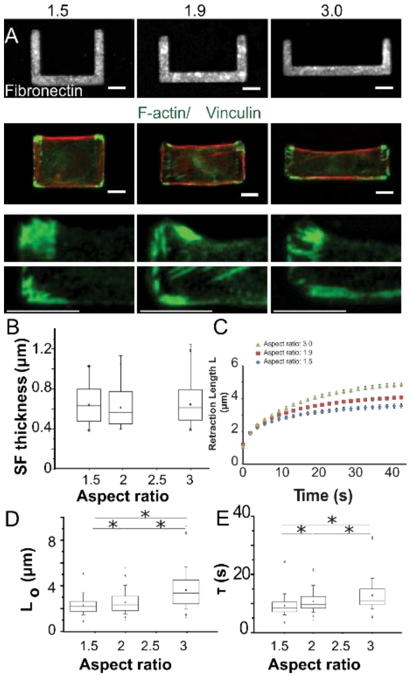

Figure S1: A, Distribution of matrix, actin, and focal adhesions on U-shaped patterns. Top row: Fibronectin staining of patterns of 3 aspect ratios (1.5, 1.9 and 3.0) and 3 SF lengths (30 μm, 38 μm and 50 μm). Second row: Distribution of SFs and focal adhesions in U2OS cells as visualized by F-actin (red) and vinculin (green). Third and fourth rows: Higher-magnification images show the absence of focal adhesions along the defined-length SF formed at the fibronectin-free side and the presence of adhesions along the pattern's bottom edge. **B**, SF thickness does not vary based on aspect ratio. **C,** Length-vs-time curves for retracting SFs on U-shaped patterns for varying aspect ratio. **D,** L_o increases with SF length as a function of aspect ratio. **E,** τ statistically increases with SF length (N = 84, 126 and 120 respectively). Statistical differences determined using Dunn test for multiple comparisons of non-normally distributed data (* = $p<0.01$). Boxes represent 25th and 75th percentiles; whiskers represent 10th and 90th percentiles. Scale bars = 10μm.

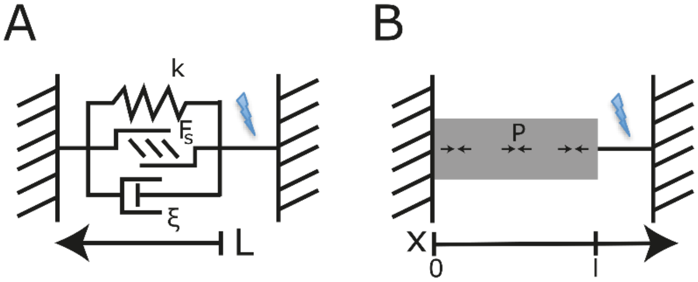

Figure S2: A, An active Kelvin-Voigt model consist of an elastic, a motor and a viscous element acting in parallel. L is the retraction length and it increases after laser cutting due to motor activity. **B,** A beam of length l contracts under the action of force dipoles P. The retraction length can be identified as $L = |u(l)|$, where $u(x)$ is the displacement field. The beam retracts if the connection to the wall is soft or if the connection is cut.

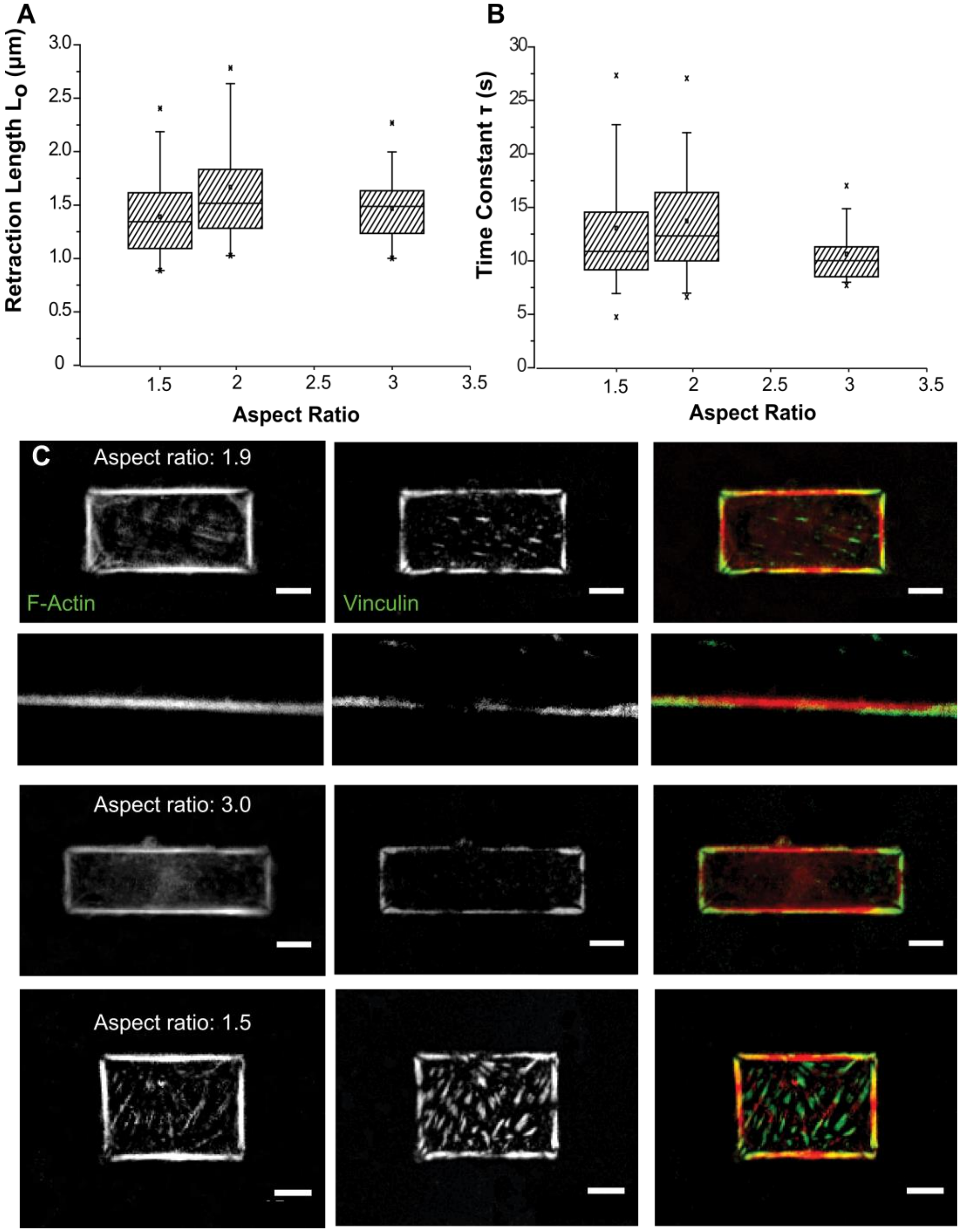

Figure S3: Viscoelastic properties of SFs of cells grown on fibronectin-coated rectangular patterns of variable-aspect ratio do not depend on SF length due to the presence of vinculin-positive focal adhesions. A, L_o obtained from the Kelvin Voigt fit does not vary with SF length as a function of aspect ratio. **B,** τ does not vary with SF length (N=22, 24 and 26 for each aspect ratio). Statistical differences were determined using Dunn test for multiple comparisons of non-normally distributed data. Boxes represent 25th and 75th percentiles; whiskers represent 10th and 90th percentiles. **C,** Distribution of SFs and focal adhesions of U2OS RFP-LifeAct cells seeded in varying-aspect ratio patterns as visualized by F-actin (RFP-LifeAct signal, red) and vinculin (immunofluorescence, green). Second row: Higher magnification images of cells seeded on patterns of aspect ratio 1.9 show the presence of focal adhesions along the length of the fiber. Scale bars = 10µm.

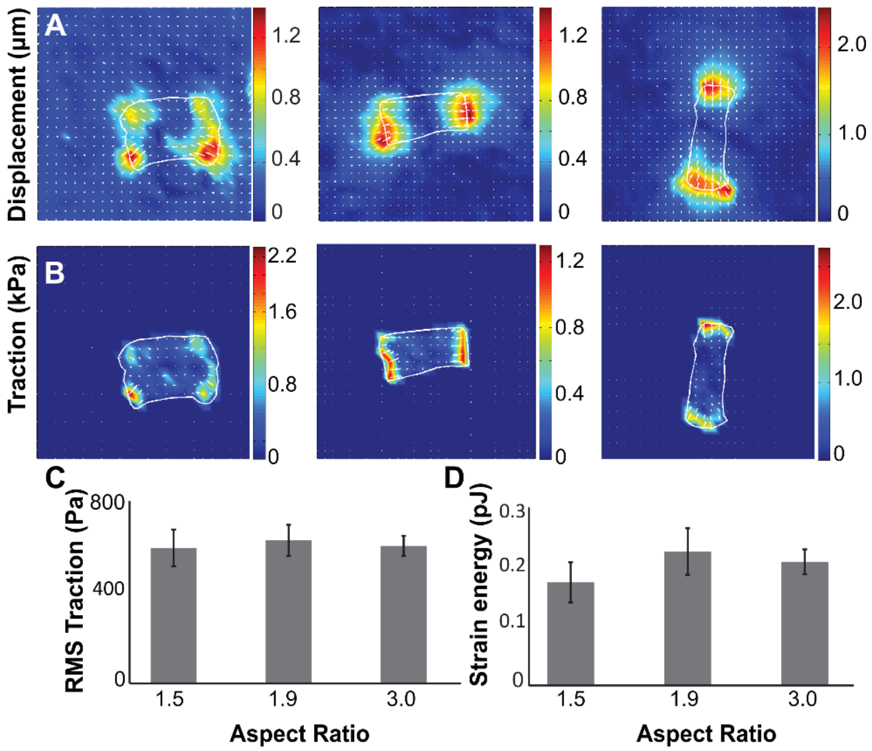

Figure S4: At the whole cell level, U2OS RFP-LifeAct cells produce similar traction and strain energy on all variable-aspect ratio patterns. A, Changes in bead displacement and ECM substrate strain distribution after removal of U2OS RFP-LifeAct cells seeded on Fibronectin-coated U-shaped patterns of varying-aspect ratio made on polyacrylamide gels (9.22kPa). **B,** Map of traction forces relaxed into the ECM substrate after cell removal. **C,** No statistical differences observed in average whole cell traction of cells seeded on U-shaped patterns on varying-aspect ratio. **D,** Average strain energy of U2OSRFP-LifeAct cells seeded on U-shaped patterns of varying-aspect ratio is not dependent on aspect ratio. Bars are mean ± SEM. Statistical differences were determined using ANOVA followed by Tukey (N= 8, 22 and 17 cells for each aspect ratio).

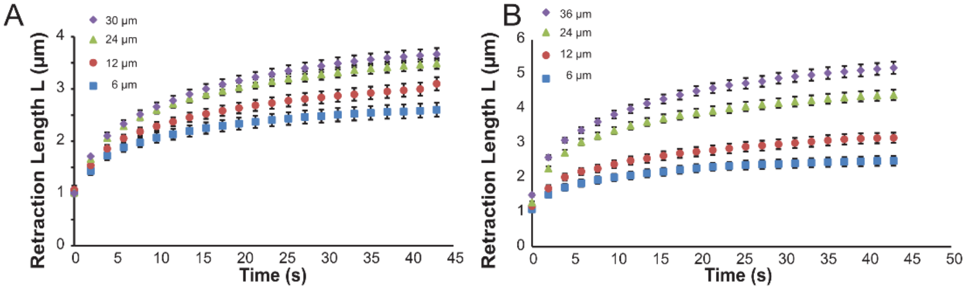

Figure S5: Length-vs-time curve for retracting SFs on (A) spacing patterns of aspect ratio 1.9 and (B) spacing patterns of aspect ratio 3.0.

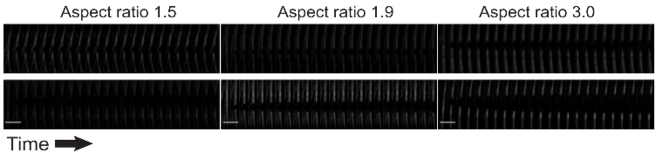

Figure S6: Despite micropatterning attempts, cells exhibit heterogeneity in retraction kinetics. Kymographs of SF ends of two cells retracting away from each other over time for each aspect ratio. Top panels show cells that undergo small retraction whereas bottom panels show cells that undergo large retractions. Each frame is 1.96 seconds. Scale bar is 10 µm.

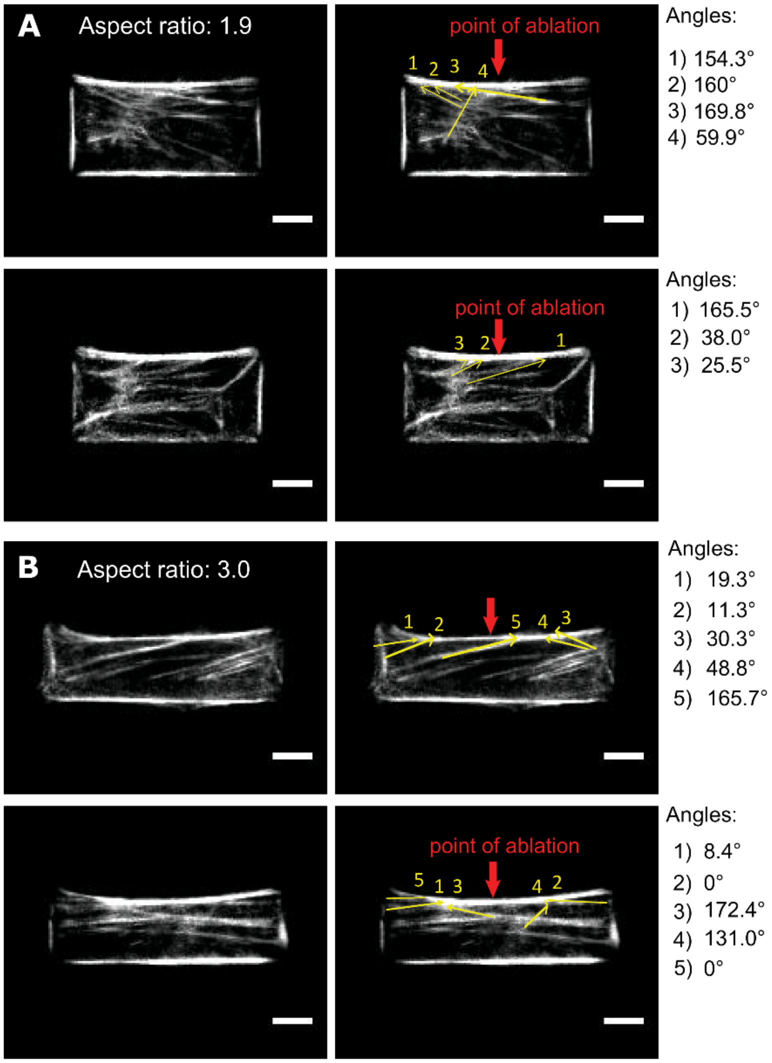

Figure S7: Examples of angle analysis and stress fiber segmentation. Firstly, the image orientation is adjusted in order for the cell horizontal axis to be at zero degrees. Secondly, the intensity of RFP-LifeAct images of U2OS cells before ablation was adjusted using ImageJ. Connecting SFs were then visualized by RFP-LifeAct and manually traced. The angle between the connecting fiber and the horizontal axis is measured and recorded in degrees in ImageJ. Angle is recorded as discussed in the model presented in Fig. 2E. We then calculate the cosine of each angle and finally add up all the values to determine the Sum of cos (α) per cell.

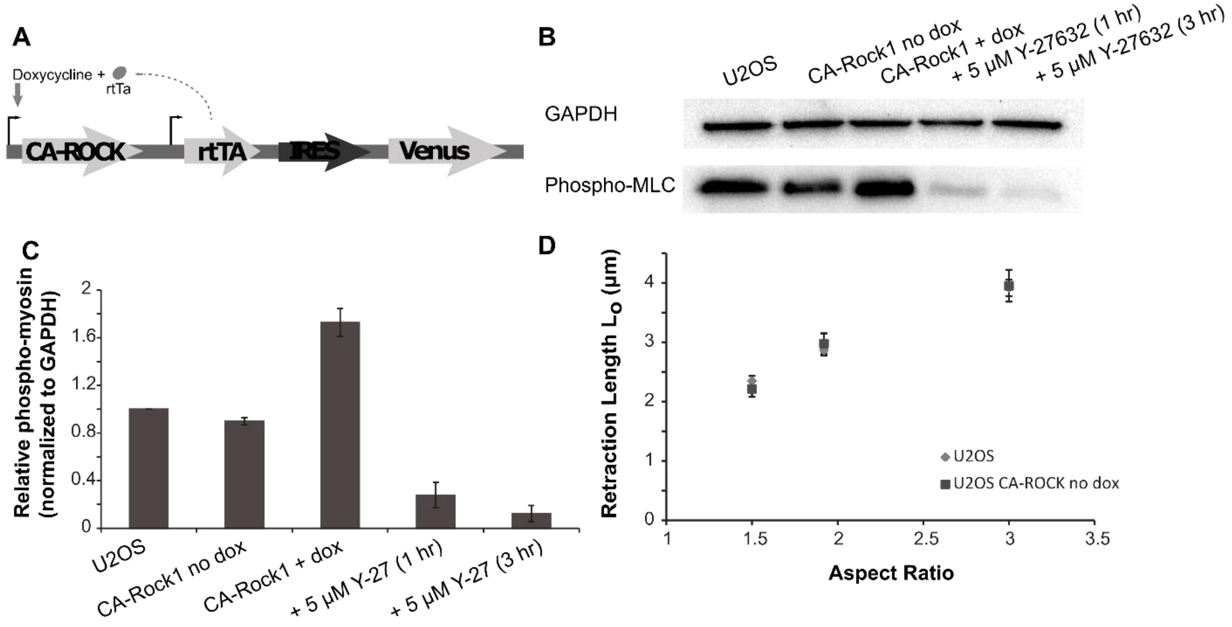

Figure S8: Characterization of pSLIK CA-ROCK cells and 5μM Y-27632 treated cells. A, Schematic of the pSLIK system used for expression of CA-ROCK. Briefly, a constitutively active form of ROCK is placed under the control of a doxycycline-inducible promoter. The construct is then placed in a lentiviral vector which is used to transduce cells and form stable cell lines. **B,** Westerns were carried out to verify the effectiveness of the construct and Y-27632 incubation. In the absence of doxycyline (lane 2), the construct remains silent with no observable change in myosin light chain phosphorylation compared to naive cells. In the presence of doxycycline (lane 3), CA-ROCK is activated leading to increases in myosin light chain phosphorylation. For Y-27632 treated cells, we observe a decrease in myosin light chain phosphorylation after 1 hour of incubation. **C,** Quantification of western blot bands normalized to GAPDH and to the expression of phosphorylated myosin light chain of naive cells. (N=4 blots, Bars represent means ± SEM). **D,** L_o of U2OS RFP-LifeAct cells and U2OS RFP-LifeAct CA-ROCK cells with no doxycycline are statistically similar showing that the transduction did not affect SF viscoelastic properties (Student's t-test comparing conditions at each aspect ratio, for CA-Rock – no doxycycline cells, N = 23, 26 and 26 for each aspect ratio, for U2OS RFP-LifeAct cells, N = 78, 127 and 116 for each aspect ratio respectively). Error bars are SEM.

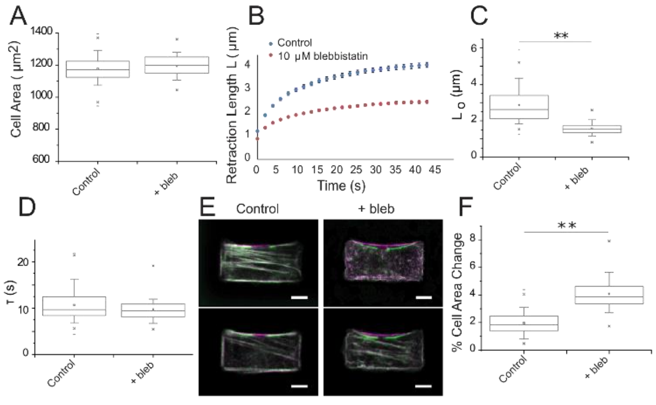

Figure S9: Blebbistatin treated cells undergo smaller retraction but greater inward movement. A, Quantification of cellular area of cells seeded on U-shaped patterns of aspect ratio 1.9 in the absence and presence of 10 μM blebbistatin (N = 106 and 61 respectively). **B,** Length vs. time curves for retracting SFs in cells seeded on U shaped patterns in the presence and absence of blebbistatin (N = 54 and 126 for each condition). Both follow an exponential retraction. **C,** L_o decreases in the presence of blebbistatin. **D**, τ is unchanged with treatment of blebbistatin. **E,** Overlay of U2OS RFP-LifeAct cells before (magenta) and after (green) ablation. Length-defined SFs of blebbistatin-treated cells undergo a larger inward movement indicated by the arrow. **F,** Quantification of percentage area change after ablation for each population shows that there is a statistically larger change in area in blebbistatin-treated cells due to a larger inward movement. Statistical differences determined using a Student's t-test (** = p<0.0001). Boxes represent 25th and 75th percentiles; whiskers represent 10th and 90th percentiles (N= 61 for and 106 respectively). Data for control cells transposed from Figure S1. Scale bars = 10μm.

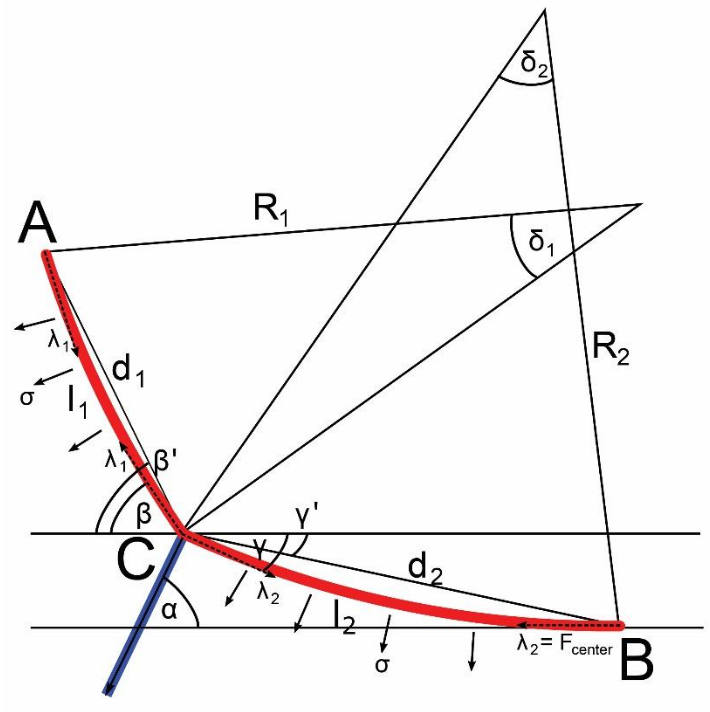

Figure S10: Schematics of the symmetric tension-elasticity model extended with a connecting fiber. The figure shows the left half of the symmetrical situation described in Fig. 4A in more detail. The connecting SF (blue) separates the length-defined SF (red) in two segments, which we label by indices 1 (segment A-C) and 2 (segment C-B), respectively. Each segment forms a circular arc of radius $R_i = {}^{\lambda_i}/_{\sigma}$, where λ_i is the tension along the segment and σ is a homogeneous surface tension. Note that F_{center} pulls in the horizontal direction for symmetry reasons. The geometric relations and derived model equations are explained in the supplementary text.

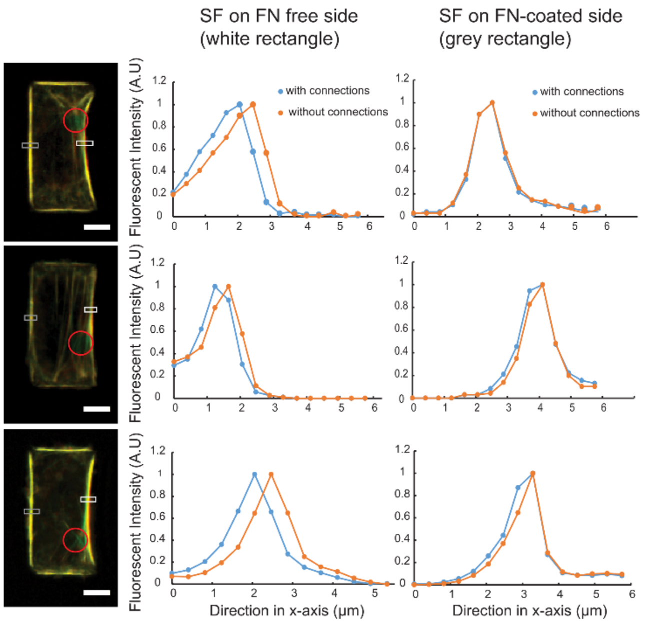

Figure S11: Removal of connections causes length-defined SF to shift away from the cell body showing that the SF is under prestress from the connecting network. Left column: Overlay of RFP-LifeAct images of cells before (green) and after (red) ablation of connecting fibers. Ablation point highlighted by red circle. Scale bar = 10 µm. Middle column: Normalized fluorescent intensity plot of length defined SF over highlighted white box. Blue curve shows fluorescent intensity before ablation and orange curve shows fluorescent intensity after ablation and with the removal of connections. All curves shift to more positive values suggesting that the SF moves to the right (away from the cell body). Right column: Normalized fluorescent intensity plot of length defined SF over highlighted grey box. Blue curve shows fluorescent intensity before ablation and orange curve shows fluorescent intensity after ablation and with the removal of connections. No visible shift observed suggesting that the shift shown in middle column is indeed due to the removal of connections.

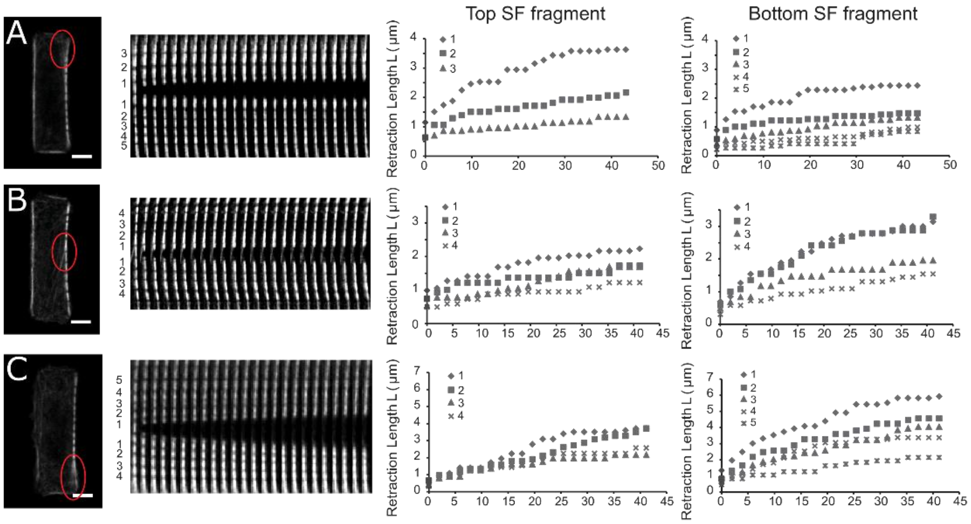

Figure S12: Retraction within an SF is heterogeneous and correlates with the geometry of the internal SF network. U2OS RFP-LifeAct cells exhibiting asymmetric connections (**A** – top SF fragment highly connected with acute angles, **B** – top SF fragment connected at angles >90°, **C** – bottom SF fragment highly connected with acute angles) were photobleached to create rectangular segments within the length-defined SF. The SF was then ablated and retraction of each segment was traced (third and fourth column). In A and C, segments within the SF fragment that is highly connected undergo greater retraction than segments in the non-connected SF fragment. In B, segments in the SF fragment that is connected to the internal SF at an angle >90° undergo smaller retraction due to an opposing force that impedes recoil.

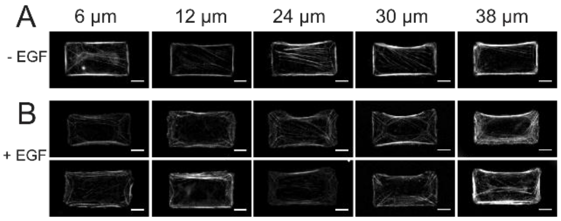

Figure S13: Treatment with EGF leads to a formation of a lamella-like structure whose orientation depends on the spacing of the pattern. A, Actin distributions (phalloidin stains) within U2OS cells seeded on spacing patterns of aspect ratio 1.9. On all patterns, cells form four peripheral stress fibers across the boundaries of the pattern. **B,** Actin distributions within U2OS cells seeded on spacing patterns and treated with EGF for 4 hours. EGF induces a motile phenotype where the peripheral SFs at the pattern boundaries dissociate to form dorsal SFs and transverse arcs. When the spacing is small (6 μm and 12 μm), the SF formed across the gap may also dissociate and migratory-like structures can form at either the top or the bottom part of the pattern. As the spacing increases, the SF formed across the gap remains and becomes the "rear" of the cell. For all images, the spacing is at the top and scale bar = 10 μm.

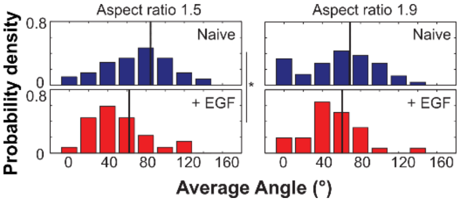

Figure S14: Treatment with EGF leads to a shift in the average angle distribution to smaller (more acute) angles for both aspect ratios 1.5 and 1.9.

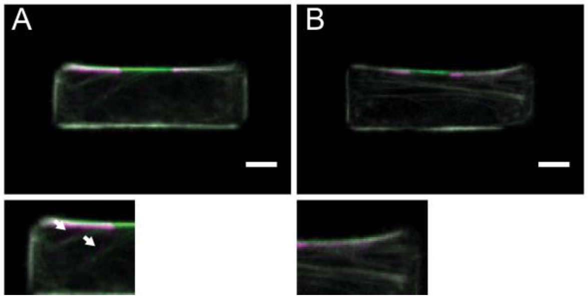

Figure. S15: Overlay of cells before (green) and after (magenta) ablation to show that connecting fibers move along with the cut fiber (A – observed green and purple stress fibers in overlay as shown by the white arrows). The time constant τ for the cell shown in A is 10.93 seconds whereas for the cell shown in B, τ is 8.19 seconds.

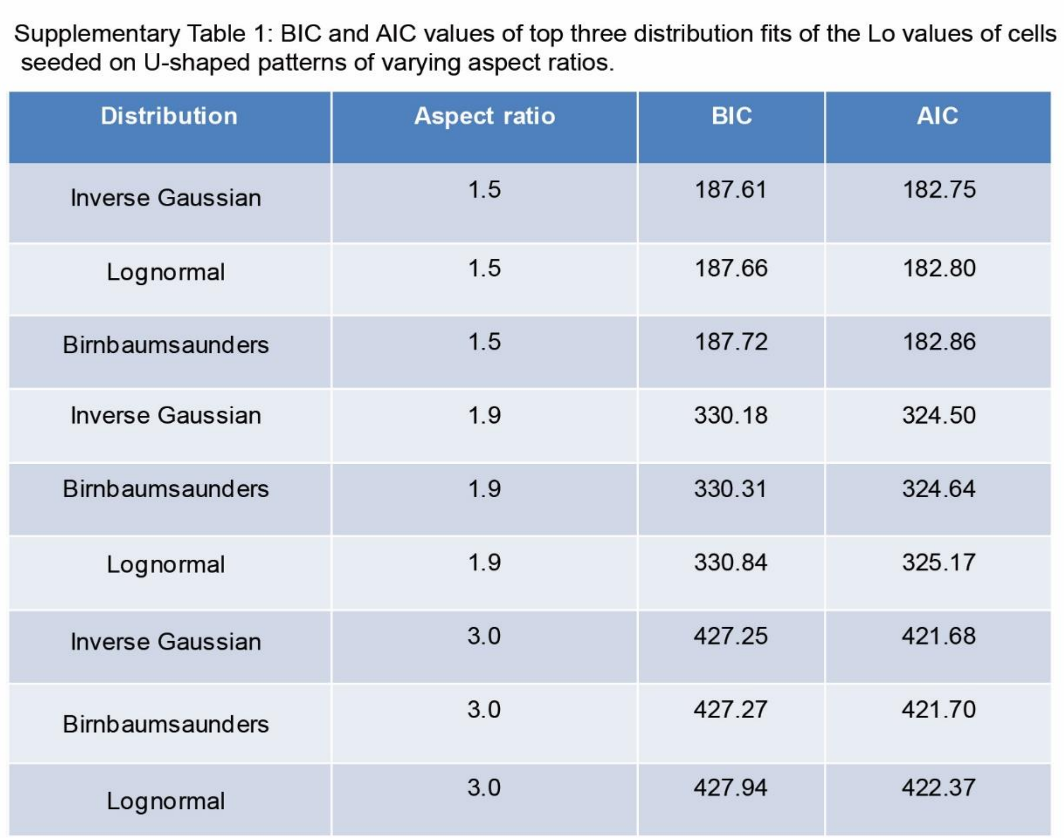

Supplementary Table 1: BIC and AIC values of top three distribution fits of the Lo values of cells seeded on U-shaped patterns of varying aspect ratios.

Distribution	Aspect ratio	BIC	AIC
Inverse Gaussian	1.5	187.61	182.75
Lognormal	1.5	187.66	182.80
Birnbaumsaunders	1.5	187.72	182.86
Inverse Gaussian	1.9	330.18	324.50
Birnbaumsaunders	1.9	330.31	324.64
Lognormal	1.9	330.84	325.17
Inverse Gaussian	3.0	427.25	421.68
Birnbaumsaunders	3.0	427.27	421.70
Lognormal	3.0	427.94	422.37

Table S1: Bayesian Information criterion (BIC) and Akaike Information criterion (AIC) values of the top three distribution fits of the L_o distributions of cells seeded on U-shaped patterns of varying-aspect ratio. Fits were calculated based on histograms shown in Fig. 3a using the *allfitdist* command in Matlab. The command returns all possible distributions that fit the data (normal and non-normal) including the distribution parameters and the respective BIC and AIC values. In this table, we list the top three distribution fits for each aspect ratio (Distribution fits are also drawn in Fig. 2A). All fits provided have an average peak and a long tail showing the highly heterogeneous nature of the L_o collected.

References

1. Kassianidou E, Kumar S (2015) A biomechanical perspective on stress fiber structure and function. *Biochim Biophys Acta - Mol Cell Res* 1853(11, Part B):3065–3074.

2. Burnette DT, et al. (2014) A contractile and counterbalancing adhesion system controls the 3D shape of crawling cells. *J Cell Biol* 205(1):83–96.

3. Blanchoin L, Boujemaa-Paterski R, Sykes C, Plastino J (2014) Actin dynamics, architecture, and

mechanics in cell motility. *Physiol Rev* 94(1):235–263.

4. Murrell M, Oakes PW, Lenz M, Gardel ML (2015) Forcing cells into shape: the mechanics of actomyosin contractility. *Nat Rev Mol Cell Biol* 16(8):486–498.

5. Stachowiak MR, O'Shaughnessy B (2009) Recoil after severing reveals stress fiber contraction mechanisms. *Biophys J* 97(2):462–71.

6. Labouesse C, Gabella C, Meister J-J, Vianay B, Verkhovsky AB (2016) Microsurgery-aided in-situ force probing reveals extensibility and viscoelastic properties of individual stress fibers. *Sci Rep* 6:23722.

7. Schwarz AB and US (2007) Coupling biochemistry and mechanics in cell adhesion: a model for inhomogeneous stress fiber contraction. *New J Phys* 9(11):425.

8. O'Shaughnessy MRS and Ben (2008) Kinetics of stress fibers. *New J Phys* 10(2):25002.

9. Besser A, Colombelli J, Stelzer EHK, Schwarz US (2011) Viscoelastic response of contractile filament bundles. *Phys Rev E* 83(5):51902.

10. Mayer M, Depken M, Bois JS, Julicher F, Grill SW (2010) Anisotropies in cortical tension reveal the physical basis of polarizing cortical flows. *Nature* 467(7315):617–621.

11. Kumar S, et al. (2006) Viscoelastic retraction of single living stress fibers and its impact on cell shape, cytoskeletal organization, and extracellular matrix mechanics. *Biophys J* 90(10):3762–73.

12. Bischofs IB, Schmidt SS, Schwarz US (2009) Effect of Adhesion Geometry and Rigidity on Cellular Force Distributions. *Phys Rev Lett* 103(4):48101.

13. Bischofs IB, Klein F, Lehnert D, Bastmeyer M, Schwarz US (2008) Filamentous network mechanics and active contractility determine cell and tissue shape. *Biophys J* 95(7):3488–96.

14. Labouesse C, Verkhovsky AB, Meister J-J, Gabella C, Vianay B (2015) Cell Shape Dynamics Reveal Balance of Elasticity and Contractility in Peripheral Arcs. *Biophys J* 108(10):2437–2447.

15. Russell RJ, Xia S-L, Dickinson RB, Lele TP (2009) Sarcomere mechanics in capillary endothelial cells. *Biophys J* 97(6):1578–1585.

16. Colombelli J, et al. (2009) Mechanosensing in actin stress fibers revealed by a close correlation between force and protein localization. *J Cell Sci* 122(11):1928–1928.

17. Soiné JRD, et al. (2014) Model-based traction force microscopy reveals diferential tension in cellular actin bundles. *PLoS Comput Biol*.

Chapter 3. Cell spreading dictates stress fiber geometry

3.1 Abstract

Cells exhibit heterogeneous stress fiber (SF) architectures, with wide cell-to-cell variations in SF number and connectivity. The degree of connectivity strongly influences the elastic energy dissipated by peripheral SFs of patterned cells as shown in Chapter 2, which begs the question of how the SF connectivity within an individual cell arises and is maintained. To explore this issue, we combined single cell micropatterning with time-lapse imaging of cell binding and spreading to track the dynamics of SF network assembly during spreading. We show that initial cellular binding position on the micropattern as well as spreading history can affect the final internal SF configuration. Furthermore, we show that the extracellular matrix geometry can alter the spreading history (irrespective of initial binding position) and thereby contribute to final internal SF configuration. Finally, we show that after SF disassembly, cells return to similar SF configurations, suggesting that cells maintain a memory of the SF network encoded or maintained by other cytoskeletal and adhesive structures. Our preliminary results support the idea that cells have structural memory and motivate further experimental and computational analysis.

3.2 Introduction

The stress fiber (SF) network is responsible for force generation and transmission across a cell-extracellular matrix (ECM) interface as well as cell-cell adhesions (1–3). The force generated by the SF network is important in cellular adhesion, maintenance of cell shape, migration and proliferation and in the case of stem cells, it can direct stem cell differentiation lineage (4, 5). The SF network, however, is highly heterogeneous from cell to cell. It can vary in the number of SFs present, their location across the cell as well as their overall interconnectivity. It is currently unclear whether and how these heterogeneities contribute to cellular functions such as spreading, adhesion and migration.

Moreover, as discussed in Chapter 2, heterogeneities of the internal SF architecture led to differences in the elastic energy dissipated by peripheral SFs after subcellular laser ablation (SLA) (6). This suggests that different SF architectures distribute and maintain tension across a cell in unique ways. Furthermore, we developed a simple active cable model that takes as an input the architecture of the connecting SFs to the peripheral fiber of interest and can remarkably predict the retraction kinetics of the peripheral SF (6). These results illustrate the importance of the internal SF network architecture in understanding and appreciating single SF mechanics and their role to overall cellular tension distribution (7, 8).

The architecture and composition of the SF network is very dynamic and can change depending on the state of the cell – for example a migratory/spreading cell has a different SF architecture and composition than a stationary cell, with increased number of transverse arcs and dorsal SFs found in the lamella than a non-motile cell that lacks polarization (9–11). As such, it is challenging to understand how SF network heterogeneities arise due to the inherent heterogeneity present in cell culture.

Understanding how the heterogeneities in SF architectures arise may provide further insight into how an individual cell interacts with the extracellular adhesive environment and how it processes signals such as ECM geometry to spread and decide on a final SF configuration. In this chapter, we therefore sought to understand how ECM geometry and cell spreading contribute to the final SF configuration of a cell. To standardize cell and SF geometry, we wish to observe the SF architectures of cells while spreading on patterns of fixed geometry as well as their final SF configuration when the cell spreads fully.

3.3 Results

To gain an appreciation of the degree of heterogeneity in the geometry of internal SFs in U2OS RFP-LifeAct cells, we designed two sets of rectangular patterns with a 15 µm spacing placed at the top or side while keeping the fibronectin (FN) area, pattern area and aspect ratio constant (Fig. 1A) (6, 12). As shown in Fig. 1B-C, U2OS cells conform to the pattern shape and form thick peripheral SFs across the perimeter of the pattern as well as a peripheral SF that spans over the top or side gap. Cells also form vinculin-positive focal adhesions (FAs) only where the FN pattern is present and no such adhesions are visible across the gap or in the internal area of the rectangle. Internal SF architecture, however, is highly heterogeneous both in the numbers of SFs formed as well as in their angular distribution. Additionally, the distribution and size of FAs varied from cell to cell on either the top or side pattern. We reasoned that identifying the sources of internal SF architecture heterogeneity may potentially yield valuable and unappreciated regulatory principles underlying SF formation, development over time within the cell as well as provide insight as to whether cells have an intrinsic memory that allows them to form reproducible cytoskeletal structures as seen in tissue.

We hypothesized that internal SF architecture may be related to the spreading history of the cell, and as such, the initial binding position of the cell on the pattern may be predictive of the final internal SF configuration. To determine the veracity of this hypothesis, we followed the SF architecture of a cell while it was spreading over time on either top-spacing (Fig. 2A) or side-spacing (Fig. 2B) patterns. First, we observed that on the top spacing patterns, cells bound either at the two corners or at the bottom long FN line (Fig. 2A, top and bottom rows). Cells that bound at the corners exhibited thick diagonal SFs that were parallel to the direction of spreading and persisted throughout the spreading process (Fig. 2A, top rows). When the cells bound at the bottom FN line, they spread parallel to the long axis of the pattern. In some cases, both lamella-like structures found on the perpendicular FN lines migrated at the same rate leading to strong horizontal SFs that persist throughout the spreading. It is also possible however that one “lamella like structure” overtakes the other leading to a triangular cell shape and SFs formed are at an angle rather than horizontal. Our results that SFs are formed parallel to the lamella-like structures agree with previously published work (13–15). Secondly, cells seeded on the side-spacing pattern bound at the corner of the pattern or at the top/bottom FN line of the pattern (Fig. 2B, top

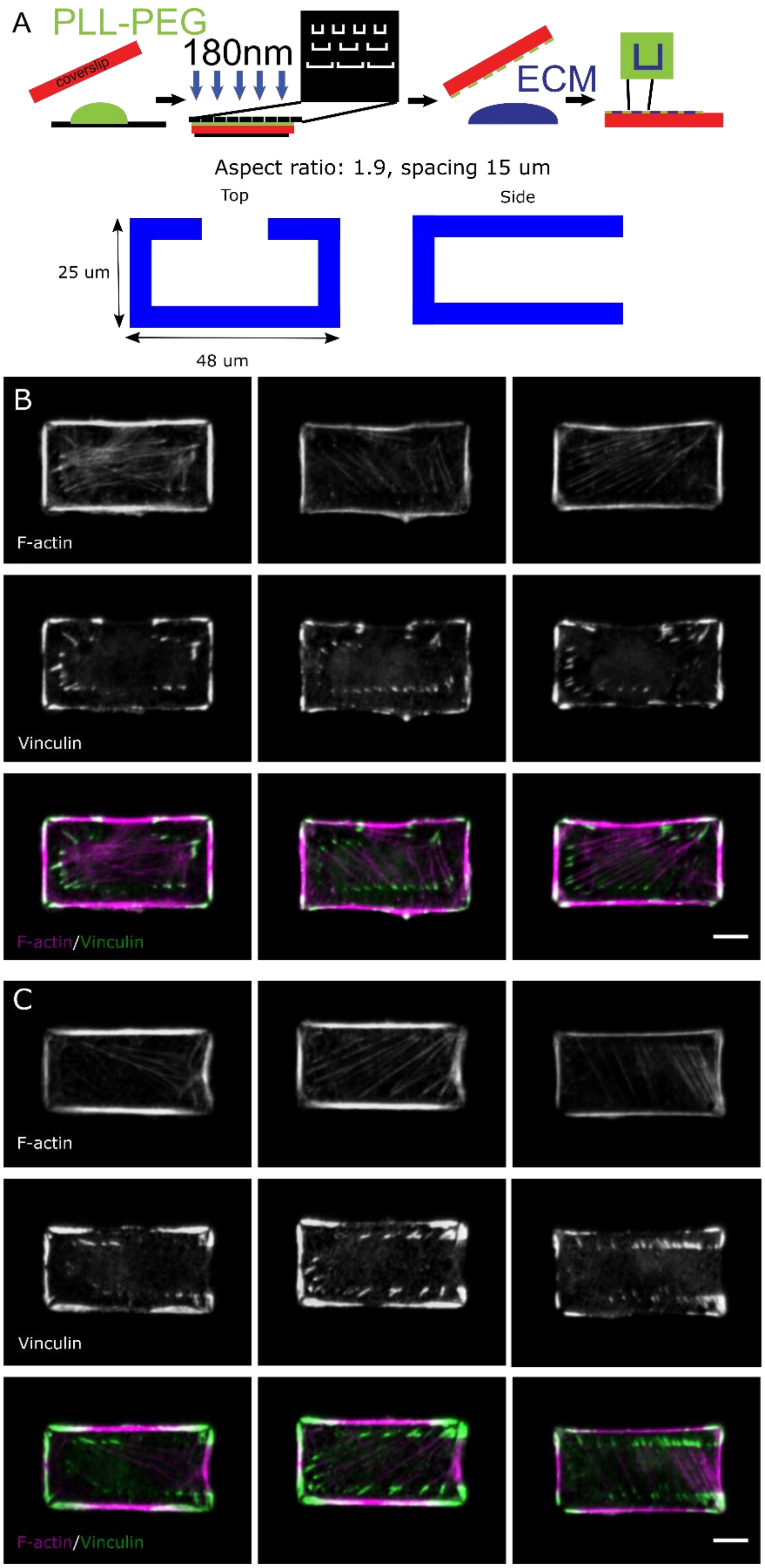

Figure 1: Heterogeneity of internal SF architecture on patterned U2OS cells. (A) Schematic of pattern fabrication that results in two rectangular patterns of same aspect ratio and FN area but different gap spacing. (B) Distribution of F-actin (magenta) and vinculin positive focal adhesions (green) of cells seeded on the top-spacing patterns. (C) Distribution of F-actin (magenta) and vinculin (green) of U2OS cells seeded on the side-spacing patterns. Scale bars = 10 µm.

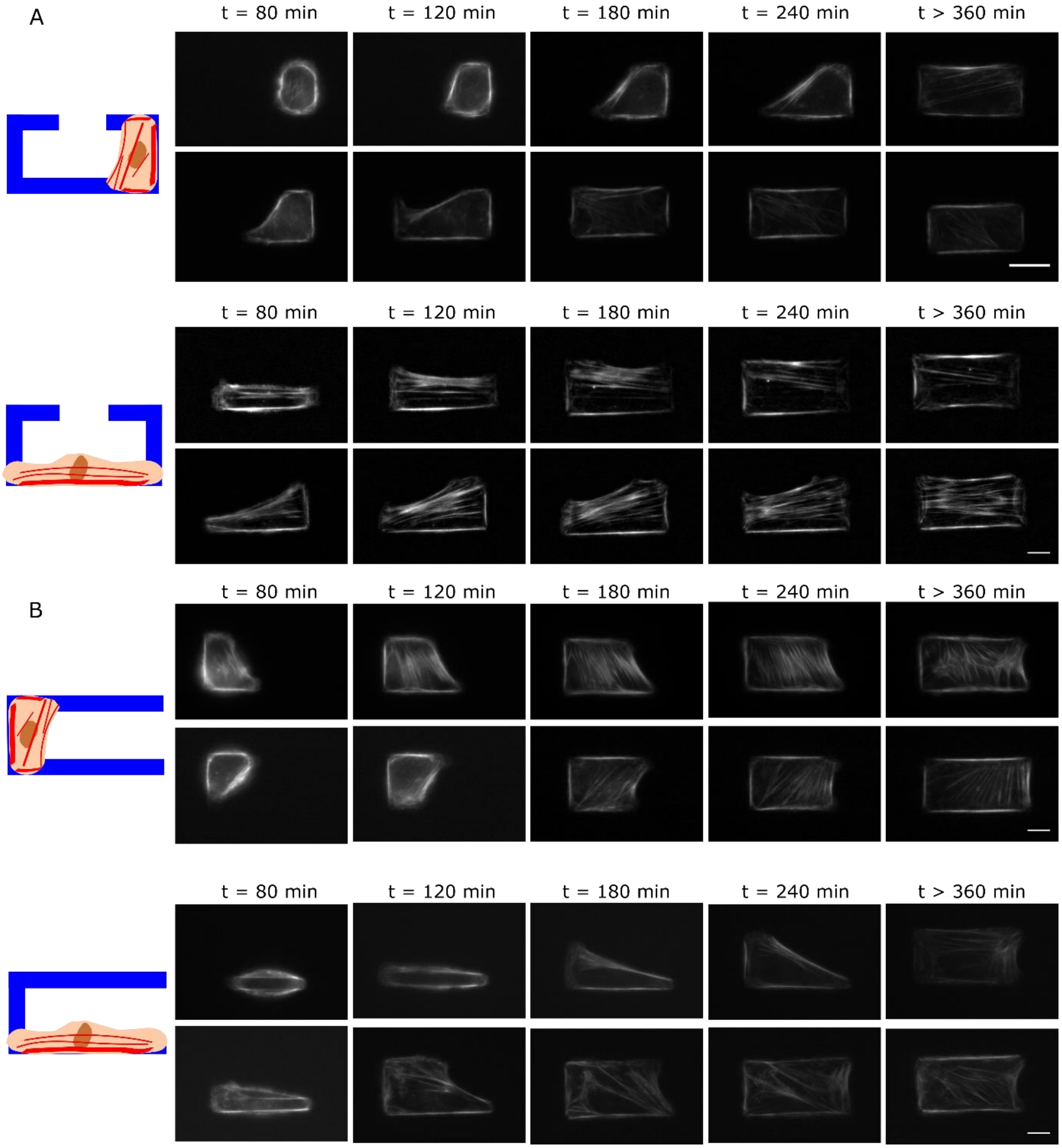

Figure 2: Time-lapse images of cells spreading on patterns from different initial binding positions. U2OS RFP-LifeAct cells seeded on (A) top-spacing patterns initially bound at either the corners (top rows) or bottom FN-line (bottom rows) or on (B) side-spacing patterns initially bound at either the corner (top rows) or bottom FN-line (bottom rows) exhibit different internal SF architectures as detected by RFP-LifeAct images taken over a period of 8 hours. Scale bars = 10 µm.

and bottom rows). Cells that bound at the corners exhibited thick perpendicular SFs that persisted throughout the spreading process. If one of the lamella like structrues overtakes the other leading edge then the SFs shift in angle. Finally, cells bound on the long FN line of the pattern go through a triangular phase where they form SFs parallel to the cell's edge and seem to persist throughout the spreading process. Based on these qualitative findings, binding position and spreading of a cell on a pattern seem to be predictive factors of internal SF configuration.

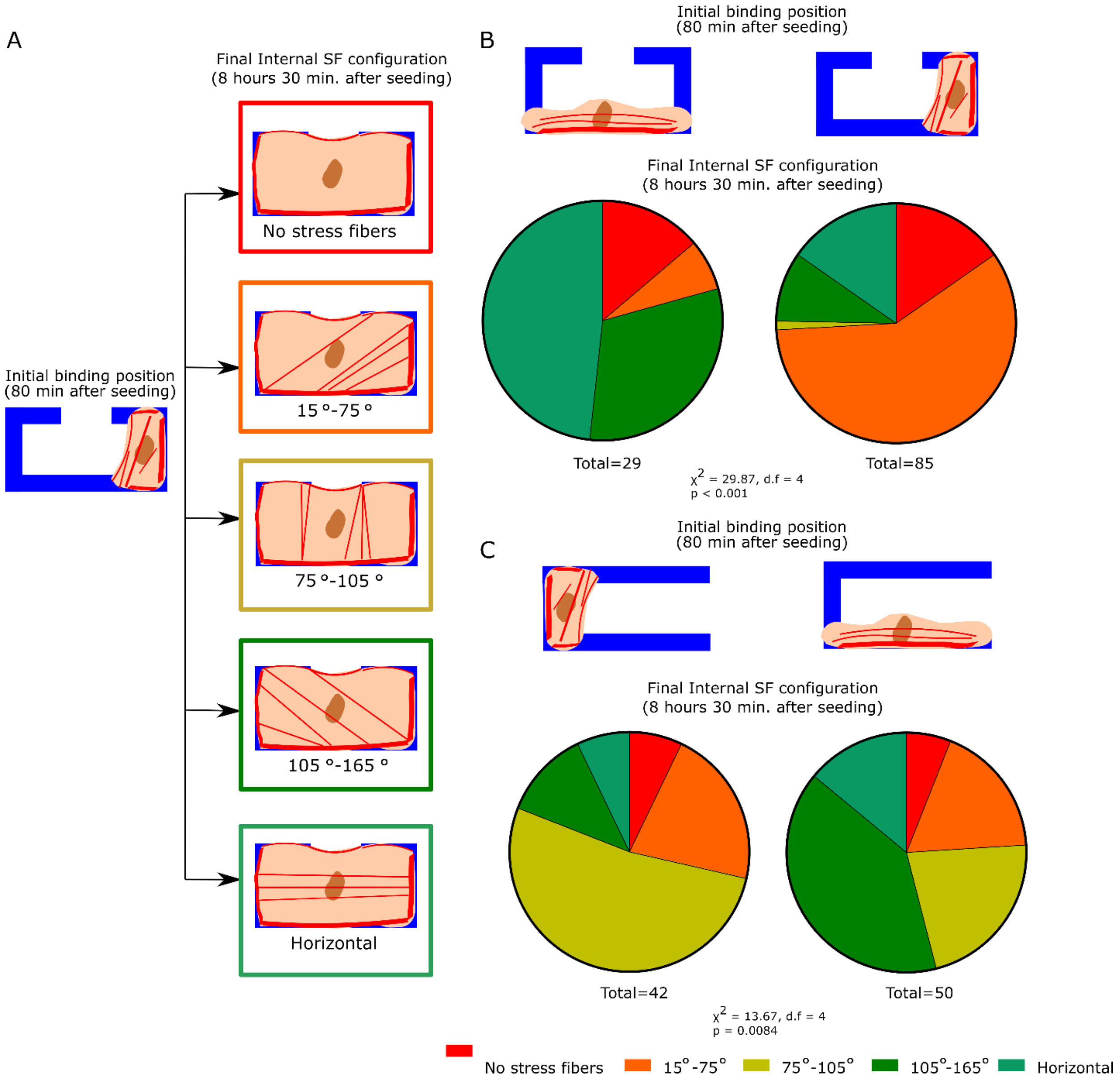

Figure 3: Correlating initial binding position of cell on the micropattern to its final internal SF configuration. (A) Schematic of analysis. U2OS RFP-LifeAct cells were seeded on the patterns and 1 hour 20 minutes after seeding, the initial binding position of the cell was recorded. Images were taken every 10 minutes looking at F-actin (RFP-LifeAct) for at least 8 hours and 30 minutes after seeding. Cells are then subdivided into 5 categories based on their final internal SF configuration: no internal SFs visible, majority of SFs are angled between 15°-75°, 75°-105°, 105°-165° or most SFs are horizontal and span the long axis of the cell. (B) Comparison of initial binding position of cells seeded on the top-spacing pattern to final internal SF configuration. There are two possible initial binding positions – on the long FN line (left) or on either of the two corners (right). Relative abundances of final internal SF configurations based on initial binding positions are statistically different based on a χ^2 test (N = 29 cells bound on the long FN binding position and 85 cells bound at either of the corners). (C) Comparison of initial binding position of cells seeded on the side-spacing pattern to final internal SF configuration. There are two possible initial binding positions – on the left corner of the pattern (left) or on either of the long FN lines (right). Relative abundances of final internal SF configurations based on initial binding positions are statistically different based on a χ^2 test (N = 42 cells bound at the corner and 49 cells bound at either the top or bottom long FN line).

To study this in a more quantitative manner, we designed the following experimental and analytical workflow. First, we allowed the cells to bind on either top-spacing or side-spacing patterns and followed the cells spreading over a period of 8 hours and 30 minutes. We then correlated the initial binding position of each cell based on the first image of RFP-LifeAct taken at 80 minutes after cell seeding and the final internal SF configuration based on the last image of RFP-LifeAct taken at 8 hours 30 minutes (Fig. 3A). Final internal SF configurations were determined based on the angle of the majority of the SFs and cells were classified in the following categories: 1) no visible SFs, 2) major angle of 15°-75°, 3) major angle of 75°-105°, 4) major angle of 105°-165° and, 5) horizontal SFs (Fig. 3A). We hypothesized that cells bound on the left corner of the top-spacing pattern should exhibit symmetrical distributions to cells bound on the right corner. The relative frequencies of internal SF distributions of left versus right corner binding are indeed symmetric – 59.4% of cells bound on the right corner exhibited angles between 15°-75° whereas 58.3% of cells bound on the left corner exhibited angles between 105°-165° (Appendix II – Fig. S1). Additionally, we assumed that cells bound at the top and bottom long FN line of the side-spacing pattern should also behave in a symmetric manner – 65.4% of cells bound on the bottom FN line exhibited angles between 75°-165° whereas 58.3% of cells bound on the top FN line exhibited angles between 15°-105° (Appendix II – Fig. S1). Due to the symmetry exhibited between these binding conditions (left and right corner on top-spacing patterns, top and bottom on side-spacing patterns), we combined them into one binding condition referred to as corner binding for the top-spacing pattern and long-edge binding for the side-spacing pattern.

A statistical difference was observed between the relative frequencies of final internal SF configurations based on the initial binding position of cells on the top-spacing pattern (Fig. 3B) as well as on the side-spacing pattern (Fig. 3C). These results show that indeed binding position can be a predictor of the final internal SF configuration.

Furthermore, we wondered whether the ECM geometry may also affect the spreading history of the cell and therefore the final internal SF configuration. We specifically asked whether moving the spacing from top to the side altered the final internal SF configurations of cells that initially bound at the same position. To answer this question, we compared the relative distributions of final internal SF configurations of cells bound at the bottom edge of top-spacing pattern and the bottom edge of the side-spacing pattern (Fig. 4A) and the relative distributions of final internal SF configurations of cells bound at the left corner of top-spacing patterns and the corner of the side-spacing pattern (Fig. 4B). Both comparisons were significantly different showing that in addition to the binding position, the geometry of the ECM also alters the internal SF configuration of cells and may be used as a predictive marker.

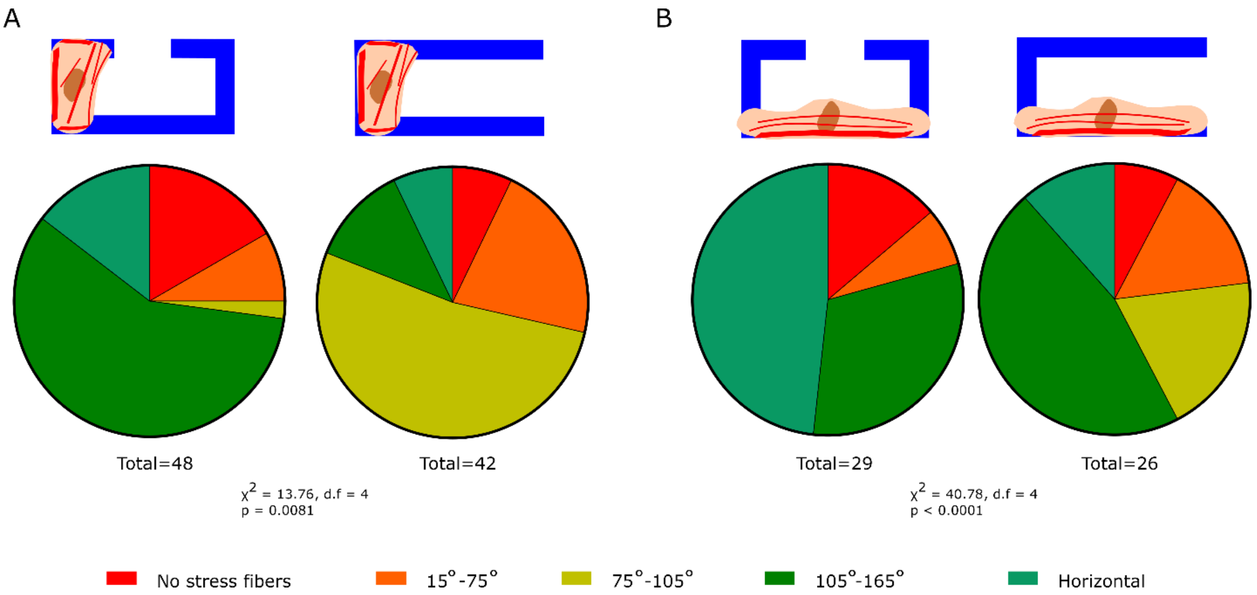

Figure 4: ECM geometry also dictates final internal SF distribution irrespective of initial binding position. (A) Comparison of initial binding position of cells seeded on the top-spacing pattern to final internal SF configuration. There are two possible initial binding positions – on the long FN line (left) or on either of the two corners (right). Relative abundances of final internal SF configurations based on initial binding positions are statistically different based on a χ^2 test (N = 29 cells bound on the long FN binding position and 85 cells bound at either of the corners). (C) Comparison of initial binding position of cells seeded on the side-spacing pattern to final internal SF configuration. There are two possible initial binding positions – on the left corner of the pattern (left) or on either of the long FN lines (right). Relative abundances of final internal SF configurations based on initial binding positions are statistically different based on a χ^2 test (N = 42 cells bound at the corner and 49 cells bound at either the top or bottom long FN line).

Finally, we wondered whether a cell maintains a memory of its SF architecture after spreading fully over the pattern. To answer this, we allowed the cells to spread on the patterns and then disassembled the SF network using 1 µM of Cytochalasin-D, a potent inhibitor of actin depolymerization, for 30 minutes. Cytochalasin-D was then washed off and the cells were allowed to reform SFs (Fig. 5A). As shown in Fig. 5B, Cytochalasin-D inhibition was successful at breaking down the SF network (second row). In some instances, cells balled up and detached from parts of the pattern. Those cells were discarded during the analysis since after Cytochalasin-D was removed, a new spreading process was initiated that skewed our results. As shown in the third row of Fig. 5B, cells recover their SF network within 2 hours 30 minutes following Cytochalasin-D removal. We quantified the relative distribution of the initial and final internal SF configurations based on the categorization described previously. The two distributions show no statistical differences. We observed similar results with cells seeded on the side-spacing patterns (Appendix II – Fig. S2). These results suggest that cells possess an intrinsic memory that allows them to form reproducible internal SF architectures even after SF depolymerization.

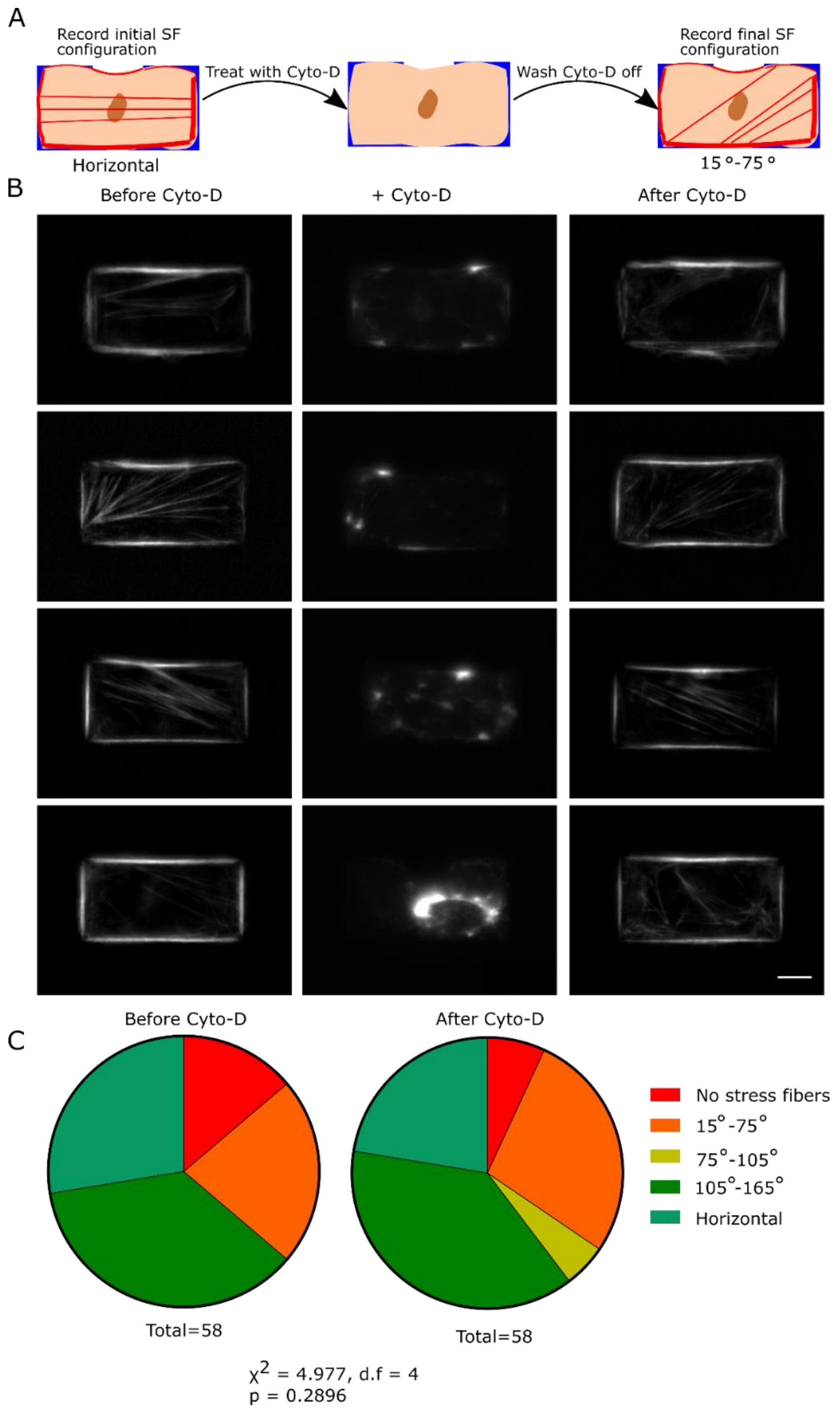

Figure 5: Cells seeded on the top-spacing pattern maintain a memory of the SF distribution after SF depolymerization using Cytochalasin-D (A) Schematic of experimental set-up. U2OS RFP-LifeAct cells spread on the top-spacing patters for 6 hours and images of the internal SF architecture were obtained and cells were sub-divided into 5 categories: no internal SFs visible, majority of SFs are angled between 15°-75°, 75°-105°, 105°-165° or most SFs are horizontal and span the long axis of the cell. 1 µM of Cytochalasin-D was added in the media for 30 minutes, taking images every 10 minutes. Cytochalasin-D was then washed off and cells reformed SFs for 2 hours 30 minutes. Cells were then sub-divided into 5 categories based on their final SF configurations (B) Representative images of the SF distribution (RFP-LifeAct) before Cytochalasin-D (first column), with 30 minutes of Cytochalasin-D incubation (second column) and after Cytoshalasin-D was washed off and cells reformed SFs (third column). (C) Comparison of the relative abundances of the initial SF configuration of 58 cells to the relative abundances of the final SF configurations of the same cells. Relative abundances are statistically insignificant.

3.4 Discussion

In this study, we have combined single-cell micropatterning and long term time-lapse imaging to elucidate how a single cell regulates its internal SF configuration to appreciate the parameters that contribute to the observed SF internal SF heterogeneity. Previous studies have concentrated on peripheral SF formation and curvature as cells spread on patterns as well as the interaction of SFs with the lamella/lamellipodium structures. Our results confirm that internal SFs are formed parallel to the lamella-like structures as the cell spreads over the pattern (16, 17). There are however other unexplored parameters that potentially contribute to this intricate relationship.

Our preliminary results show that the initial binding position of the cell and subsequent spreading history affect the internal SF distribution observed. For example, binding on the corner of the side-spacing pattern allows the cell to crawl forward across the long FN lines and form SFs that are perpendicular to these lines. Binding on the bottom FN line, however, forces the cell to first spread upwards across the short axis of the pattern leading to a triangular intermediate shape. At this intermediate stage, SFs formed are diagonal and parallel to the hypotenuse of the triangle. As the cell continues spreading on the top FN line, the SFs shift to more perpendicular angles. When the cell binds on either the long FN or the corner, there are two possible lamellas that can form and it remains unclear how the cell chooses which one will lead the spreading. More experiments are required to understand the molecular pathways and determine if this is a stochastic process.

We also show that the internal SF distribution depends on the geometry of the ECM. ECM geometry influences the spreading history of the cell since it forces the cell to jump through a spacing in the case of the top-spacing pattern that is not present on the side-spacing pattern. As a result, the SF distributions of top-spacing and side-spacing patterns are distinct even though the initial binding is the same. These results suggest that a cell may have an intrinsic memory that guides its SF architecture based on the ECM geometry it encounters and may provide an insight as to how cells in tissue form reproducible cytoskeletal structures.

It should be noted that further experimental and computational analysis is required to fully understand how a cell interacts with an adhesive pattern and how this interaction leads to varying SF configurations. First, our current analysis depended only on the final SF configuration. A future direction could include intermediate time points to understand the evolution of SFs during spreading and how parameters such as the geometry of the ECM may alter this evolution. This will allow us to develop computation models that simulate cell spreading based on initial binding position – a potentially useful approach in better understanding how cells interact with the ECM and process this signal to lead to a final SF configuration. Second, our analysis stops after ~8.5 hours. It is possible if not likely that after spreading, cells reinforce existing SFs and undergo further SF rearrangement to achieve an optimal tension distribution (16). It is important to understand how SFs evolve after 8.5 hours to ensure that the configuration we are analyzing is indeed the final configuration of the cell. Finally, to be able to compare the final SF configuration of various cells, it is important to ensure that we are comparing cells undergoing similar spreading events at the same time. As seen in Fig. 2, cells may sometimes spread fully on the pattern within 3 hours whereas some cells may require 8 hours to fully cover the pattern area.

One potential solution is to normalize the cells to a specific coverage area over the pattern rather than the first image of the time lapse. These promising results show the potential of our methodology to study the complex and unexplored question of how cells process the geometry of the ECM.

3.5 Materials and Methods

Cell lines and reagents: Viral particles of the pFUG-RFP-LifeAct vector were packaged in 293T cells and used to infect U2OS cells (ATCC HBT-96) (6). Cells expressing the pFUG-RFP-LifeAct vector were sorted on a DAKO-Cytomation MoFlo High Speed Sorter based on RFP fluorescence.

Cells were cultured in DMEM with 10% fetal bovine serum (JR scientific), 1% penicillin/strep (Thermo Fischer Scientific) and 1% Non-Essential Amino Acids (Life Technologies).

Deep-UV based pattern fabrication: Chrome quartz photomasks were designed using CleWin 4.0 and were printed from aBeam technologies (Hayward, CA). Patterns were made as described elsewhere (6, 12). Briefly, glass coverslips were coated with 0.01mg/ml PLL-PEG (Surface Solutions, Switzerland) in 10mM HEPES pH = 7.4 for 1 hour. After drying with air, coverslips were exposed to deep UV (UVO cleaner, Jetlight, USA) through a photomask. A drop of water was used to hold the coverslips on the photomask and care was taken to remove any excess liquid and air bubbles. After Deep UV incubation, coverslips were placed in DI water and left to incubate for at least 30 minutes. Coverslips were then incubated with 34.25 μg/ml of fibronectin (EMD Millipore Corporation) in 10mM HEPES pH = 8.5 for 1 hour at 37°C. Patterns were washed 3 x for 5 min in phosphate-buffered saline (PBS) before cells were plated.

Immunofluorescence staining: Cells were fixed with 4% paraformaldehyde for 10 minutes, and washed using PBS. Cells were permeabilized in 0.5% Triton-X for 15 minutes, and blocked in 5% goat serum (Thermo Fisher Scientific) for 1 hour. We then incubated the cells with the primary antibody for 2 hours at room temperature in a humidity chamber, followed by washing in 1% goat serum (3 x 5 minutes) and secondary incubation for 1 hour at room temperature. We used the following antibodies: vinculin (Sigma Aldrich), Alexa-fluor 647 anti-mouse (Thermo Fisher Scientific). F-actin was stained with 546-phalloidin. Immunofluorescence images were obtained using a swept-field upright confocal microscope equipped with a 60x water immersion lens (Prairie Technologies). For presentation purposes, the contrast and brightness of fluorescence images were optimized using ImageJ (NIH).

Time lapse experiments of cell spreading: Patterned coverslips were glued on the bottom of 6-well plates (MatTek corporation) and washed extensively with PBS to ensure no leakage and removal of any glue trace. 120,000 cells were seeded at t = 0 and media was changed 30 minutes after seeding to ensure that any cells that did not bind on patterns were removed. The plate was then placed on a heated stage on a Nikon Ti-Eclipse microscope 40 minutes after seeding. Time-lapse positions were saved and imaging began at 1 hour 20 minutes after seeding. Images of RFP-LifeAct were taken every 10 minutes for at least 7 hours using a 40x objective. A perfect focus system was used to ensure that SFs remained in focus during spreading.

Characterization of stress fiber architecture: Cells were first divided based on their initial binding positions on the pattern 80 minutes after seeding. For the top-spacing pattern, three positions were identified: right corner, left corner, and bottom FN edge. For the side-spacing pattern, cells bound on the left corner, on the top FN or the bottom FN edge. Cells were further manually subdivided into 5 categories depending on their final internal SF architecture configuration recorded at 8 hours 30 minutes after seeding. The 5 categories are: 1) no internal SFs visible, majority of internal SFs are aligned at angles between 2) 15°-75°, 3) 75°-105° (perpendicular), 4) 105°-165° and 5) horizontal SFs that span the length of the cell. Due to symmetry between left and right corner binding on the top-spacing patterns, we combined the relative counts after inverting the left distribution to match the right. Additionally, symmetry was observed between top- and bottom-edge binding on the side-spacing patterns, and the distributions were also combined to match the bottom-edge binding.

Cytochalasin-D incubation: For these experiments, cells were seeded as described above and allowed to spread in the incubator (37° Celsius and 5% CO_2) for 5 hours. The plate was placed on a heated stage and imaging positions were saved. SF architecture images were taken at 6 hours after seeding. 1.5ml of 2 µM Cytochalasin-D + U2OS media was added in the well resulting in a final concentration of 1 µM Cytochalasin-D. Images were taken every 10 minutes for 30 minutes. Cytochalasin-D was washed off the cells by adding fresh media (repeated at least four times). Images were taken every 10 minutes after Cytochalasin-D removal for at least 2 hours 30 minutes.

Statistical analysis: All statistical analyses and graphing were performed using Prism 7.02. Unless otherwise noted, relative frequencies were compared using a χ^2 test.

3.6 Acknowledgements

This work was performed in part at the CRL Molecular Imaging Center supported by NIH 3R01EY015514-01S1. Confocal images were obtained at the CIRM/QB3 Stem Cell Shared Facility. EK gratefully acknowledges the support of the Howard Hughes Medical Institute International Student and Siebel Scholar fellowships. This work was supported from the National Institute of Health (1R21EB016359), the National Science Foundation (CAREER Award CMMI-1055965) and the France-Berkeley Fund. EK gratefully acknowledges Anne-Lou Roguet, a visiting Masters student from Ecole Polytechnique who helped with experiments.

1. Kassianidou E, Kumar S (2015) A biomechanical perspective on stress fiber structure and function. *Biochim Biophys Acta - Mol Cell Res* 1853(11, Part B):3065–3074.
2. Tojkander S, Gateva G, Lappalainen P (2012) Actin stress fibers - assembly, dynamics and biological roles. *J Cell Sci* 125(Pt 8):1855–1864.
3. Ulrich T a, de Juan Pardo EM, Kumar S (2009) The mechanical rigidity of the extracellular matrix regulates the structure, motility, and proliferation of glioma cells. *Cancer Res* 69(10):4167–74.
4. Zemel A, Rehfeldt F, Brown AEX, Discher DE, Safran SA (2010) Optimal matrix rigidity for stress-fibre polarization in stem cells. *Nat Phys* 6(6):468–473.

5. Chaudhuri O, et al. (2015) Hydrogels with tunable stress relaxation regulate stem cell fate and activity. *Nat Mater* advance on(November). doi:10.1038/nmat4489.

6. Kassianidou E, Brand CA, Schwarz US, Kumar S (2017) Geometry and network connectivity govern the mechanics of stress fibers. *Proc Natl Acad Sci* 114(10):2622–2627.

7. Soiné JRD, et al. (2015) Model-based Traction Force Microscopy Reveals Differential Tension in Cellular Actin Bundles. *PLoS Comput Biol* 11(3):e1004076.

8. Chang C-W, Kumar S (2013) Vinculin tension distributions of individual stress fibers within cell-matrix adhesions. *J Cell Sci* 126(Pt 14):3021–3030.

9. Hotulainen P, Lappalainen P (2006) Stress fibers are generated by two distinct actin assembly mechanisms in motile cells. *J Cell Biol* 173(3):383–94.

10. Saitoh T, et al. (2001) Differential localization of non-muscle myosin II isoforms and phosphorylated regulatory light chains in human MRC-5 fibroblasts. *FEBS Lett* 509(3):365–9.

11. Cramer LP, Siebert M, Mitchison TJ (1997) Identification of novel graded polarity actin filament bundles in locomoting heart fibroblasts: Implications for the generation of motile force. *J Cell Biol* 136(6):1287–1305.

12. Azioune A, Carpi N, Tseng Q, Théry M, Piel M (2010) Protein micropatterns: A direct printing protocol using deep UVs. *Methods Cell Biol* 97(10):133–146.

13. Loosli Y, et al. (2013) An actin length threshold regulates adhesion maturation at the lamellipodium/lamellum interface. *Integr Biol* 5(6):865.

14. Loosli Y, Luginbuehl R, Snedeker JG (2010) Cytoskeleton reorganization of spreading cells on micro-patterned islands: a functional model. *Philos Trans A Math Phys Eng Sci* 368(1920):2629–2652.

15. Zemel A, Rehfeldt F, Brown AEX, Discher DE, Safran SA (2010) Cell shape, spreading symmetry and the polarization of stress-fibers in cells. *J Phys Condens Matter* 22(19):194110.

16. Théry M, Pépin A, Dressaire E, Chen Y, Bornens M (2006) Cell distribution of stress fibres in response to the geometry of the adhesive environment. *Cell Motil Cytoskeleton* 63(6):341–355.

17. Tojkander S, Gateva G, Husain A, Krishnan R, Lappalainen P (2015) Generation of contractile actomyosin bundles depends on mechanosensitive actin filament assembly and disassembly. *Elife* 4:e06126.

Appendix II. Supplementary figures for Chapter 3

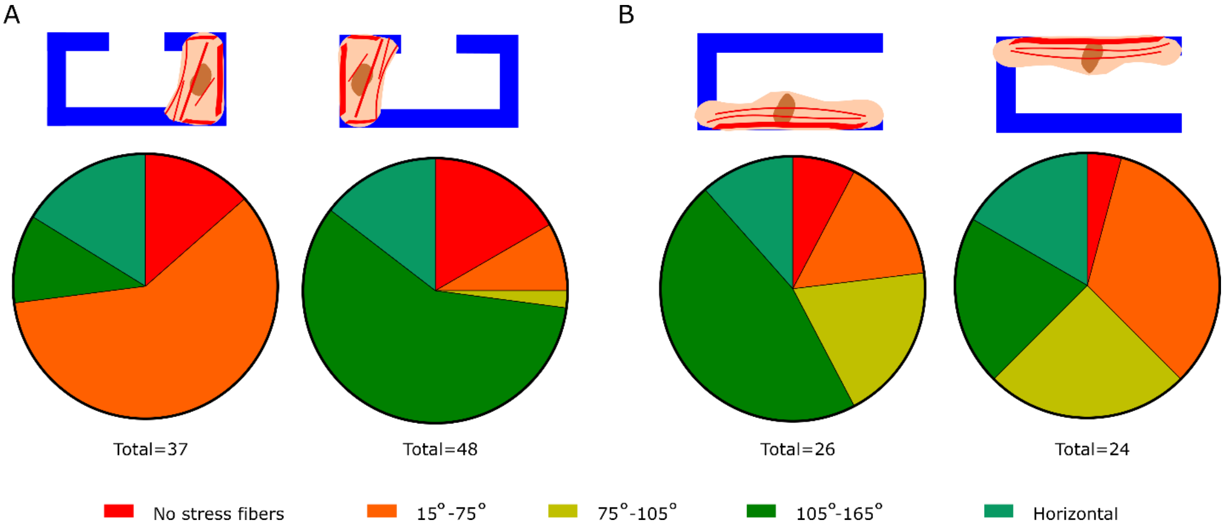

Figure S1: Cells exhibit symmetric final internal SF distributions when they bind on opposing sides of symmetric patterns. (A) Comparison of final internal SF distribution of cells bound on the right or left corner of the symmetric top-spacing pattern. Relative abundances of final internal SF configurations based on initial binding positions are statistically different based on a χ^2 test and symmetric (N = 37 cells bound on the left corner and 48 cells bound on the right corner). (B) Comparison of final internal SF distribution of cells bound on the top or bottom long FN edges of the symmetric side-spacing pattern (N = 26 cells bound at the bottom long FN edge and 24 cells bound the top long FN edge).

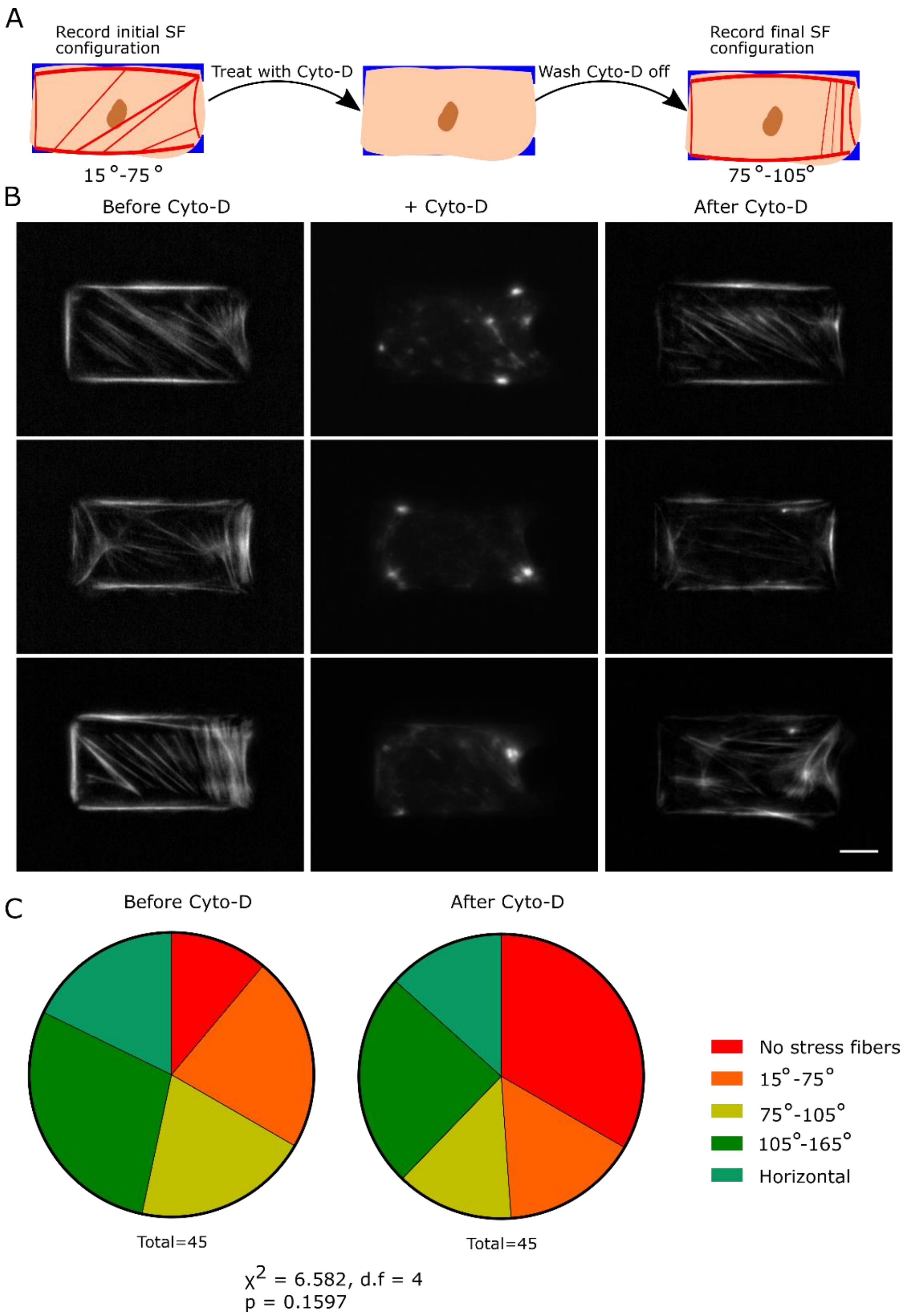

Figure S2: Cells seeded on the side-spacing pattern maintain a memory of the SF distribution after SF depolymerization using Cytochalasin-D (A) Schematic of experimental set-up. U2OS RFP-LifeAct cells spread on the side-spacing patters for 6 hours and images of the internal SF architecture were obtained and cells were sub-divided into 5 categories: no internal SFs visible, majority of SFs are angled between 15°-75°, 75°-105°, 105°-165° or most SFs are horizontal and span the long axis of the cell. 1 µM of Cytochalasin-D was added in the media for 30 minutes, taking images every 10 minutes. Cytochalasin-D was then washed off and cells reformed SFs for 2 hours 30 minutes. Cells were then sub-divided into 5 categories based on their final SF configurations (B) Representative images of the SF distribution (RFP-LifeAct) before Cytochalasin-D (first column), with 30 minutes of Cytochalasin-D incubation (second column) and after Cytoshalasin-D was washed off and cells reformed SFs (third column). (C) Comparison of the relative abundances of the initial SF configuration of 45 cells to the relative abundances of the final SF configurations of the same cells. Relative abundances are statistically insignificant.

Chapter 4. ROCK and MLCK contribute to stress fiber viscoelasticity via preferential phosphorylation of myosin light chain

4.1 Abstract

Stress fibers (SFs) are contractile bundles of actin and non-muscle myosin II that can generate and transmit forces within the cell. Generation of force is dependent on myosin light chain (MLC) phosphorylation – a process that can occur either via Myosin Light Chain Kinase (MLCK) or Rho associated Kinase (ROCK). Previous work has shown that MLCK regulates formation of peripheral SFs whereas ROCK regulates formation of central SFs. It is unclear, however, how this compartmentalized regulation takes place and whether MLCK and ROCK preferentially affect SF mechanical properties. We combined subcellular laser ablation with a genetic strategy that allows us to express constitutively active forms of ROCK isoforms and MLCK in an inducible manner. We showed that ROCK and MLCK preferentially phosphorylate MLC in an inducible manner – ROCK phosphorylates Thr18/Ser19 whereas MLCK phosphorylates Ser19. Di-phosphorylated myosin induced by ROCK isoforms localizes at the central regions of the cell, whereas mono-phosphorylated MLC induced by MLCK localizes primarily at the periphery. We have shown that graded expression of ROCK and MLCK regulates the mechanical properties of central and peripheral SFs in a graded manner respectively. Finally, to show that ROCK and MLCK regulate SF tension generation via MLC phosphorylation directly, we ablated SFs in cells expressing phosphomimetic MLC and the results mimicked those obtained by inducible expression of MLCK and ROCK respectively. Overall, our results provide further insight into how cells can differentially regulate tension generation in different subsets of SFs via regulation of MLC phosphorylation from ROCK and MLCK. We also show for the first time, that SF tension can follow gradient MLC phosphorylation trends – a finding that can enhance our understanding of SF mechanics and force generation.

4.2 Introduction

Actomyosin stress fibers (SFs) enable mammalian cells to generate traction forces against the extracellular matrix (ECM) that are very important to the regulation of cell shape and migration. (1–3). At the multicellular level, these forces also contribute significantly to tissue morphogenesis, wound healing, and neoplasia (4, 5). SFs are composed of F-actin, structural proteins such as α-actinin, and, frequently, non-muscle myosin II (NMMII) (2, 6). When NMMII filaments are present, SFs generate tension that is transmitted along the length of the SF to ECM adhesions and surrounding cytoskeletal elements (7). As such, SFs are capable of acting both locally and globally through their networked interactions with other cellular structures to impose tensile loads within the cell (8).

NMMII is a hexamer that consists of two essential light chains (ELCs), two myosin light chains (MLCs) and two heavy chains (9, 10). The heavy chains contain the head domain, which is a globular structure that can both directly engage F-actin and hydrolyze ATP to provide the free energy required to power the contractile sliding of the thick filaments against the thin filaments, thus creating tension within the stress fiber.

MLC has multiple phosphorylation sites that control myosin filament formation and activity. Phosphorylation of the MLC allows NMMII to uncoil and assemble into linear thick filaments (10). Phosphorylation of Ser19 activates the motor domain and phosphorylation of Thr18 and Ser19 further enhances the ATPase activity (11–13). While both mono-phosphorylated (Ser19) and di-phosphorylated (Thr18/Ser19) NMMII are observed within peripheral as well as central SFs, their overall effect in the mechanical properties of SFs has not been addressed (14–16).

MLC can be phosphorylated by two orthogonal pathways, the Myosin Light Chain Kinase (MLCK) and RhoA/ROCK pathways: MLCK can directly phosphorylate MLC whereas ROCK can promote MLC phosphorylation through either direct MLC phosphorylation or MLC phosphatase inactivation. Experiments using inhibitors for each kinase have shown that MLCK preferentially contributes to the formation of peripheral SFs whereas ROCK preferentially contributes to the formation of central SFs (17, 18). SF mechanical properties also vary depending on their cellular location – using subcellular laser ablation to study SF recoil kinetics, it was shown that peripheral SFs dissipate more elastic energy than central SFs (18). Moreover, it has been shown that ROCK regulates the amount of di-phosphorylated myosin whereas MLCK affected both mono-phosphorylated and di-phosphorylated myosin (19–21) . This begs the question whether ROCK and MLCK preferentially control central and peripheral SF formation and mechanical properties by preferential phosphorylation of MLC.

Studying the relative role of these pathways to SF mechanics with traditional pharmacological tools has been challenging, as inhibition of either ROCK or MLCK can produce wholesale SF disassembly (17, 18). Moreover, these drugs are very difficult to use in anything other than an “on/off” fashion, defying attempts to understand the effect of graded changes in myosin activation on SF retraction. For example, it is currently unclear whether the cell senses graded changes in myosin activation and tunes SF tension accordingly or if there is a threshold point of myosin activation above which the tension within SFs changes drastically. Thus, it is important to determine both the differential role of ROCK and MLCK to SF mechanics and the degree at which graded changes of kinase activation translate into changes in SF mechanical properties, in order to fully comprehend how a SF generates and transmits force.

In this chapter, we aim to examine in more detail the molecular mechanisms responsible for the preferential control of ROCK and MLCK on SF mechanical properties. We show for the first time to our knowledge, that ROCK regulates central SF retraction kinetics via increased di-phosphorylation of MLC whereas MLCK regulates peripheral SF retraction kinetics via increased mono-phosphorylation of MLC. Moreover, we show that SF mechanical properties can be graded, providing further clarification in the relationship between myosin activation and SF force generation. Overall, our findings provide further insight into the molecular pathways that control SF force generation and provide clues as to how SF tension generation is controlled and regulated within the cell.

4.3 Results

To understand how gradient expression of ROCK and MLCK affect the viscoelastic properties of SFs, we used a lentiviral gene delivery system to introduce mutants of ROCK and MLCK under a doxycycline inducible promoter into U2OS RFP-LifeAct cells (Fig. 1A) (22, 23). Myc tagged p160ROCK Δ3 (CA-ROCK 1) and ROCK CAT (CA-ROCK 2) are lacking the RhoA binding domain rendering them constitutively active, whereas flag-tagged MLCK ED785-786KK (CA-

MLCK) is mutated to prevent MLCK autoinhibition (24–26). To first confirm that we can express the kinases in a graded manner by tuning the amount of doxycycline in the cell culture media, we measured the expression levels of CA-MLCK (Fig. 1B) and CA-ROCK 2 (Fig. 1C) via Western blotting. As expected, we were unable to detect CA-MLCK or CA-ROCK 2 in the absence of doxycycline as well as in control cells that were transduced with a lentiviral vector with no encoded gene. As the amount of doxycycline was increased, the expression of each kinase also increased showing a strong positive association (Spearman correlation coefficient ρ = 0.8891 for CA-MLCK and 0.7733 for CA-ROCK 2).

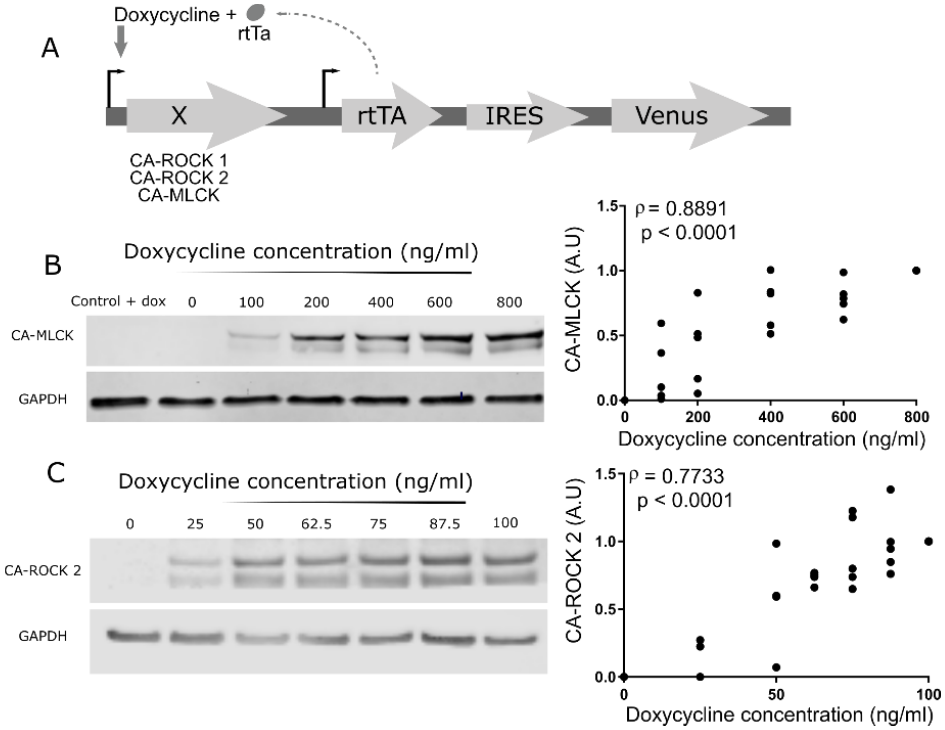

Figure 1: Graded control over the expression of a constitutively active form of MLCK (CA-MLCK) and a constitutively active form of ROCK 2 (CA-ROCK 2). (A) Schematic of doxycycline inducible lentiviral system. (B) Western Blot showing CA-MLCK expression levels in U2OS control and CA-MLCK cells in varying amounts of doxycycline. Expression levels of CA-MLCK were quantified (n > 4 blots) and normalized to CA-MLCK cells + 800 ng/ml doxycycline (Spearman correlation coefficient ρ = 0.8891, $p < 0.001$). (C) Western Blot showing CA- ROCK 2 expression levels in U2OS CA-ROCK 2 cells in varying amounts of doxycycline. Expression levels of CA-ROCK 2 were quantified (n > 4 blots) and normalized to CA-ROCK 2 cells + 100 ng/ml doxycycline (Spearman correlation ρ = 0.7733, $p < 0.001$).

To determine whether the changes in the expression of kinases translate to downstream effects, we looked at the extend of MLC phosphorylation. First, we cultured CA-MLCK, CA-ROCK 1 and CA-ROCK 2 cells with and without doxycycline and probed for either mono-phosphorylated (Ser19) or di-phosphorylated (Thr18/Ser19) MLC via Western blotting. In the case of CA-MLCK cells, we observed a significant increase in the amount of mono-phosphorylated myosin and a slight, yet statistically insignificant increase in the amount of di-phosphorylated myosin (Fig. 2A). For both CA-ROCK 1 and CA-ROCK 2 cells, we observed a significant increase in the di-phosphorylation of MLC and no increase in the mono-phosphorylation (Fig. 2B). These results support previously published work that shows a differential phosphorylation effect on MLC by each kinase and actually expand on these results since we observe a clear preference of phosphorylation by each kinase (19, 20).

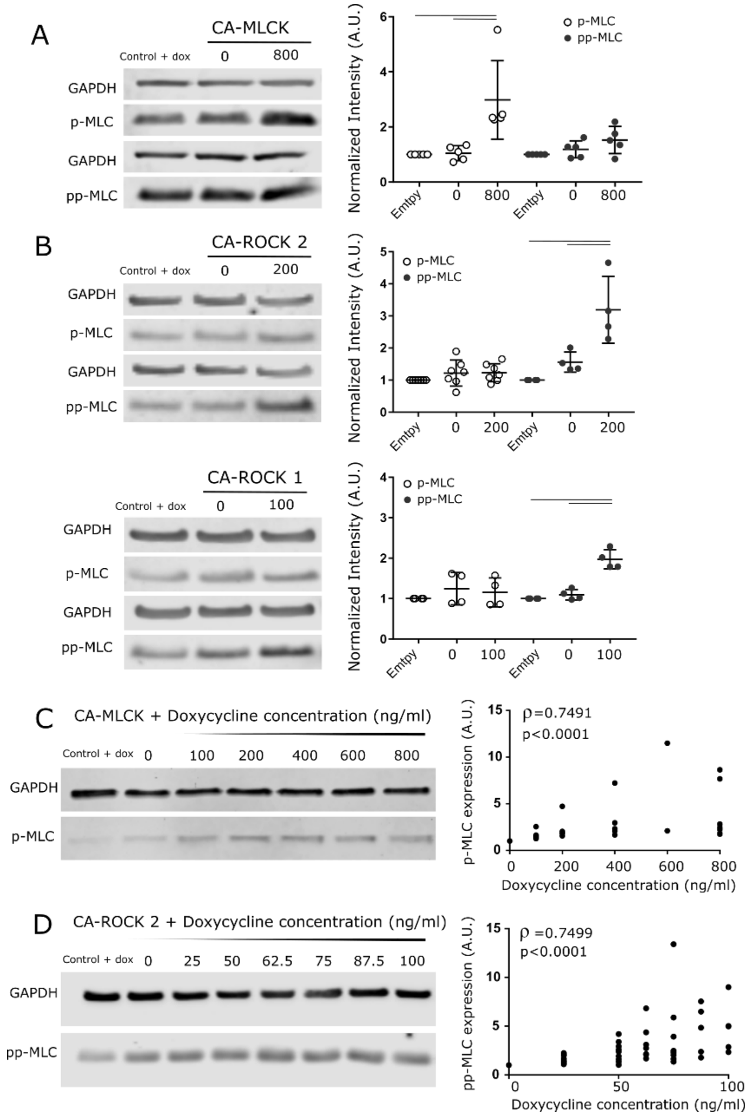

Figure 2: Expression of MLCK and ROCK isoforms leads to differential phosphorylation of MLC. (A) Expression of CA-MLCK leads to a statistical increase in the phosphorylation of Ser19 on MLC and a slight increase in the phosphorylation of Thr18/Ser19 on MLC. Phosphorylation levels were quantified and normalized to GAPDH and Control cells cultured in doxycycline (n = 4 blots, $p < 0.01$ by ANOVA followed by Tukey Kramer). (B) Expression of CA-ROCK isoforms leads to a statistical increase in the di-phosphorylation of MLC (Thr18/Ser19) and no observable chance in the mono-phosphorylation of MLC ($n > 4$ blots for each isoform, $p <0.05$). (C) Western blot demonstrating that graded doxycycline concentration translates to graded changes in the level of mono-phosphorylation of MLC in CA-MLCK cells. Phosphorylation levels were quantified and normalized to GAPDH and CA-MLCK + no doxycycline condition ($n > 5$ blots, Spearman coefficient $\rho = 0.7491$, $p < 0.001$). (D) Western blot demonstrating that graded doxycycline concentration translates to graded changes in the level of di-phosphorylation of MLC in CA-ROCK 2 cells. Phosphorylation levels were quantified and normalized to CA-ROCK 2 + 0 ng/ml doxycycline ($n > 5$ blots, Spearman coefficient = 0.7499, $p < 0.0001$).

To test whether the graded expression of kinases translates to graded phosphorylation of myosin, we cultured CA-MLCK and CA-ROCK 2 cells in varying concentrations of doxycycline and probed for mono-phosphorylated and di-phoshorylated MLC respectively. We observed a strong positive association between the amount of doxycycline and mono-phosphorylated MLC for CA-MLCK cells (Fig. 2C) and the amount of doxycycline and di-phosphorylated MLC for CA-ROCK 2 cells (Fig. 2D). We are therefore able to translate graded changes of kinase expression to graded downstream phosphorylation of MLC through our inducible promoter.

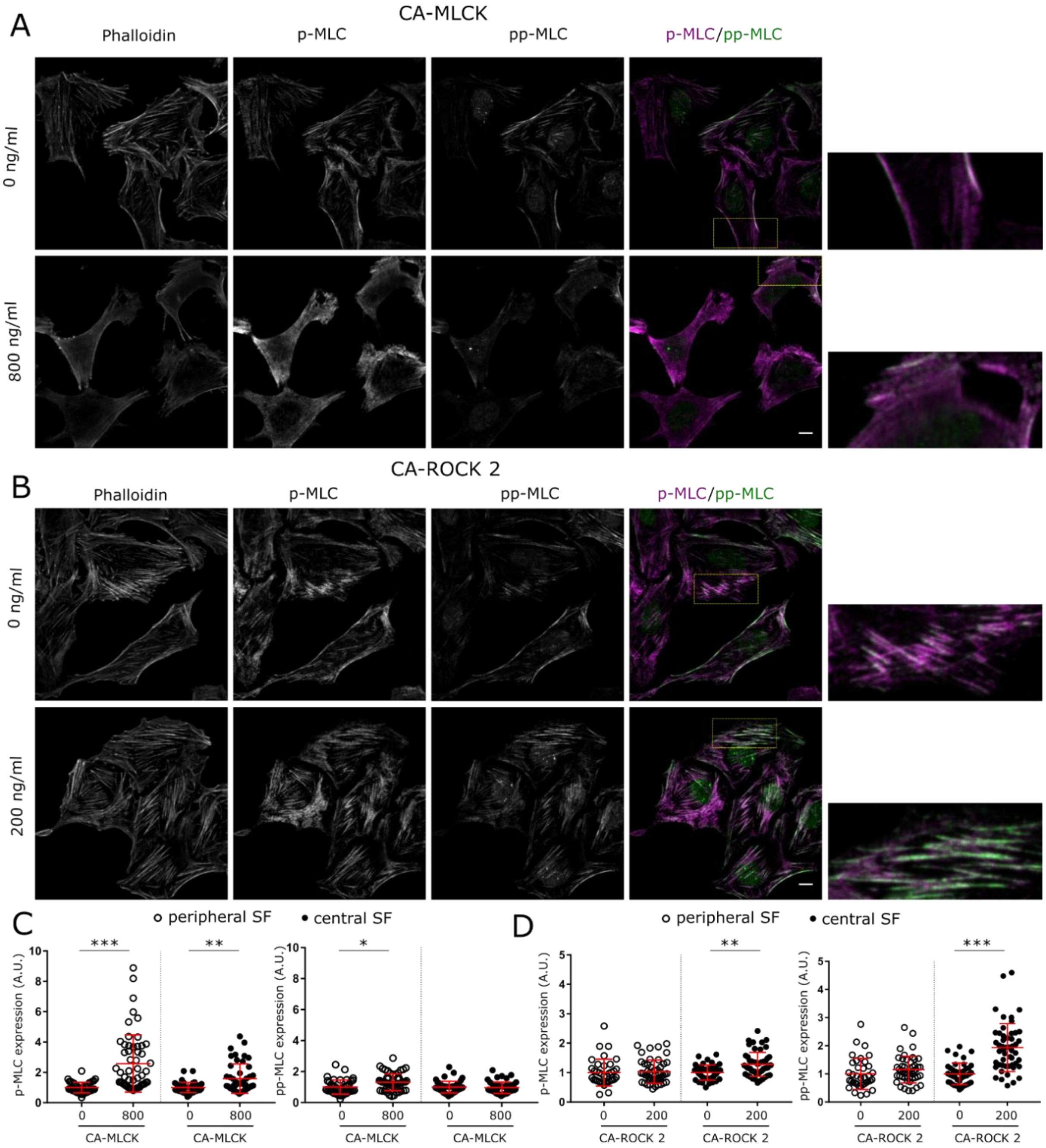

Figure 3: MLCK and ROCK expression regulate MLC phosphorylation changes in a localized manner. Representative fluorescence images of (A) CA-MLCK cells and (B) CA-ROCK 2 cultured in the presence and absence of doxycycline stained for mono-phosphorylated, di-phosphorylated myosin and F-actin. (C) Quantification of immunofluorescence intensity of mono-phosphorylated (left) and di-phosphorylated MLC (right) within peripheral (empty circles) and central SFs (full circles) for CA-MLCK cells cultured in the presence and absence of doxycycline ($n > 41$ cells for all conditions collected from 3 independent experiments). Intensities were normalized to the average intensity value of CA-MLCK cells cultured in the absence of doxycycline per each experiment. (D) Quantification of immunofluorescence intensity of mono-phosphorylated (left) and di-phosphorylated MLC (right) within peripheral (empty circles) and central SFs (full circles) for CA-ROCK 2 cells cultured in the presence and absence of doxycycline ($n > 37$ cells for all conditions collected from 3 independent experiments). Intensities were normalized to the average intensity value of CA-ROCK 2 cells cultured in the absence of doxycycline per each experiment (* = $p < 0.05$, ** = $p < 0.005$, *** = $p < 0.0001$, Mann-Whitney Test). Scale bars = 10 μm.

Previous work has shown that inhibition of ROCK via Y-27632 led to the breakdown of central stress fibers, whereas inhibition of MLCK via ML-7 led to the breakdown of peripheral stress fibers, suggesting that the two kinases are active in different cellular compartments (27, 28). To test whether the increases in phosphorylation levels correspond to the suggested cellular compartments (increase in mono-phosphorylation in CA-MLCK cells and increase in di-phosphorylation in CA-ROCK 2 cells), we stained CA-MLCK and CA-ROCK 2 cells cultured in the presence and absence of doxycycline for each MLC phosphorylation state (Fig. 3A and B). As a control, we also stained cells that were transduced with an empty vector. In both CA-MLCK and CA-ROCK 2 cells not treated with doxycycline, we observed a strong localization of di-phosphorylated myosin on both peripheral and central SFs. Mono-phosphorylated myosin, however, was localized more diffusely on both peripheral and central SFs. Overall, we observed that CA-ROCK 2 cells cultured in doxycycline expressed thicker central SFs and in some cases, cells had acquired a star-like SF architecture (Appendix III – Fig. S1). CA-MLCK cells cultured in doxycycline seemed to have less central SFs and in some cases, cells had acquired an elongated shape (Appendix III – Fig. S1).

We then quantified the amount of mono- and di-phosphorylated myosin over peripheral and central SFs within CA-MLCK (Fig. 3C) and CA-ROCK 2 cells (Fig. 3D) in the presence and absence of doxycycline. We observed that expression of CA-MLCK resulted in an increase in the amount of mono-phosphorylated myosin for both central and peripheral SFs (Fig. 3C, left graph). The effect in peripheral SFs however was overwhelmingly stronger compared to the increase in central SFs (empty versus dark circles). A small statistical increase was also observed in the amount of di-phosphorylated myosin present in peripheral but not central SFs (Fig. 3C, right graph). Overall, CA-MLCK expression primarily contributes to mono-phosphorylation of myosin as supported by Fig. 2, and the increased mono-phosphorylated myosin localizes primarily on peripheral SFs. Expression of CA-ROCK 2 however resulted in an increase in the amount of both mono-phosphorylated (Fig. 3D, left graph) and di-phosphorylated myosin (Fig. 3D, right graph) in central SFs but no such increase was observed in peripheral SFs (empty versus dark circles). Overall, CA-ROCK 2 expression leads to more di-phosphorylated myosin that localizes primarily on central SFs. CA-ROCK 2 and CA-MLCK cells cultured in no doxycycline show similar localization and intensity levels of mono-phosphorylated and di-phosphorylated MLC as the cells transduced with an empty vector (Appendix III – Fig. S2). Overall, immunostaining results match the results obtained from Western blotting (Fig. 2) and previously published work – ROCK promotes di-phosphorylation of MLC primarily in the central cellular regions whereas MLCK promotes mono-phosphorylation of MLC primarily in the periphery.

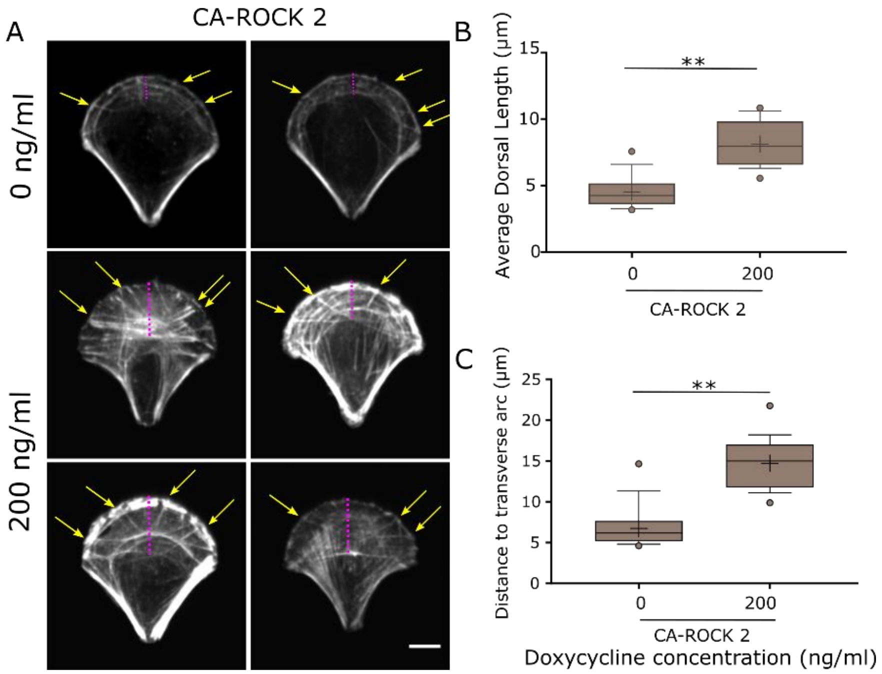

Figure 4: Expression of CA-ROCK 2 increases average dorsal SF length and distance of last transverse arc from cell edge. (A) CA-ROCK 2 cells cultured in the presence and absence of doxycycline and seeded on crossbow patterns exhibit differences in their SF subtype architecture. Yellow arrows point to examples of dorsal SFs and magenta dashed line indicates distance from cell edge to last transverse arc. (B) Quantification of average dorsal SF length per CA-ROCK 2 cells cultured in the presence and absence of doxycycline. (C) Quantification of the distance from the cell edge to the last transverse arc in CA-ROCK 2 cells seeded on crossbow patterns and cultured in the presence and absence of doxycycline. (n = 14 and 19 cells respectively). Statistical differences determined using Mann-Whitney test (** = $p < 0.001$). Boxes represent 25th and 75th percentiles; whiskers represent 10th and 90th percentiles. Cross represents the mean of the distribution.

As shown in Appendix III – Fig. S1, CA-ROCK 2 cells cultured in 200 ng/ml doxycycline sometimes form thick central SFs and sometimes acquire a star-like SF architecture. We hypothesized that increased contractility in the central regions of the cells led to increased contractility in transverse arcs causing them to contract and form the observed star-like structures. To investigate this, we seeded CA-ROCK 2 cells on cross-bow shaped patterns to allow cells to form all subtypes of stress fibers – dorsal, transverse arcs, ventral and peripheral SFs – while maintaining the same cell area and shape (Fig. 4A). We then measured dorsal SF length and the distance from the lamella’s edge to the last transverse arc observed in our phalloidin images. We found that CA-ROCK 2 cells cultured in doxycycline showed an increase in the average dorsal SF length as well as an increase in the distance of the last transverse arc to the lamella (Fig. 4B-C). Overall, we have shown that increased contractility in the central region of the cell causes the transverse arcs to contract and move further away from the cellular edge causing the dorsal SF length to increase suggesting that expression of kinases can alter the arrangement of SFs.

To determine if the localized changes in myosin phosphorylation caused by each kinase translate to changes in the mechanical properties of SFs, we performed subcellular laser ablation on both central and peripheral SFs of CA-ROCK 1, CA-ROCK2 and CA-MLCK cells cultured in the presence and absence of doxycycline. As in our previous studies, we follow the SF ends as they move away from each other and fit each retraction curve to a Kelvin-Voigt viscoelastic cable model described by a time constant (τ), which reflects the SF's effective viscosity/elasticity ratio, and a plateau retraction distance (L_o), which correlates to the elastic energy dissipated by half of the severed SF (Fig. 5A, Appendix III – Fig. S3 for examples of SF architectures being ablated). Peripheral SF retraction kinetics were unchanged in the presence of either CA-ROCK isoform (Fig. 5B and C). Both retraction kinetics (L_o and τ) of peripheral SFs were statistically increased when CA-MLCK is expressed (Fig. 5B and C). Central SF retraction kinetics (both L_o and τ) however were regulated by the expression of both CA-ROCK isoforms and were unchanged by expression of CA-MLCK (Fig. 5D and E). Our results definitively show that ROCK regulates the mechanical properties of central SFs whereas MLCK dominates the mechanical properties of peripheral SFs.

The strength of our inducible promoter system is the ability to express each kinase in a gradient manner (Fig. 1) leading to graded changes in the level of phosphorylated MLC (Fig. 2). We wondered whether graded changes in the phosphorylation can indeed translate to graded changes in mechanical properties of SFs or whether SFs need a certain level of phosphorylation activation and once that threshold is passed, SFs become more tensile. Graded expression of CA-MLCK by varying doxycycline concentration preferentially increased the mechanical properties of peripheral SFs in a graded manner whereas graded expression of CA-ROCK 2 via varying doxycycline concentration preferentially increased the mechanical properties of central SFs (Appendix III – Fig. S4). Peripheral SF mechanical properties of CA-ROCK 2 cells and central SF mechanical properties of CA-MLCK cells cultured in varying amounts of doxycycline remained unchanged (Appendix II – Fig. S4). SF retraction kinetics of CA-ROCK 2 and CA-MLCK cells were also plotted versus the induced gradient of mono-phosphorylated and di-phosphorylated myosin respectively obtained by Western blotting (Fig. 2D and E). We observed a positive correlation between increased mono-phosphorylated myosin expression and increased L_o of peripheral SFs in CA-MLCK cells (Fig. 6A) as well as a positive correlation between increased di-phosphorylated myosin expression and increased L_o values of central SFs in CA-ROCK 2 cells (Fig. 6A). Surprisingly, the mechanical properties of central SFs in CA-ROCK 2 cells cultured in 100 ng/ml doxycycline (last point on graph) match those of peripheral SFs. We also observed an increase in τ of peripheral SF ablation of CA-MLCK cells with increased mono-phosphorylated MLC (Fig. 6B) as well as a positive correlation between τ and di-phosphorylated myosin expression in central SF ablation of CA-ROCK 2 cells (Fig. 6C). These results suggest that SF mechanical properties are indeed tunable based on the amount of phosphorylated MLC present.

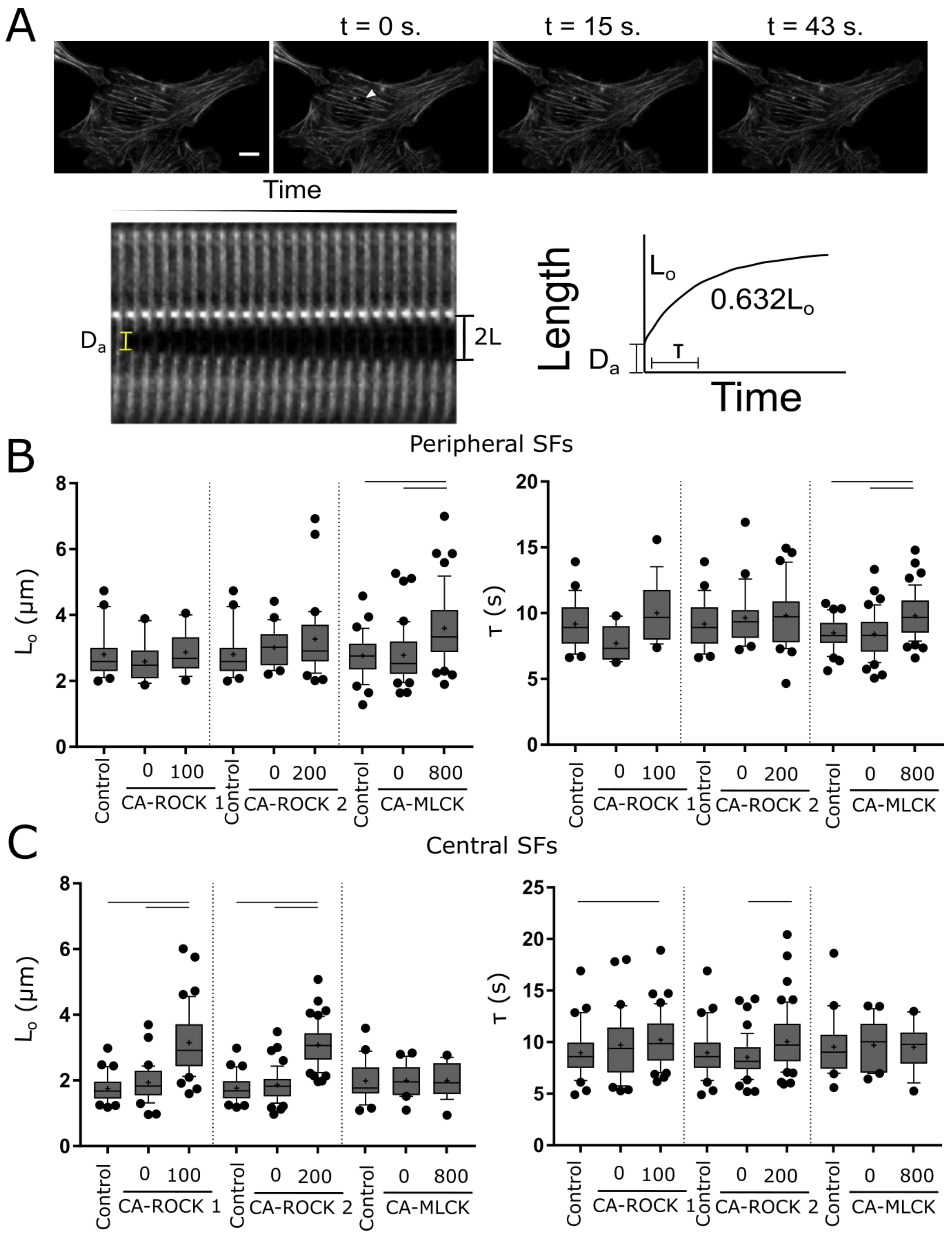

Figure 5: MLCK and ROCK regulate the mechanical properties of distinct subpopulations of SFs. (A) SF Retraction analysis. D_a - SF material destroyed by ablation, 2L - distance between fiber ends over time (L is the retraction distance of a severed SF fragment). Length L vs time t is fit to the Kelvin-Voigt model to determine L_o, whose magnitude correlates with the SF's dissipated elastic energy, and τ, the viscoelastic time constant which is the ratio of viscosity/elasticity. (B) L_o and τ values of peripheral SF ablation for CA-ROCK 1, CA-ROCK 2 and CA-MLCK cells cultured in the presence and absence of doxycycline (n= 25, 12, 16 for CA-ROCK 1 plot, n = 25, 21 and 32 for CA-ROCK 2 plot, n = 33, 42, 47 for CA-MLCK plot). Statistical differences only observed in the presence of CA-MLCK (* = $p < 0.005$, Kruskal Wallis followed by Dunn test). (C) L_o and τ values of central SF ablation for CA-ROCK 1, CA-ROCK 2 and CA-MLCK cells cultured in the presence and absence of doxycycline (n= 33, 33, 43 for CA-ROCK 1 plot, n = 34, 41, 59 for CA-ROCK 2 plot, n = 22, 22, 19 for CA-MLCK plot). Statistical differences only observed in the presence of CA-ROCK isoforms (* = $p < 0.005$, Kruskal Wallis followed by Dunn test). Boxes represent 25th and 75th percentiles; whiskers represent 10th and 90th percentiles. Cross represents the mean of the distribution.

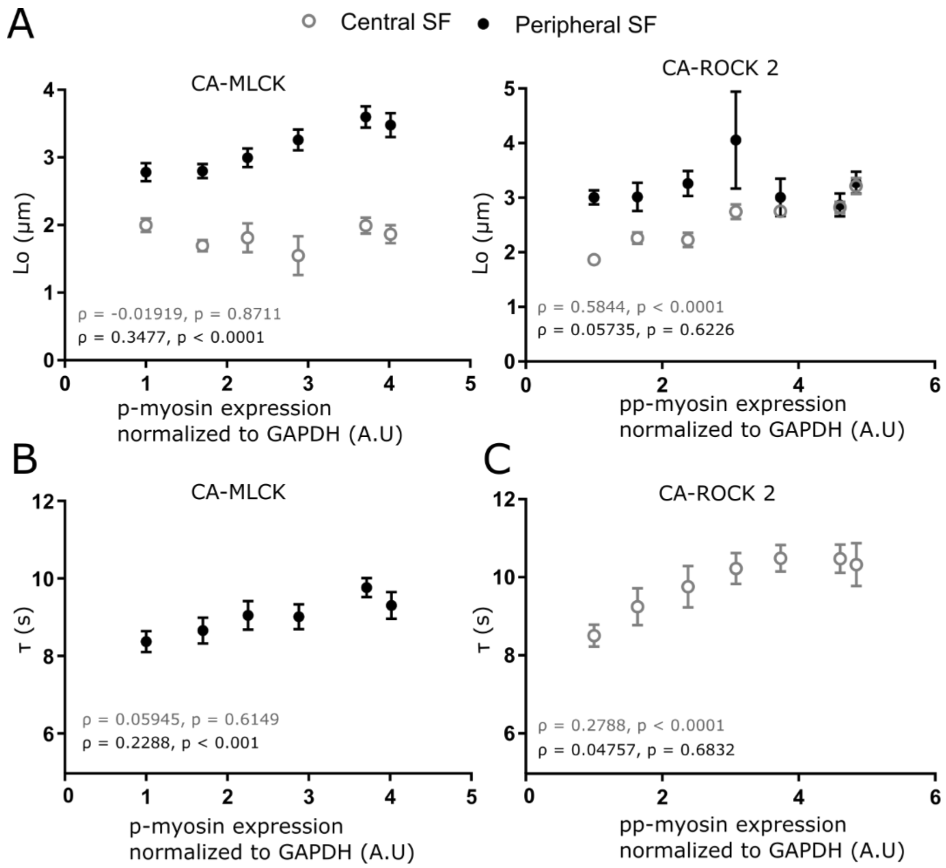

Figure 6: SF mechanical properties increase in a graded manner following graded expression of kinases and graded phosphorylation of MLC. (A) L_o of central (empty circles) and peripheral (full circle) SF ablation of CA-MLCK and CA-ROCK 2 cells cultured in varying concentrations of doxycycline (n = 42, 24, 39, 37, 25, 47 cells for peripheral SF ablation of CA-MLCK, n = 22, 14, 7, 3, 9, 19 cells for central SF ablation of CA-MLCK cells, n = 21, 4, 6, 4, 6, 14, 21 cells for peripheral SF ablation of CA-ROCK 2 cells, n = 49, 41, 31, 25, 40 and 38 cells for central SF ablation of CA-ROCK 2 cells). (B) τ values of peripheral SF ablation for CA-MLCK cells cultured in varying amounts of doxycycline (n = 42, 24, 39, 37, 25, 47 cells per concentration plotted). (C) τ values of central SF ablation for CA-ROCK 2 cells cultured in varying concentrations of doxycycline (n = 49, 41, 31, 25, 40 and 38 cells per concentration plotted). Spearmann correlation coefficients ρ and p-values shown at the bottom of each were calculated using all data points, and are shown at the bottom of each graph. Gray values correspond to central SF ablation analysis whereas black values correspond to peripheral SF ablation analysis.

Our results so far suggest that the two kinases phosphorylate MLC in a preferential manner - MLCK preferentially phosphorylates Ser19 whereas ROCK isoforms phosphorylate Thr18 and Ser19 (Fig 2). We also show that these changes in phosphorylation have specific localizations – mono-phosphorylated myosin via MLCK activation localizes primarily in the periphery of the cell whereas di-phosphorylated myosin via ROCK activation localizes in the center (Fig. 3). Finally, we show SF mechanical properties are also regulated via the kinases – ROCK controls central SF retraction kinetics, whereas MLCK controls peripheral retraction kinetics (Fig. 5 and 6). It is unclear, however, if the SF mechanical changes observed are truly due to phosphorylation changes by the kinases or due to other kinase targets such as LIMK and cofilin. To provide a direct link between the kinases, phosphorylation state of MLC and SF mechanics, we transduced U2OS RFP-LifeAct cells with mono-phosphomimetic MLC where Ser19 was mutated to Asp (MLC-AD) and with di-phosphomimetic MLC where both Thr18/Ser19 were mutated to Asp (MLC-DD) (16). We performed SLA on central and peripheral SFs of MLC-AD and MLC-DD cells and observed that overexpression of MLC-DD only affected the elastic energy dissipated by central SFs (L_o) but not peripheral ($p < 0.0001$, $p = 0.7223$). Overexpression of MLC-AD however only affected the elastic energy dissipated by peripheral SFs (L_o) ($p = 0.0293$) and not central ($p = 0.6326$). The retraction kinetics observed match the retraction kinetics obtained by CA-ROCK 2 cells in the presence of 50 ng/ml and CA-MLCK cells in the presence of 400 ng/ml which correspond to intermediate points on our gradient expression. These results suggest that the changes in the retraction kinetics observed from the increased expression of kinases are directly due to the changes in MLC phosphorylation.

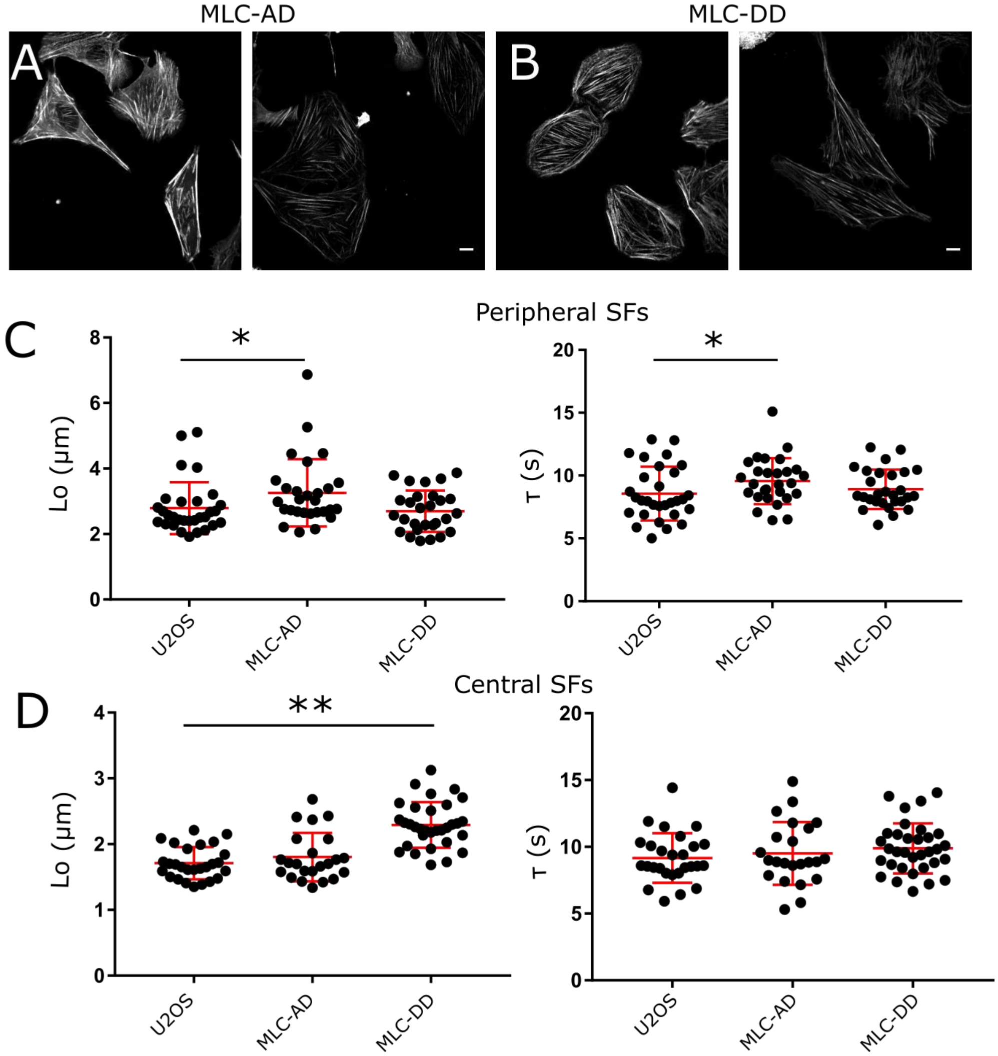

Figure 7: Expression of phosphosmimetic MLC replicates the changes in SF mechanical properties observed by expression of CA-ROCK and CA-MLCK. (A) Representative images of U2OS RFP-LifeAct GFP-MLC AD. (B) Representative images of U2OS RFP-LifeAct GFP-MLC DD. (C) L_o and τ values of peripheral SF ablation for U2OS RFP-LifeAct, U2OS RFP-LifeAct GFP MLC-AD and U2OS RFP-LifeAct GFP MLC-DD cells (n = 21, 28, 28 cells respectively). (D) L_o and τ values of central SF ablation for U2OS RFP-LifeAct, U2OS RFP-LifeAct GFP MLC-AD and U2OS RFP-LifeAct GFP MLC-DD cells (n = 22, 23, 31 cells respectively). Statistical differences calculated using Mann-Whitney test versus the corresponding U2OS RFP-LifeAct data sets (* = $p < 0.05$, ** = $p < 0.001$).

4.4 Discussion

We have presented a novel combination of SLA and genetic expression of MLC kinases under an inducible promoter to determine how ROCK and MLCK preferentially control central and peripheral SFs. This combination allows us to study the effect of these kinases while maintaining an intact SF network, both structurally and mechanically. Additionally, our system allows us to express specific isoforms of kinases such as ROCK 1 and ROCK 2 to study differential contributions of isoforms, a question that cannot be currently addressed pharmacologically and is challenging to do with shRNAs due to high homology between the kinases. Finally, our system allows us to also express kinases in a gradient manner and study for the first time to our knowledge, how different expression levels of each kinase translate to phosphorylated MLC levels and eventually translate to phenotypic changes in SF architecture and mechanics.

Based on previously published work, a hypothesized model of ROCK and MLCK contributions to SF mechanics is that ROCK regulates formation of central SFs whereas MLCK regulates formation of peripheral SFs (17, 18, 28). Inhibition of either kinase led to a decrease in SF mechanics of both populations, possibly due to the potency of the drugs used. However, it was unclear how the two kinases preferentially controlled each SF subpopulation. We show that ROCK and MLCK preferentially phosphorylate MLC in a graded manner (Fig. 2D-E) and that the induced changes in MLC phosphorylation levels localize on central or peripheral SFs respectively (Fig. 3), providing a previously unknown link between the relationship of ROCK and MLCK and cellular compartments (Fig. 8).

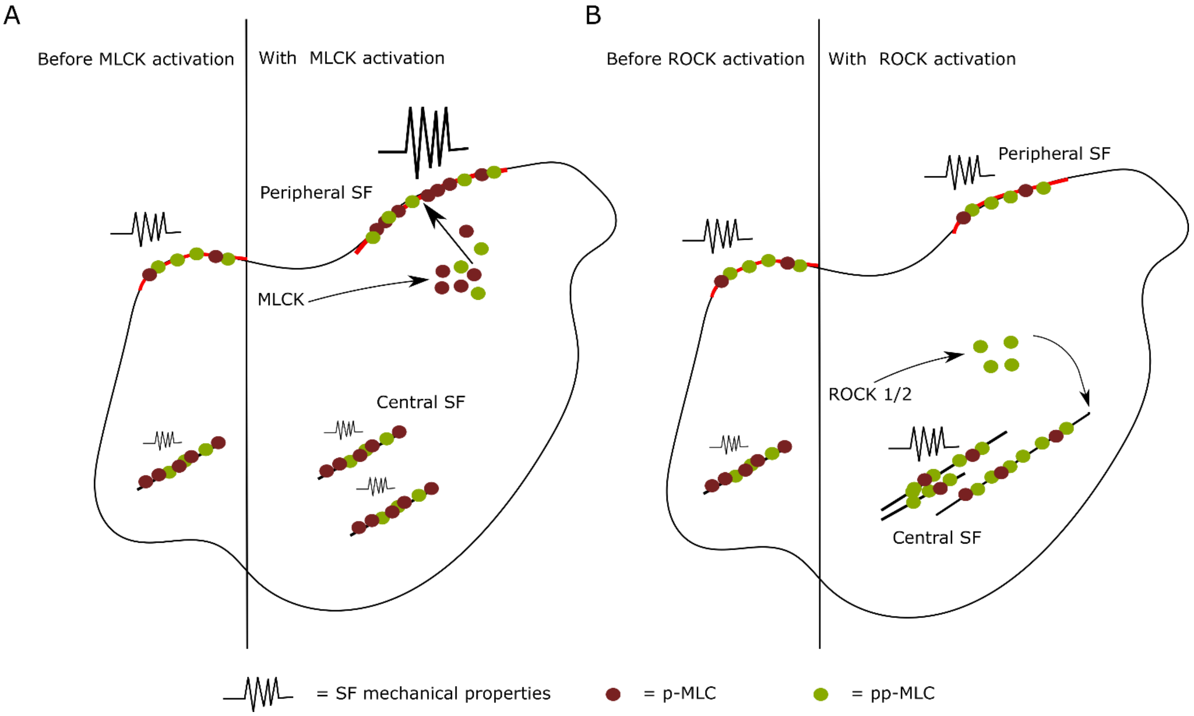

Figure 8: Schematic to summarize the proposed mechanism. (A) MLCK leads to an increase in the amount of mono-phosphorylated myosin (p-MLC) which preferentially accumulates on peripheral SFs causing them to become more viscoelastic. Central SF mechanical properties are unaffected by MLCK activation. (B) Both ROCK isoforms lead to an increase in di-phosphorylated myosin (pp-MLC) which preferentially localize on central SFs causing them to become more viscoelastic. Peripheral SF mechanical properties remain unaffected.

We also show for the first time, that indeed ROCK and MLCK regulate not only the formation but also the mechanical properties of different subpopulations of SFs – expression of either ROCK isoform altered only the retraction kinetics of central SFs and not peripheral whereas expression of MLCK altered specifically the retraction kinetics of peripheral SFs. This is the first time to our knowledge that it has been shown that ROCK and MLCK contribute to the mechanical properties of *specific* SF subpopulations. Previous attempts combining SLA and pharmacological inhibition did not show distinct regulatory control between the two kinases. This highlights the strength of our methodology over pharmacological treatments.

It is still unclear, however, how changes in phosphorylation levels change SF mechanical properties. The observed increases in L_o could be explained either by increased stiffness of the SF (increased spring constant k) or increased spacing between sarcomeric structures within the fiber (extended spring). Super-resolution imaging of phosphorylated myosin stacks within sarcomeric structures of central and peripheral SFs within CA-ROCK and CA-MLCK cells could provide further evidence to support one of these two scenarios. It is also possible that as graded phosphorylation is induced, SFs undergo both stiffness and extension at different rates leading to graded changes in SF mechanical properties.

Results shown in this study were obtained using a U2OS human osteosarcoma cell line. Previous studies that have shown a link between ROCK and central regions as well as MLCK and peripheral regions within the cell used U-373 MG, U-87 MG glioma cells, fibroblasts and MDCK epithelial cells (18, 19, 28). The similarity in results across various cell lines implies that the mechanisms of spatial regulation of SF mechanics are highly conserved among adhesive cells. Using the tools presented in this work, it may therefore be possible to map tension generation within individual SFs within a cell based on cellular location and understand how the two kinases work synergistically for cell migration and invasion.

This regulation (ROCK → pp-MLC → central, MLCK → p-MLC → peripheral) was directly proven through the use of phosphomimetic cell lines where MLC-AD phenocopied results obtained by CA-MLCK cells, whereas MLC-DD cells phenocopied results observed by CA-ROCK isoforms. Our results provide a direct link of the effect of phosphorylated MLC via ROCK or MLCK on SF mechanics. It remains unclear how MLC phosphorylation relates to NMMII isoforms. Previous work has shown that inhibition of NMMIIB phenocopied results obtained by inhibition of MLCK whereas inhibition of NMMIIA phenocopied results obtained by inhibition of ROCK (29). It will be interesting to see whether the changes in MLC phosphorylation observed in our work correspond to specific NMMII isoforms using super-resolution microscopy techniques to visualize individual myosin stacks.

Finally, we showed that graded expression of each kinase resulted to graded changes in MLC phosphorylation as well as graded changes in the mechanical properties of central or peripheral SFs. This novel result suggests that the two myosin activators control the intrinsic contractile properties of SFs in addition to changing the SF network and provides mechanistic insight into why ROCK and MLCK activation increases cellular traction forces as well as how an individual SF generates tension.

4.5 Materials and Methods

Cell lines and reagents: Viral particles of the pFUG-RFP-LifeAct vector were packaged in 293T cells and used to infect U2OS cells (ATCC HBT-96). Cells expressing the pFUG-RFP-LifeAct vector were sorted on a DAKO-Cytomation MoFlo High Speed Sorter based on RFP fluorescence (30). Myc tagged p160ROCK Δ3 (kindly provided by Shuh Narumiya, Kyoto University, Japan), Flag-tagged MLCK ED785-786KK and ROCK CAT (kindly provided by Dr. Kaibuchi, Nagoya University, Japan) were subcloned into the lentiviral vector pSLIK containing the TRE tight doxycycline-inducible promoter (22, 31). p160ROCK Δ3 is the ROCK 1isoform whereas ROCK CAT is ROCK2 and will be referred to as such in this work. Viral particles for each plasmid were packaged in 293T cells. U2OS RFP LifeAct cells were further stably transduced with the pSLIK vectors at an MOI of 0.5 IU/cell. Cells were then sorted based on RFP and Venus fluorescence. Control cell lines were created with the same method using empty vectors.

Cells were cultured in DMEM with 10% fetal bovine serum (JR scientific), 1% penicillin/strep (Thermo Fischer Scientific) and 1% Non-Essential Amino Acids (Life Technologies). Doxycycline was added at the required concentration 2 days prior to all experiments to activate the constitutively active constructs.

Cloning of phosphomimetic cell lines: Plasmids (pEGFP RLC-DD, pEGFP RLC-AD) were kindly provided by Professor Horwitz (University of Virginia, USA) (16). The RLC constructs fused to GFP were digested out of the backbone using EcoRI and XhoI and ligated into the lentiviral vector pLVX-AcGFP-N1 (Clonetech). Ligation was verified via sequencing. Viral particles for each plasmid were packaged in 293T cells. U2OS RFP-LifeAct cells were stably transduced with the pLVX vectors at an MOI of 0.5 IU/cell and 3 IU/cell. Cells were then sorted based on RFP and GFP fluorescence.

Western blots: U2OS RFP-LifeAct pSLIK CA-ROCK1, CA-ROCK2, CA-MLCK or Empty cells were cultured in the required concentration of doxycycline for 2 days prior to lysis. As described previously, cells were lysed in RIPA buffer with phosphatase and protease inhibitors (EMD Millipore, Billerica, MA) (22, 23). Protein content was measured by BCA and used to normalize samples before loading. Lysates were boiled and run on 4-12% Bis-Tris gels and transferred onto a PVDF membrane. The following primary antibodies were used: anti-phosphorylated myosin light chain 2 (Thre18/Ser19) (Cell Signaling Technology), anti-phosphorylated myosin light chain 2 (Ser19) (Cell Signaling Technology), anti-GAPDH (Sigma-Aldrich, St. Louis, MO), anti-MLCK (Sigma-Aldrich, St. Louis, MO), anti-ROCK 2 (Sigma-Aldrich, St. Louis, MO), anti-ROCK1 C8F7 (Cell Signaling Technology). The following secondaries were used: IRDye 800 Goat anti-mouse IgG and IRDye 700 Goat anti-rabbit IgG (Licor). Bands were visualized using an Odyssey system and were quantified with the built-in gel analyzer tool in ImageJ (NIH).

Deep-UV based pattern fabrication: Chrome quartz photomasks were designed using CleWin 4.0 and were printed from aBeam technologies (Hayward, CA). Patterns were made as described elsewhere (23, 32). Briefly, glass coverslips were coated with 0.01mg/ml PLL-PEG (Surface Solutions, Switzerland) in 10mM HEPES pH=7.4 for 1 hour. After drying with air, coverslips were exposed to deep UV (UVO cleaner, Jetlight, USA) through a photomask. A drop of water was used to hold the coverslips on the photomask and care was taken to remove any excess liquid and air bubbles. After Deep UV incubation, coverslips were placed in DI water and left to incubate for at least 30 minutes. Coverslips were then incubated with 34.25μg/ml of fibronectin (EMD Millipore Corporation) in 10mM HEPES pH=8.5 for 1 hour at 37°C. Patterns were washed 3 times for 5 min in phosphate-buffered saline (PBS) before cells were plated.

Cells were activated with doxycycline 2 days prior to seeding on patterns. Cells were allowed to spread on the patterns for 6 hours 30 minutes and were subsequently fixed with 4% paraformaldehyde (Alfa Aesar) for 10 minutes and washed with PBS (3 x 5 minutes).

Immunofluorescence staining: Cells (both patterned and nonpatterned) were fixed with 4% paraformaldehyde for 10 minutes, and washed using PBS. Cells were permeabilized in 0.5% Triton-X for 15 minutes, and blocked in 5% goat serum (Thermo Fisher Scientific) for 1 hour. We then incubated the cells with the primary antibody for 2 hours at room temperature in a humidity chamber, followed by washing in 1% goat serum (3 x 5 minutes) and secondary incubation for 1 hour at room temperature. We used the following antibodies: anti-phosphorylated myosin light chain 2 (Thre18/Ser19) (Cell Signaling Technology), anti-phosphorylated myosin light chain 2 (Ser19) (Cell Signaling Technology), anti-vinculin (Sigma-Aldrich), Alexa-fluor 647 anti-mouse, Alexa-fluor 488 anti-rabbit, Alexa-fluor 633 anti-rabbit and Alexa-fluor 488 anti-mouse (Thermo Fisher Scientific). F-actin was stained with 546-phalloidin. Immunofluorescence images were obtained using a swept-field upright confocal microscope equipped with a 60x water immersion lens (Prairie Technologies) or using a Nikon Eclipse Ti microscope equipped with a 20x lens. For presentation purposes, the contrast and brightness of fluorescence images were optimized using ImageJ (NIH).

Analysis of immunofluorescent images: All analyses were performed using ImageJ (NIH). For quantification of dorsal stress fiber length, images of phosphorylated myosin were overlayed with images of phalloidin to identify dorsal stress fibers and background was subtracted (Fig. 4A). Length was measured using a built-in length measurement in ImageJ. To quantify the distance of the last transverse arc, a line was manually drawn from the end of the pattern to the final transverse arc as shown in Fig. 4A.

To quantify the localization of mono-phosphorylated myosin (Ser19) and di-phosphorylated myosin (Thr18/Ser19), images were overlaid with phalloidin and background was subtracted. A line (of thickness 2 pixels) was manually drawn over stress fibers (multiple stress fibers per cell) and a measurement of raw integrated intensity of mono-phosphorylated myosin, di-phosphorylated myosin and phalloidin was recorded across the drawn line. The intensities were then normalized to the length of the drawn line and averages of raw intensities were calculated per cell. Values were normalized to the appropriate control – either CA-ROCK 2 or CA-MLCK cells cultured in 0 ng/ml doxycycline.

SF photo-disruption: SF SLA experiments were performed on a Zeis LSM 510 Meta Confocal microscope equipped with a MaiTai Ti:sapphire femtosecond laser (Spectra Physics, Newport Beach, CA) (8, 18, 29). 10,000 cells of U2OS RFP-LifeAct pSLIK CA-ROCK1, CA-ROCK2, CA-MLCK or Empty were seeded on 35 mm glass bottom dishes (MaTek Corporations) coated with 25μg/ml of fibronectin (EMD Millipore Corporation). Cells were incubated in doxycycline for 2 days. Media was changed to Live Cell Imaging Solution (Invitrogen) prior to experiment.

For SF photodisruption, the femtosecond laser was used at 770nm resulting in an energy deposition of 1-2 nJ on a single stress fiber (18, 23, 29). All images were acquired with a 40x water-dipping objective (N.A = 0.8).

Data analysis of SF retraction: SF retraction distance was recorded every 1.96 seconds for 43 seconds following SLA. Retraction dynamics were obtained through tracking of the two ends in ImageJ. Results were then fitted to a Kelvin-Voigt model

$$L = D_a + L_o\left(1 - \exp\left(-\frac{t}{\tau}\right)\right)$$

where L is defined as half the distance between the two severed ends, D_a is the length of SF destroyed by ablation, L_o is the retraction plateau distance and τ is the viscoelastic time constant determined using CurveFit, MATLAB. $L_o$is proportional to the ratio of pre-stress to elasticity of the fiber, whereas τ is the ratio of viscosity to elasticity (18, 23, 29).

Statistical analysis: All statistical analyses and graph generation were performed using GraphPad Prism. Unless otherwise noted, samples were compared using non-parametric t-tests such as Mann-Whitney.

4.6 Acknowledgements

This work was performed in part at the CRL Molecular Imaging Center supported by NIH 3R01EY015514-01S1. Confocal images were obtained at the CIRM/QB3 Stem Cell Shared Facility. EK gratefully acknowledges the support of the Howard Hughes Medical Institute International Student and Siebel Scholar fellowships. This work was supported from the National Institute of Health (1R21EB016359), the National Science Foundation (CAREER Award CMMI-1055965) and the France-Berkeley Fund. The authors would like to acknowledge Jasmine Hannah Hughes for critical discussions of analysis and results.

1. Burnette DT, et al. (2014) A contractile and counterbalancing adhesion system controls the 3D shape of crawling cells. *J Cell Biol* 205(1):83–96.
2. Kassianidou E, Kumar S (2015) A biomechanical perspective on stress fiber structure and function. *Biochim Biophys Acta - Mol Cell Res* 1853(11, Part B):3065–3074.
3. Kumar S, et al. (2006) Viscoelastic retraction of single living stress fibers and its impact on cell shape, cytoskeletal organization, and extracellular matrix mechanics. *Biophys J* 90(10):3762–73.
4. Zeng Y, et al. (2015) Formin-like2 regulates Rho/ROCK pathway to promote actin assembly and cell invasion of colorectal cancer. *Cancer Sci* 106(10):1385–1393.
5. Darby IA, Laverdet B, Bonte F, Desmouliere A (2014) Fibroblasts and myofibroblasts in wound healing. *Clin Cosmet Investig Dermatol* 7:301–311.
6. Blanchoin L, Boujemaa-Paterski R, Sykes C, Plastino J (2014) Actin dynamics, architecture, and mechanics in cell motility. *Physiol Rev* 94(1):235–63.
7. Makhija E, Jokhun DS, Shivashankar G V (2016) Nuclear deformability and telomere

dynamics are regulated by cell geometric constraints. *Proc Natl Acad Sci* 113(1):E32–E40.

8. Chang C-W, Kumar S (2013) Vinculin tension distributions of individual stress fibers within cell-matrix adhesions. *J Cell Sci* 126(Pt 14):3021–30.
9. Lee JP, Kassianidou E, MacDonald JI, Francis MB, Kumar S (2016) N-terminal Specific Conjugation of Extracellular Matrix Proteins to 2-Pyridinecarboxaldehyde Functionalized Polyacrylamide Hydrogels. *Biomaterials* 102:268–276.
10. Vicente-Manzanares M, Ma X, Adelstein RS, Horwitz AR (2009) Non-muscle myosin II takes centre stage in cell adhesion and migration. *Nat Rev Mol Cell Biol* 10(11):778–90.
11. Umemoto S, Bengur AR, Sellers JR (1989) Effect of multiple phosphorylations of smooth muscle and cytoplasmic myosins on movement in an in vitro motility assay. *J Biol Chem* 264(3):1431–6.
12. Mizutani T, Haga H, Koyama Y, Takahashi M, Kawabata K (2006) Diphosphorylation of the Myosin Regulatory Light Chain Enhances the Tension Acting on Stress Fibers in Fibroblasts. 731(December 2005):726–731.
13. Kamisoyama H, Araki Y, Ikebe M (1994) Mutagenesis of the Phosphorylation Site (Serine 19) of Smooth Muscle Myosin Regulatory Light Chain and Its Effects on the Properties of Myosin. *Biochemistry* 33(3):840–847.
14. Saitoh T, et al. (2001) Differential localization of non-muscle myosin II isoforms and phosphorylated regulatory light chains in human MRC-5 fibroblasts. *FEBS Lett* 509(3):365–9.
15. Sakurada K, Seto M, Sasaki Y (1998) Dynamics of myosin light chain phosphorylation at Ser 19 and Thr 18 / Ser 19 in smooth muscle cells in culture. *Am J Physiol Cell Physiol* 274:1563–1672.
16. Vicente-Manzanares M, Horwitz AR (2010) Myosin light chain mono- and di-phosphorylation differentially regulate adhesion and polarity in migrating cells. *Biochem Biophys Res Commun* 402(3):537–42.
17. Totsukawa G, et al. (2000) Distinct roles of ROCK (Rho-kinase) and MLCK in spatial regulation of MLC phosphorylation for assembly of stress fibers and focal adhesions in 3T3 fibroblasts. *J Cell Biol* 150(4):797–806.
18. Tanner K, Boudreau A, Bissell MJ, Kumar S (2010) Dissecting regional variations in stress fiber mechanics in living cells with laser nanosurgery. *Biophys J* 99(9):2775–83.
19. Watanabe T, Hosoya H, Yonemura S (2007) Regulation of Myosin II Dynamics by Phosphorylation and Dephosphorylation of Its Light Chain in Epithelial Cells □. 18(February):605–616.
20. Ikebe M, Hartshorne DJ (1985) Phosphorylation of smooth muscle myosin at two distinct sites by myosin light chain kinase. *J Biol Chem* 260(18):10027–10031.
21. Ikebe M, Hartshorne DJ, Elzinga M (1986) Identification, phosphorylation, and dephosphorylation of a second site for myosin light chain kinase on the 20,000-dalton

light chain of smooth muscle myosin. *J Biol Chem* 261(1):36–39.

22. Wong SY, et al. (2015) Constitutive activation of myosin-dependent contractility sensitizes glioma tumor-initiating cells to mechanical inputs and reduces tissue invasion. *Cancer Res* . doi:10.1158/0008-5472.CAN-13-3426.

23. Kassianidou E, Brand CA, Schwarz US, Kumar S (2017) Geometry and network connectivity govern the mechanics of stress fibers. *Proc Natl Acad Sci* 114(10):2622–2627.

24. Ishizaki T, et al. (1997) p160ROCK, a Rho-associated coiled-coil forming protein kinase, works downstream of Rho and induces focal adhesions. *FEBS Lett* 404(2–3):118–124.

25. Gallagher PJ, Herring BP, Trafny A, Sowadski J, Stull JT (1993) A molecular mechanism for autoinhibition of myosin light chain kinases. *J Biol Chem* 268(35):26578–26582.

26. Leung T, Manser E, Tan L, Lim L (1995) A Novel Serine/Threonine Kinase Binding the Ras-related RhoA GTPase Which Translocates the Kinase to Peripheral Membranes. *J Biol Chem* 270(49):29051–29054.

27. Tanner K, Boudreau A, Bissell MJ, Kumar S (2010) Dissecting regional variations in stress fiber mechanics in living cells with laser nanosurgery. *Biophys J* 99(9):2775–2783.

28. Katoh K, Kano Y, Amano M, Kaibuchi K, Fujiwara K (2001) Stress fiber organization regulated by MLCK and Rho-kinase in cultured human fibroblasts. *Am J Physiol Cell Physiol* 280:1669–1679.

29. Chang C-W, Kumar S (2015) Differential Contributions of Nonmuscle Myosin II Isoforms and Functional Domains to Stress Fiber Mechanics. *Sci Rep* 5:13736.

30. Lee JP, Kassianidou E, MacDonald JI, Francis MB, Kumar S (2016) N-terminal Specific Conjugation of Extracellular Matrix Proteins to 2-Pyridinecarboxaldehyde Functionalized Polyacrylamide Hydrogels. *Biomaterials* 102:268–276.

31. MacKay JL, Kumar S (2014) Simultaneous and independent tuning of RhoA and Rac1 activity with orthogonally inducible promoters. *Integr Biol* 6(9):885–894.

32. Azioune A, Carpi N, Tseng Q, Théry M, Piel M (2010) Protein micropatterns: A direct printing protocol using deep UVs. *Methods Cell Biol* 97(10):133–146.

Appendix III. Supplementary text and figures for Chapter 4

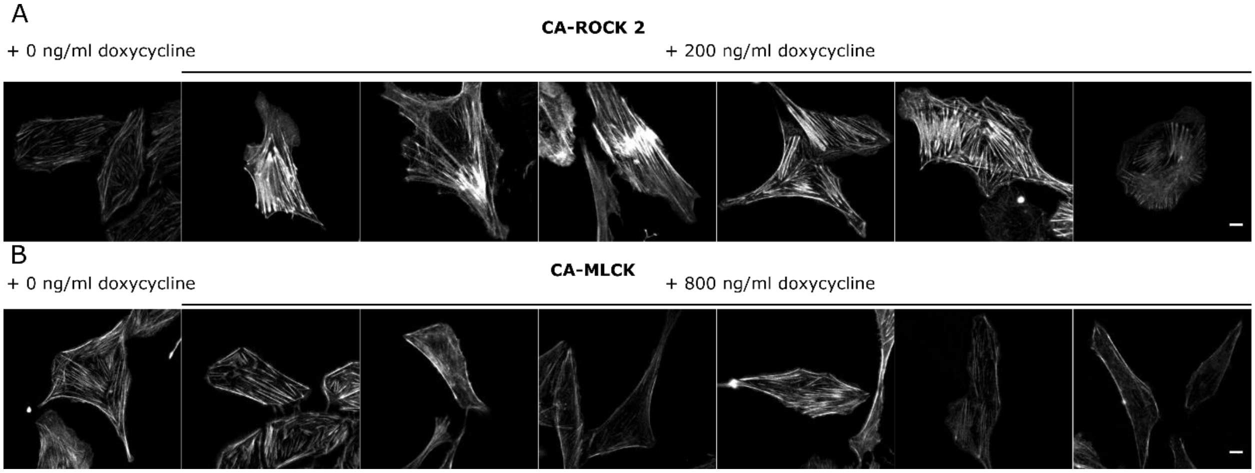

Figure S1: Representative examples of stress fiber architectures as seen by RFP-LifeAct of (A) CA-ROCK 2 and (B) CA-MLCK cells grown in the presence and absence of doxycycline. CA-ROCK 2 cells grown in doxycycline exhibit thick central SFs whereas CA-MLCK cells grown in doxycycline exhibit longer phenotypes. Scale bars = 10 µm.

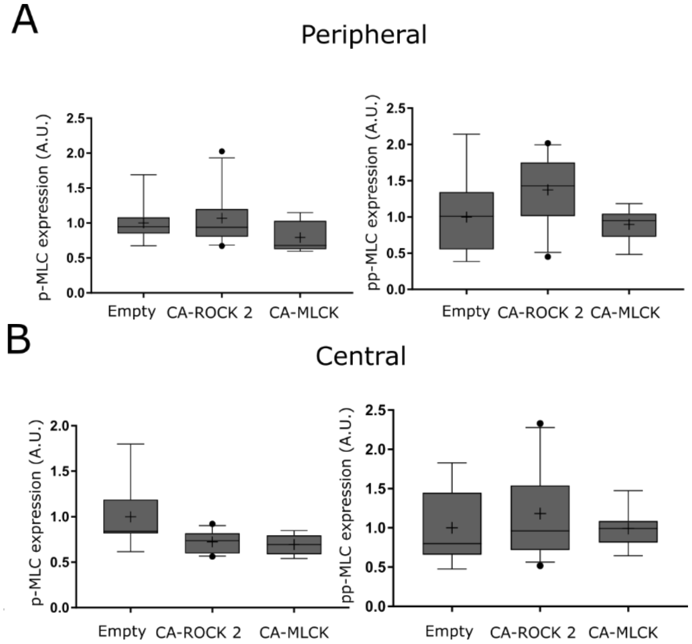

Figure S2: Intensity levels of mono-phosphorylated and di-phosphorylated levels of CA-MLCK and CA-ROCK 2 cells cultured in the absence of doxycycline match those of control cells transduced with an empty vector. (A) Quantification of immunofluorescence intensity of mono-phosphorylated and di-phosphorylated MLC within peripheral SFs (n = 9, 11 and 8 cells for each cell line for both p-MLC and pp-MLC expression). (B) Quantification of immunofluorescence intensity of mono-phosphorylated and di-phosphorylated MLC within central SFs (n = 9, 12 and 8 cells for each cell line for both p-MLC and pp-MLC expression). Intensities was normalized to that of control cells transduced with an empty vector. Boxes represent 25th and 75th percentiles; whiskers represent 10th and 90th percentiles. Cross represents the mean of the distribution. No statistical differences were observed among any of the conditions (Kruskal Wallis followed by Dunn test).

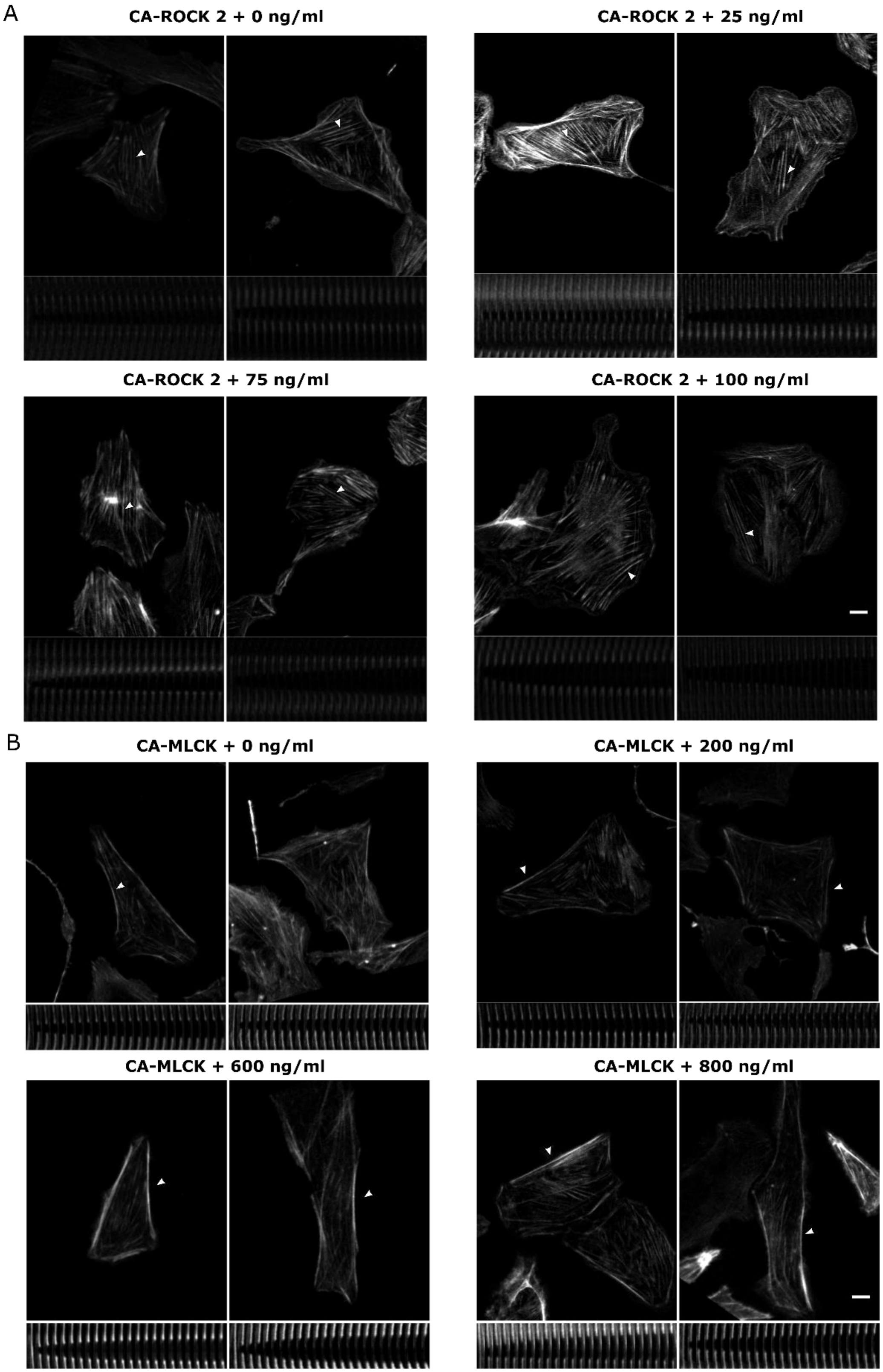

Figure S3: Examples stress fiber architectures of (A) CA-ROCK 2 and (B) CA-MLCK cells cultured in varying concentrations of doxycycline. White arrow points to ablation point. Montage of SF retraction portrayed in below each image. Scale bars = 10 µm.

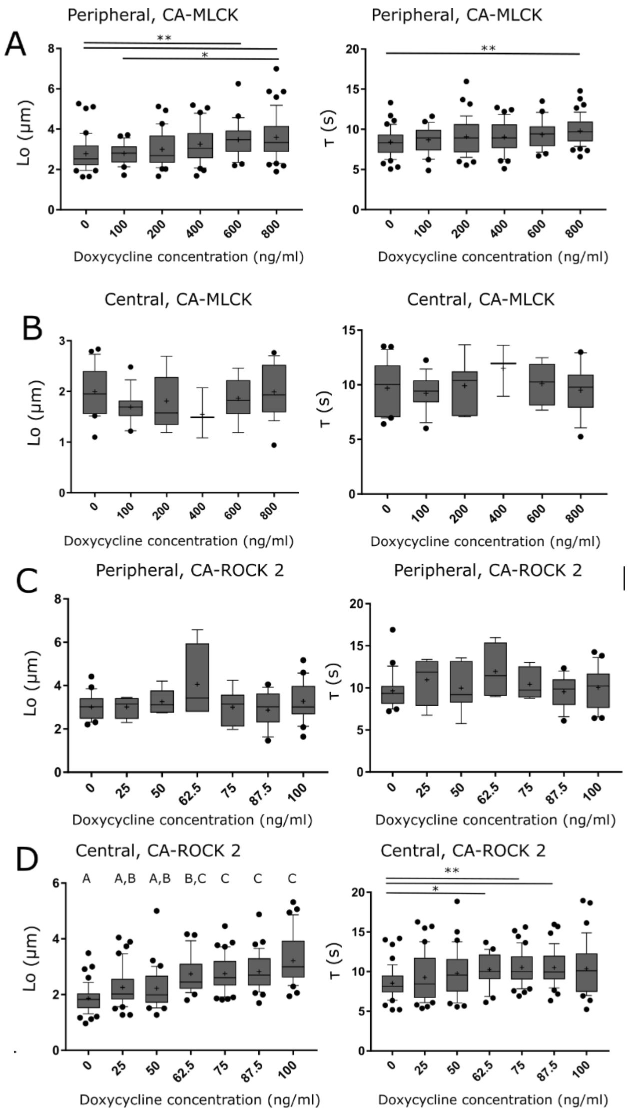

Figure S4: SF mechanical properties increase in a graded manner following graded expression of kinases and graded phosphorylation of MLC by varying doxycycline concentration in the media. (A) Lo and τ values of peripheral SF ablation for CA-MLCK cells cultured in varying amounts of doxycycline (n = 42, 24, 39, 37, 25, 47 cells per concentration plotted). (B) Lo and τ values of central SF ablation for CA-MLCK cells cultured in varying concentrations of doxycycline (n = 22, 14, 7, 3, 9, 19 cells per concentration plotted). (C) Lo and τ values of peripheral SF ablation for CA-ROCK 2 cells cultured in varying amounts of doxycycline (n = 21, 4, 6, 4, 6, 14, 21 cells per concentration plotted). (D) Lo and τ values of central SF ablation for CA-MLCK cells cultured in varying concentrations of doxycycline (n = 49, 41, 31, 25, 40 and 38 cells per concentration plotted). Statistical differences determined using Kruskal-Wallis followed by Dunn test. * denote $p < 0.01$ and ** denote $p < 0.05$. A, B and C statistical families show differences $p<0.05$ determined using Dunn test for multiple comparisons of non-normally distributed data. Boxes represent 25th and 75th percentiles; whiskers represent 10th and 90th percentiles. Cross represents the mean of the distribution.

Chapter 5. Conclusions

The work described in this dissertation explores the parameters that contribute to stress fiber (SF) viscoelasticity. In Chapter 1, we reviewed current knowledge of the biological composition of SFs as well as techniques used to study their mechanical properties. We discussed the advantages and disadvantages of each technique, with a special focus on subcellular laser ablation (SLA), a technique we use heavily in subsequent chapters. We briefly explored the mechanical models developed to explain the observed exponential retraction of SFs after SLA and discussed the limitations as well as predictions made by each model.

In Chapter 2, we combined SLA with single cell micropatterning to standardize cellular shape, area, aspect ratio and determine how the geometry of a single SF, particularly its length, contributes to its viscoelastic properties. We observed that increasing SF length does increase the elastic energy dissipated by an SF (L_o) after SLA but the relationship is more complicated than anticipated - with increasing SF length, the rate of increase in L_o decreases. Despite the use of single cell micropatterning to standardize the cellular and SF geometry, we still observed heterogeneity in the internal SF architecture. We determined experimentally that the geometry of the connecting SF network, specifically the location and angle of connecting SFs along the peripheral SF can alter the retraction kinetics. Finally, we developed a simple active-cable model that takes as an input the geometry of the connecting SF network and can predict remarkably well the retraction kinetics observed experimentally.

In Chapter 3, we wished to understand the parameters that contribute to the observed internal SF heterogeneity by combining singe cell micropatterning and time-lapse imaging of SFs evolution. We showed that the initial cellular binding position on the micropattern as well as the spreading history of the cell over the pattern can predict the final internal SF configuration. Furthermore, we show that the adhesive geometry contributes to the final SF configuration irrespective of initial binding position by altering the spreading history of the cell. Finally, we show that after SF disassembly, cells return to similar SF configurations, suggesting that cells maintain a memory of the SF network encoded or maintained by other cytoskeletal and adhesive structures.

In Chapter 4, we began to explore the molecular pathways that contribute to SF viscoelasticity, specifically Myosin Light Chain Kinase (MLCK) and Rho Associated Kinase (ROCK). We wished to understand how each kinase regulates a different subpopulation of SFs, specifically MLCK regulates formation of peripheral SFs whereas ROCK regulates formation of central SFs. Through overexpression of a constitutively active form of MLCK and ROCK, we showed that MLCK preferentially mono-phosphorylates myosin light chain (MLC) which localizes mostly on peripheral SFs altering their viscoelastic properties. MLCK overexpression does not affect central SF viscoelasticity. ROCK expression preferentially di-phosphorylates MLC which localizes on central SFs leading to increased viscoelasticity of central but not peripheral SFs. Furthermore, graded expression of each kinase results in graded changes in SF viscoelasticity, showing for the first time that SF mechanical properties can be tuned in a graded manner.

Overall, the work presented in this thesis provides a new framework to investigate mechanical properties of SFs. First, SFs have always been presented as isolated bodies that do not interact with each other or other cytoskeletal elements. Our work shows that SFs do interact with each other as well as with vimentin and these interactions contribute to the tension distribution across peripheral SFs as measured by SLA. It is important to appreciate how these interactions form molecularly, how they participate in the overall tension distribution throughout the cell as well as how they evolve over time as the cell is migrating. We can exploit the tools developed in this thesis by potentially combining them with traction force microscopy or FRET tension sensors to deepen our understanding of how SFs generate tension and contribute to motility (1–3). Additionally, this theme of connectivity can be expanded to other cytoskeletal elements. Vimentin, an intermediate filament protein, has been shown to interact directly with actin and the vimentin-actin filaments are significantly stiffer than either vimentin or actin filaments alone (4, 5). Preliminary data presented in Appendix IV shows that vimentin also contributes to the viscoelastic properties of central SFs but not peripheral.

Second, while we do show that there is a relationship between SF length and retraction kinetics, it is still unclear how this relationship translates to individual sarcomeric structures. Super-resolution imaging of sarcomeric structures of peripheral SFs on different patterns can show whether longer SFs are made up of more sarcomeric structures of fixed length or the same number of sarcomeric structures with increased length (6–8). Furthermore, it will be interesting to see whether sarcomeric structures close to connecting SFs exhibit different lengths compared to structures further away. This will provide direct evidence that connecting SFs pull on the peripheral SF and stretch the “spring”, a key concept in our active-cable model.

Finally, all the work presented in this thesis concentrates on ventral SFs, a subtype responsible for traction generation at the rear of the cell during migration. As described in Chapter 1, there are 4 subtypes of SFs – ventral, dorsal, peripheral and transverse arcs (9, 10). It will be interesting to explore how geometry contributes to the retraction kinetics of the remaining subtypes and how connections between different subtypes of SFs may alter retraction after SLA. We have shown that ROCK regulates the geometry of the connecting SF network by shifting transverse arcs further away from the lamella of the cell leading to increased dorsal SF lengths in cells cultured on crossbow patterns but leads to increased connectivity on peripheral SFs on cells cultured on rectangular patterns. This raises the question of how the SF network rearranges its connections from a static phenotype (rectangular pattern) to a migratory phenotype (cross-bow) and how this rearranges tensile forces within the cell – a question explored to some extend in Chapter 2 by EGF stimulation of cells on rectangular patterns.

1. Wang Y, Wang N (2009) FRET and mechanobiology. *Integr Biol (Camb)* 1(10):565–73.
2. Grashoff C, et al. (2010) Measuring mechanical tension across vinculin reveals regulation of focal adhesion dynamics. *Nature* 466:263–6.
3. Soiné JRD, et al. (2015) Model-based Traction Force Microscopy Reveals Differential Tension in Cellular Actin Bundles. *PLoS Comput Biol* 11(3):e1004076.
4. Esue O, Carson AA, Tseng Y, Wirtz D (2006) A direct interaction between actin and vimentin filaments mediated by the tail domain of vimentin. *J Biol Chem* 281(41):30393–30399.
5. McCormick MB, Kouklis P, Syder A, Fuchs E (1993) The roles of the rod end and the tail in vimentin IF assembly and IF network formation. *J Cell Biol* 122(2):395–407.
6. Beach JR, et al. (2014) Nonmuscle myosin II isoforms coassemble in living cells. *Curr Biol* 24(10):1160–6.
7. Hu S, et al. (2017) Long-range self-organization of cytoskeletal myosin II filament stacks. *Nat Cell Biol* 19(2):133–141.
8. Beach JR, et al. (2017) Actin dynamics and competition for myosin monomer govern the sequential amplification of myosin filaments. *Nat Cell Biol* 19(2):85–93.
9. Livne A, Geiger B (2016) The inner workings of stress fibers - from contractile machinery to focal adhesions and back. *J Cell Sci* 129(7):1293–1304.
10. Kassianidou E, Kumar S (2015) A biomechanical perspective on stress fiber structure and function. *Biochim Biophys Acta - Mol Cell Res* 1853(11, Part B):3065–3074.

Appendix IV. Interconnectivity of stress fibers and vimentin regulates retraction kinetics of central stress fibers

AIV.1 Abstract

Stress fibers (SFs) reside within a network of cytoskeletal structures including other SFs, microtubules and intermediate filaments. Based on our new understanding of how SF viscoelasticity is influenced by the geometry of the surrounding SF network (Chapter 2), we decided to explore how other cytoskeletal networks, specifically vimentin, a type III intermediate filament, interact with SFs. We show that the elastic energy dissipated by central SFs in cells lacking a vimentin network is increased compared to central SFs of control cells. Our preliminary results suggest that the vimentin network is interacting specifically with central SFs and the physical interaction is preventing the fiber ends from retracting away from each other after subcellular ablation.

AIV.2 Introduction

Stress fibers (SFs) are an important constituent of the cellular cytoskeleton that is responsible for force generation and transmission within a single cell as well as within a tissue. SF mechanical properties have been investigated experimentally via isolation of SFs followed by tensile testing (1, 2), via subcellular laser ablation that allows interrogation of SFs within a living cell (3–6) as well as computational modeling (7–9). In most of these cases, an SF is treated as an individual body isolated from the rest of the cell. As we show in Chapter 2, however, the geometry of the surrounding SF network is an important contributor to the viscoelastic properties of an individual SF (10). This finding raises the question of how possible interactions from other cytoskeletal elements such as intermediate filaments contribute to the observed SF viscoelasticity.

Vimentin is a major intermediate filament proteins in mesenchymal cells and contributes to cell migration, proliferation, contractility and morphogenesis. Biochemical assays using purified vimentin and actin filaments show that the two interact directly through the tail domain of vimentin to form structures that are stiffer than the two individual networks (11). Vimentin can associate with actin filaments through its C-terminal tail via plectin, a cytoskeletal cross linker (12). Plectin-mediated interplay between transverse arcs and vimentin has been shown to control the localization as well as the dynamics of both the vimentin and SF networks (12). Additionally, vimentin can be phosphorylated by Rho Associated Kinase (ROCK – discussed further in Chapter 4). Phosphorylation via ROCK causes the vimentin network to break down. The fact that ROCK can control both the vimentin and the central SF network suggests that there may be a functional interplay between the two cytoskeletal elements (13).

While there have been some studies to explore the direct interaction of vimentin and SFs *in vitro* and *in vivo* (12, 14), very little is known about how molecular and physical interactions between the two cytoskeletal systems contribute to the mechanical properties of an individual SF within the cell. In this appendix, we sought to determine how the physical interaction between vimentin and central or peripheral SFs alters the mechanical properties of SFs. To answer this question, we combined subcellular laser ablation (SLA) with molecular toots such as CRISPR to ablate the expression of vimentin and determine how SFs behave in the presence and absence of the vimentin network.

AIV.3 Results

First, we sought to further understand the interaction between SFs and the vimentin network by transfecting U2OS RFP-LifeAct with EGFP-Vimentin (Fig. 1). We observed that the vimentin network of U2OS cells localizes primarily around the nucleus, consistent with previous studies (12). As a result, peripheral SFs do not strongly colocalize with the vimentin network. Central SFs, however, are sometimes surrounded by the vimentin network (left inset, white arrow head). We performed SLA on such SFs and observed minimal retraction (right inset, white arrow heads point to ends of SF after SLA). We hypothesized that the presence of the intermediate filament network regulates central SF retraction kinetics –vimentin may regulate the distance the two ends can retract away from each other (L_o), slow down the retraction (τ), or influence both.

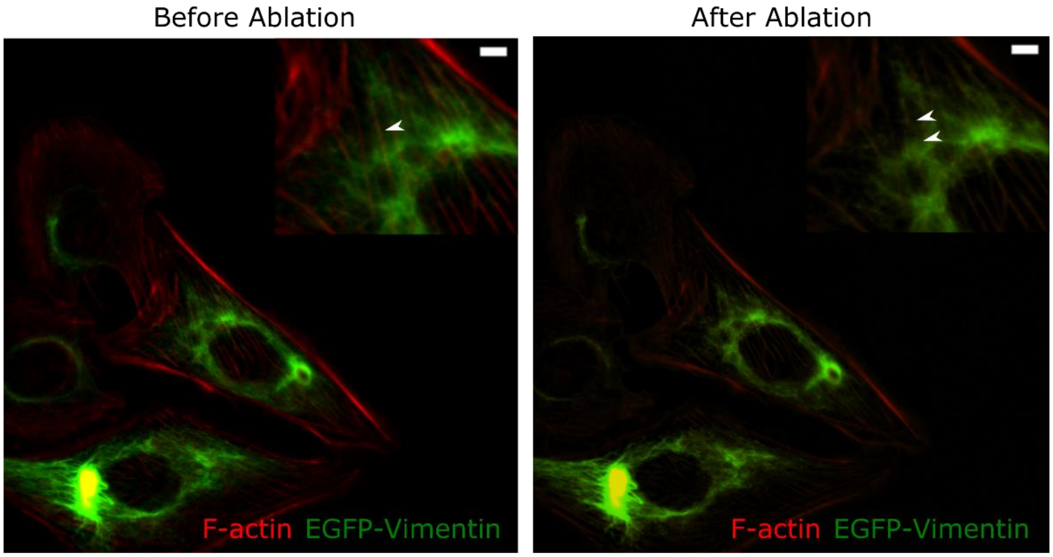

Figure 1: Appreciating the interaction between central stress fibers and the vimentin network in U2OS cells. U2OS RFP-LifeAct cells were transfected with EGFP-Vimentin to visualize the interaction of the two cytoskeletal networks. Central stress fibers are surrounded by the vimetnin network (“before ablation” inset, white arrowhead) whereas peripheral stress fibers are isolated. After subcellular ablation, central SFs retract minimally suggesting that the vimentin network may be interfering with the release of elastic energy (“after ablation” inset, white arrowheads point to ends of stress fiber) Scale bars = 10 µm for inset.

To determine if vimentin is indeed interacting with central SFs and regulating the observed retraction kinetics, we created vimentin null U2OS cell lines using CRISPR. Vimentin knock-out was verified using Western Blotting (Fig. 2A) as well as immunostaining (Fig. 2B). Based on these results, we were successful at creating two cell lines that lack the vimentin as well as a control cell line that exhibits similar expression levels of vimentin to naïve U2OS cells.

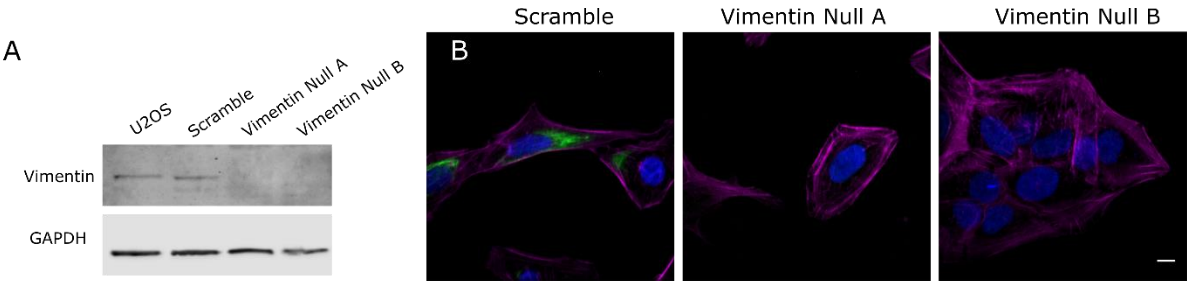

Figure 2: Characterization of U2OS vimentin null cell lines using CRISPR. (A) Western blot showing vimentin expresion of naïve U2OS, U2OS transfected with CRISPR plasmid + scramble, U2OS vimentin null A and U2OS vimentin null B cells. A full knockout of vimentin is observed in Vimentin null A and vimentin null B cell lines. (B) Immunostaining of vimentin to verify knockout in Vimentin null A and Vimentin null B cells (magenta = F-actin, green = vimentin, blue = nucleus). Scale bars = 10 µm.

We then looked at the distribution of SFs in the control and Vimentin null cell lines. In the control cell lines, U2OS exhibit thick and short central SFs that span the entire area of the cell (Fig. 3A). Ablation of these central SFs results in a small retraction as shown by the white arrowheads, similar to retractions observed in naive U2OS RFP-LifeAct cells (scramble: 1.984 µm ± 0.5215 µm, naïve: 1.71 µm ± 0.2449 µm). Vimentin null cells, however, exhibit thin and long central SFs that primarily localize closer to the cell's periphery (Fig. 3B). After ablation, the SF ends retract further away from each other and in some cases, the distance between the two ends is more than 10 µm. To quantify SLA results, we fit the retraction of a SF to the Kelvin Voigt model of viscoelasticity and obtained the retraction plateau coefficient L_o, a correlation to the elastic energy dissipated by the fiber, and the viscoelastic time constant τ, which is the ratio of viscosity over elasticity. We first analyzed the retraction kinetics of peripheral SFs and observed no statistical differences between the control and vimentin null cells for either L_o or τ (Fig. 3C). We then analyzed the retraction kinetics of central SFs and observed that in the absence of vimentin, SFs exhibited larger L_o values ($p = 0.0014$ for control versus vimentin null A and $p = 0.0074$ for control versus vimentin null B). The viscoelastic time constant τ, however, remained unaffected by the absence of the vimentin network ($p > 0.999$ for control versus vimentin null A and $p = 0.6823$ for control versus vimentin null B) (Fig. 3D). These results suggest that the vimentin network interacts specifically with central SFs and not peripheral and this interaction prevents the fiber from recoiling fully.

AIV.4 Discussion

This study takes first steps towards investigating how the interaction of the vimentin intermediate filament and SF networks contributes to the viscoelastic properties of SFs by combining SLA and molecular tools such as CRISPR. First, we show via immunostaining that vimentin directly interacts with central SFs and not peripheral. Second, central SFs of vimentin-null cells dissipate higher elastic energy after SLA compared to central SFs of control cells. Preliminary data via Western blotting (not shown) shows that vimentin-null cells express similar levels of phosphorylated myosin to control cells - the differences in retraction are, therefore, not due to differences in the amount of phosphorylated myosin found on central SFs.

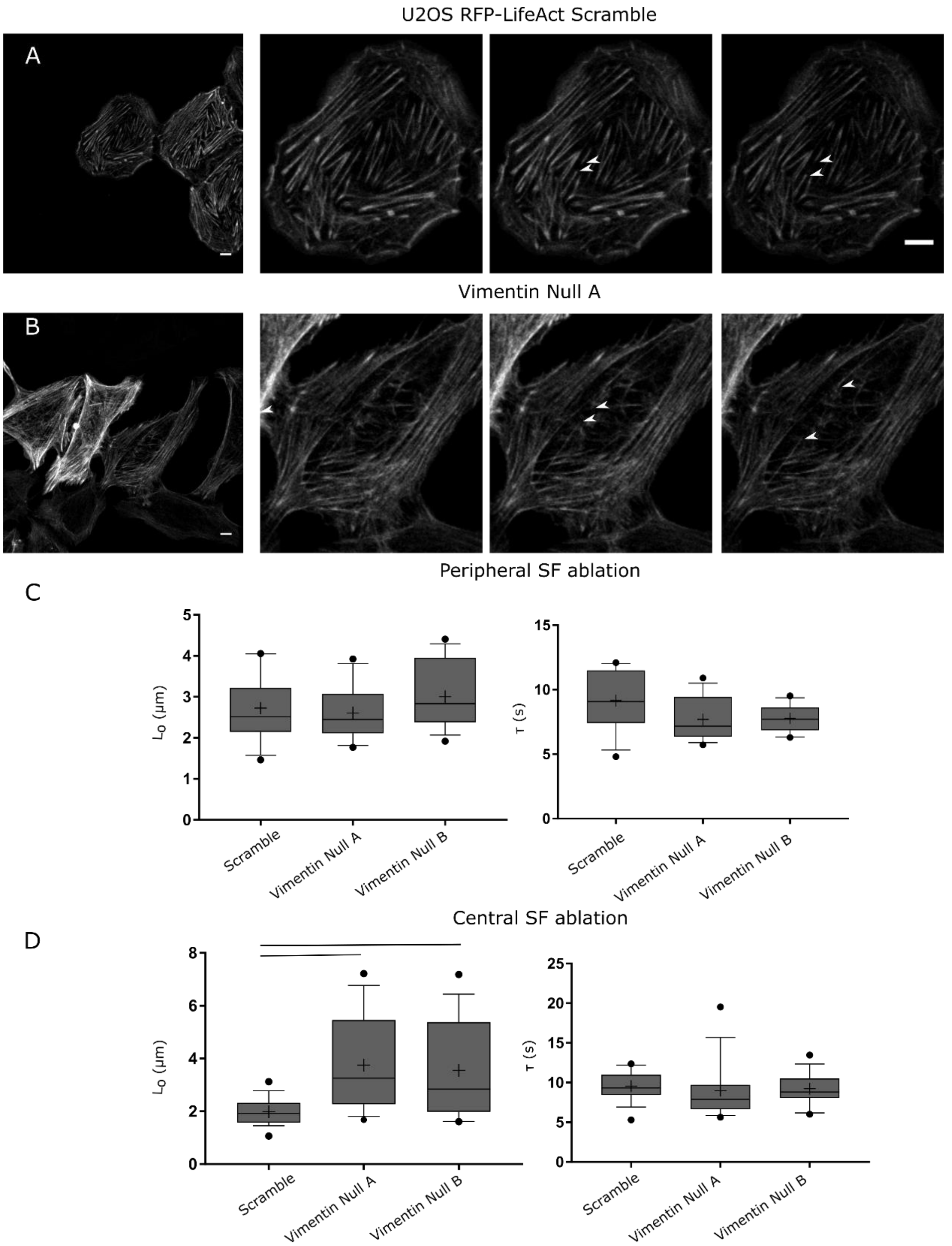

Figure 3: Central stress fibers within vimentin null cells exhibit higher elastic energy dissipation after subcellular ablation. (A) U2OS scramble cells exhibit thick central stress fibers that retract minimally after subcellular laser ablation (white arrowheads point to ends of cut stress fiber). (B) Vimentin null A cells do not have thick central stress fibers. Instead, they exhibit long and very thin stress fibers that localize close to the cell's periphery. After ablation, the two ends (white arrowheads) retract away from each other. (C) Quantification of subcellular laser ablation of peripheral stress fibers. Peripheral stress fibers retract similarly in the presence and absence of vimentin (N = 11, 12 and 14 cells respectively). (D) Quantification of subcellular laser ablation of central stress fibers. Central stress fibers in vimentin null A and vimentin null B cells exhibit a higher L_o value compared to scramble. No statistical differences are observed for the viscoealstic time constant, τ (N = 18, 17 and 16 cells respectively, Kruskal-Wallis followed by Mann-Whitney non parametric test, $p < 0.008$) Scale bars = 10 µm.

These results support a model where the physical interaction between vimentin and central SFs prevents the central SF from retracting freely – vimentin may therefore stabilize the formation and maintenance of central SFs in U2OS cells.

Further work is required to fully understand how this physical interaction is taking place. First, it is important to perform rescue studies in which we express full length-vimentin into the vimentin null cells to investigate whether we can recapture the retraction kinetics observed in the control cells. This will allow us to conclude definitively that the absence of vimentin is contributing to the changes in the retraction kinetics. Second, expression of vimentin mutants lacking head domain or tail domain (14) into the vimentin null cells will allow us to determine which domain of vimentin is functionally important for this physical interaction to occur. Additionally, super-resolution imaging of the actin and vimentin network is required to assess the level of physical interaction between the two networks.

In addition to the physical interaction, there is an important and very interesting molecular interaction between the two networks: ROCK can phosphorylate both the vimentin and the SF networks with opposing effects. Phosphorylation of SFs via ROCK enhances the formation of central SFs and increases their mechanical properties (see Chapter 4) whereas phosphorylation of vimentin via ROCK breaks down the intermediate filament network. It is important to understand how this molecular overlap contributes to the mechanical properties of SFs by expressing phosphomimetic vimentin in our vimentin null cells and seeing how SF mechanical properties are affected.

Overall, our study is the first to our knowledge to explore how the interaction of vimentin and SF networks contribute to the viscoelastic properties of SFs in living cells. While there are many remaining questions, we show that the combination of techniques discussed in this chapter can be used to probe the two networks effectively.

AIV.5 Acknowledgements

This work was performed in part at the CRL Molecular Imaging Center supported by NIH 3R01EY015514-01S1. Confocal images were obtained at the CIRM/QB3 Stem Cell Shared Facility. EK gratefully acknowledges the support of the Howard Hughes Medical Institute International Student and Siebel Scholar fellowships. This work was supported from the National Institute of Health (1R21EB016359), the National Science Foundation (CAREER Award CMMI-1055965) and the France-Berkeley Fund.

AIV.6 Materials and Methods

Creating vimentin-CRISPR cell lines: The following primers were designed using Benchling software and prepared by Elim Biopharmaceuticals:
vimentin target 1 forward: CACCGTCCTACCGCAGGATGTTCGG
vimentin target 2 forward: CACCGCTCTACGCCTCGTCCCCGGG
vimentin target 3 forward: CACCGCCCGGAGAAGAGGCGAACGA
vimentin scramble forward: CACCGCGGTCGATCCCGTTCAAGT

Primers (forward and reverse oligos) were annealed and phosphorylated (30 minutes at 37 °C, 5 minutes at 95°C, ramp down to 25 °C at 5°C per minute). Primers were then ligated into LentiCRISPR v2 (addgene plasmid #52961) for 2 hours 30 minutes at room temperature (15). Plasmids were transformed into top 10 competent bacteria (Invitrogen) and plated on LB + ampicillin plates. Bacterial cultures were selected and DNA was extracted using a mini-prep kit (Qiagen). DNA was sent for sequencing using the Human U6 forward primer: GACTATCATATGCTTACCGT.

Cell lines and reagents: U2OS cells (ATCC HBT-96) cultured in antibiotic free media were transfected with DNA (target 1, target 2, target 3 and scramble) using Viafect (Promega) at a ratio of 3:1. Transfected cells were selected using 2 µg/ml of puromycin per well for three days. At this point, knockout was assessed with Western Blotting and staining and was determined that vimentin knockout was incomplete. Target 2 however was the most efficient plasmid. To isolate cells where complete knockout was observed, a clonal expansion of U2OS Target 2 CRISPR vimentin cell lines was initiated. Cells were resuspended to 1000 cells per 200 µl and plated in 96 well plates via serial dilution across rows and columns of well plate. Single cell colonies were identified and allowed to grow. Vimentin knockout of single cell colonies were verified via Western Blotting and staining (Fig. 2).

Viral particles of the pFUG-RFP-LifeAct vector were packaged in 293T cells and used to infect U2OS vimentin null A, vimentin null B and scramble cells (ATCC HBT-96). Cells expressing the pFUG-RFP-LifeAct vector were sorted on a DAKO-Cytomation MoFlo High Speed Sorter based on RFP fluorescence (16).

Cells were cultured in DMEM with 10% fetal bovine serum (JR scientific), 1% penicillin/strep (Thermo Fischer Scientific) and 1% Non-Essential Amino Acids (Life Technologies). EGFP-Vimentin-7 was a gift from Michael Davidson (Addgene plasmid # 56439).

Western blots: Cells were lysed in RIPA buffer with phosphatase and protease inhibitors (EMD Millipore, Billerica, MA). Protein content was measured by BCA and used to normalize samples before loading. Lysates were boiled and run on 4-12% Bis-Tris gels and transferred onto a PVDF membrane. The following primary antibodies were used: anti-vimentin R28 (Cell Signaling Technology) and anti-GAPDH (Sigma-Aldrich, St. Louis, MO). The following secondary antibodies were used: IRDye 800 Goat anti-mouse IgG and IRDye 700 Goat anti-rabbit IgG (Licor). Bands were visualized using an Odyssey system and were quantified with the built-in gel analyzer tool in ImageJ (NIH).

Immunofluorescence staining: Cells were fixed with 4% paraformaldehyde for 10 minutes, and washed using PBS. Cells were permeabilized in 0.5% Triton-X for 15 minutes, and blocked in 5% goat serum (Thermo Fisher Scientific) for 1 hour. We then incubated the cells with the primary antibody for 2 hours at room temperature in a humidity chamber, followed by washing in 1% goat serum (3 x 5 minutes) and secondary incubation for 1 hour at room temperature. We used the following antibodies: vimentin R28 (Cell Signaling Technology), Alexa-fluor 488 anti-rabbit (Thermo Fisher Scientific). F-actin was stained with 546-phalloidin. Nuclear DNA was visualized using Hoechst, added 15 minutes prior to imaging (1:250 in PBS) and washed off (3 x

5 minutes with PBS). Immunofluorescence images were obtained using a swept-field upright confocal microscope equipped with a 60x water immersion lens (Prairie Technologies) or using a Nikon Eclipse Ti microscope equipped with a 20x lens. For presentation purposes, the contrast and brightness of fluorescence images were optimized using ImageJ (NIH).

SF photo-disruption: SF SLA experiments were performed on a Zeis LSM 510 Meta Confocal microscope equipped with a MaiTai Ti:sapphire femtosecond laser (Spectra Physics, Newport Beach, CA) (17–19). 10,000 cells of U2OS RFP-LifeAct Vimentin null A, Vimentin null B or scramble cells were seeded on 35 mm glass bottom dishes (MaTek Corporation) coated with 25µg/ml of fibronectin (EMD Millipore Corporation). Media was changed to Live Cell Imaging Solution (Invitrogen) prior to experiment. For SF photodisruption, the femtosecond laser was used at 770nm resulting in an energy deposition of 1-2 nJ on a single stress fiber (10, 17, 19). All images were acquired with a 40x water-dipping objective (N.A = 0.8).

Data analysis of SF retraction: SF retraction distance was recorded every 1.96 seconds for 43 seconds following SLA. Retraction dynamics were obtained through tracking of the two ends in ImageJ. Results were then fitted to a Kelvin-Voigt model

$$L = D_a + L_o\left(1 - \exp\left(-\frac{t}{\tau}\right)\right)$$

where L is defined as half the distance between the two severed ends, D_a is the length of SF destroyed by ablation, L_o is the retraction plateau distance and τ is the viscoelastic time constant determined using CurveFit, MATLAB. $L_o$is proportional to the ratio of pre-stress to elasticity of the fiber, whereas τ is the ratio of viscosity to elasticity (10, 17, 19).

Statistical analysis: All statistical analyses and graph generation were performed using GraphPad Prism. Unless otherwise noted, samples were compared using non-parametric t-tests such as Kruskal-Wallis followed by Mann-Whitney.

1. Deguchi S, Ohashi T, Sato M (2006) Tensile properties of single stress fibers isolated from cultured vascular smooth muscle cells. *J Biomech* 39(14):2603–10.
2. Deguchi S, Sato M (2009) Biomechanical properties of actin stress fibers of non-motile cells. *Biorheology* 46(2):93–105.
3. Kumar S, et al. (2006) Viscoelastic retraction of single living stress fibers and its impact on cell shape, cytoskeletal organization, and extracellular matrix mechanics. *Biophys J* 90(10):3762–3773.
4. Colombelli J, et al. (2009) Mechanosensing in actin stress fibers revealed by a close correlation between force and protein localization. *J Cell Sci* 122(11):1928.
5. Russell RJ, Xia S-L, Dickinson RB, Lele TP (2009) Sarcomere mechanics in capillary endothelial cells. *Biophys J* 97(6):1578–1585.
6. Chang C-W, Kumar S (2013) Vinculin tension distributions of individual stress fibers within cell-matrix adhesions. *J Cell Sci* 126(Pt 14):3021–3030.

7. Besser A, Colombelli J, Stelzer EHK, Schwarz US (2011) Viscoelastic response of contractile filament bundles. *Phys Rev E* 83(5):51902.

8. Stachowiak MR, O'Shaughnessy B (2008) Kinetics of stress fibers. *New J Phys* 10(2):25002.

9. Stachowiak MR, O'Shaughnessy B (2009) Recoil after severing reveals stress fiber contraction mechanisms. *Biophys J* 97(2):462–71.

10. Kassianidou E, Brand CA, Schwarz US, Kumar S (2017) Geometry and network connectivity govern the mechanics of stress fibers. *Proc Natl Acad Sci* 114(10):2622–2627.

11. Esue O, Carson AA, Tseng Y, Wirtz D (2006) A direct interaction between actin and vimentin filaments mediated by the tail domain of vimentin. *J Biol Chem* 281(41):30393–30399.

12. Jiu Y, et al. (2015) Bidirectional Interplay between Vimentin Intermediate Filaments and Contractile Actin Stress Fibers. *Cell Rep* 11(10):1511–1518.

13. Bauer PO, et al. (2012) ROCK-phosphorylated vimentin modifies mutant huntingtin aggregation via sequestration of IRBIT. *Mol Neurodegener* 7:43.

14. McCormick MB, Kouklis P, Syder A, Fuchs E (1993) The roles of the rod end and the tail in vimentin IF assembly and IF network formation. *J Cell Biol* 122(2):395–407.

15. Sanjana NE, Shalem O, Zhang F (2014) Improved vectors and genome-wide libraries for CRISPR screening. *Nat Methods* 11(8):783–784.

16. Lee JP, Kassianidou E, MacDonald JI, Francis MB, Kumar S (2016) N-terminal Specific Conjugation of Extracellular Matrix Proteins to 2-Pyridinecarboxaldehyde Functionalized Polyacrylamide Hydrogels. *Biomaterials* 102:268–276.

17. Tanner K, Boudreau A, Bissell MJ, Kumar S (2010) Dissecting regional variations in stress fiber mechanics in living cells with laser nanosurgery. *Biophys J* 99(9):2775–83.

18. Chang C-W, Kumar S (2013) Vinculin tension distributions of individual stress fibers within cell-matrix adhesions. *J Cell Sci* 126(Pt 14):3021–30.

19. Chang C-W, Kumar S (2015) Differential Contributions of Nonmuscle Myosin II Isoforms and Functional Domains to Stress Fiber Mechanics. *Sci Rep* 5:13736.